



Fermi National Accelerator Laboratory

FERMILAB-Pub-87/229

[SACLAY DPhPE 87-11]

**Can Gluinos and Squarks be Discovered at
Hadron-Hadron Colliders?
How?***

J. Freeman

Fermi National Accelerator Laboratory
P.O. Box 500, Batavia, Illinois 60510

A. Savoy-Navarro* and N. Zaganidis**
CEA-Saclay

December 1987

*Submitted to Nucl. Phys.

*Presently at Fermi National Accelerator Laboratory, Batavia, Illinois 60510

**Now at EP Division at CERN, Geneva, Switzerland



**CAN GLUINOS AND SQUARKS BE DISCOVERED AT
HADRON-HADRON COLLIDERS?
HOW?**

J. Freeman (FNAL), A. Savoy-Navarro* and N.Zaganidis** (CEA-Saclay)

Abstract

Using a uniform theoretical approach of softly broken supergravity, and realistic detector simulations, we have investigated the possible ways for: UA1 at the CERN $p\bar{p}$ collider; upgraded UA's at ACOL; CDF at the Tevatron; and superdetectors at supercolliders (LHC or SSC) to search for gluinos and squarks. For each experiment, detection and filtering techniques are discussed, and achievable detection limits on supersymmetric particle masses are presented

* Presently at Fermi National Laboratory- Batavia 60510 (Illinois) USA

** Now at EP Division at CERN ,Geneva (Switzerland)

1. Introduction

If superstring theories are the key to a unique solution of the puzzle of high energy physics, a way to search for experimental evidence of these theories is to discover supersymmetric (SUSY) particles such as gluinos and squarks. This is due to the fact that, at least at the present stage of understanding of superstrings, most of the phenomenological discussions assume supergravity at low mass scale (i.e. the scale provided by present and foreseen accelerators), in particular, to help solving the hierarchy problems such as the scales of the Fermi constant and the cosmological constant. Because of the importance of this issue, we have made a detailed study of how pp or $p\bar{p}$ colliders will be able to search for gluinos and squarks, in a mass range from a few tens of GeV up to the TeV region.

The main features of the uniform approach used to do this study are discussed in detail in Section 2. It first concerns the main hypotheses of the softly broken $N = 1$ supergravity^[1] used here as theoretical framework; secondly, it describes how the Monte Carlo Isajet^[2] generate the SUSY signals and their corresponding main backgrounds. An evaluation of the cross sections and rates which may be expected both for the signals and the backgrounds, in each case, is given at the end of this section.

The ways to search for \tilde{g} and \tilde{q} within this framework with the UA1 detector at the CERN $p\bar{p}$ collider are presented in Section 3. It is the only case up to now to provide real data to be compared with theoretical expectations. At the end of this section are presented the improvements which can be expected with an upgraded version of the $p\bar{p}$ collider at CERN (with the Antiproton Collector: ACOL) and of

the UA's detectors.

In Section 4, we present the case of the CDF detector at the FNAL Tevatron. This experiment has just started to run in 1987, and a first estimate of its possible performances with an integrated luminosity per year of 10^{36} cm^{-2} (low luminosity case) and 10^{39} cm^{-2} (upgraded case) is presented. Finally in Section 5, we briefly review the main possibilities and limitations offered by super pp colliders such as the LHC and SSC options⁽³⁾ and see how they overlap with the expected results of the Tevatron. A complete and detailed summary of the discovery limits on $m_{\tilde{g}}$ and $m_{\tilde{q}}$ that each detector and each machine could provide are given as conclusion.

2. Supersymmetric Scenarios and Generation Mechanisms

The main features of the “uniform approach” used for this study are described in details in this section. It includes first the various scenarios that may be derived from the theoretical framework considered here and secondly the mechanisms to generate them.

2.1 Theoretical Framework

The main way to produce supersymmetric particles at hadron-hadron colliders is through the following reactions:

$$pp \rightarrow \tilde{g}\tilde{g} \quad (1)$$

$$pp \rightarrow \tilde{g}\tilde{q} \quad (2)$$

$$pp \rightarrow \tilde{q}\tilde{q} \quad (3)$$

Three new types of particles are therefore expected: the gluino, squarks, and photino.

In the supergravity models^[1], the masses of the gluino (\tilde{g}) and squarks (\tilde{q}) are constrained by the relations^[1,4],

$$m_{\tilde{q}} = \sqrt{m^2 + 6.7 \mu^2}$$

and

$$m_{\tilde{g}} = (1 + 1.9) \mu$$

which take into account renormalization effects represented by the factors $6.7 \mu^2$ and 1.9μ (the precise value of these coefficients is slightly model-dependent). The parameters m and μ are the \tilde{q} and \tilde{g} masses at the Planck scale, respectively. Therefore, in supergravity, $m_{\tilde{q}}$ is smaller than $m_{\tilde{g}}$ for $m/\mu \leq 0.8$, implying $m_{\tilde{q}}/m_{\tilde{g}} \geq 0.9$. In other words, if the gluino is heavier than the squark, it may be just a little bit heavier, and so gluino and squarks will in this case be degenerate in mass.

The photino is assumed to be the lightest sparticle (LSP), to have $m_{\tilde{\gamma}} = 0$ GeV, and to be stable. Therefore, it will act as a ν -like particle and be responsible for producing, most of the time, a fair amount of missing energy in the detector. These properties of the photino are among the important assumptions of our study. However, we are well aware that one may take a more general point of view and consider the neutralino as the LSP.^[5] By neutralino $\tilde{\chi}^0$ we mean a linear combination of gauginos and higgsinos:

$$\tilde{\chi}^0 = \alpha \tilde{\gamma} - \beta \tilde{h} + \gamma \tilde{z}$$

and depending on its mass and on the various gauginos and higgsinos it is composed of, it may well be mainly $\tilde{\gamma}$ -like, \tilde{h} -like, \tilde{z} -like, or a more general mixture of all three.

It may subsequently decay into:

$$\begin{aligned} \tilde{\chi}_k^0 &\rightarrow \ell^+ \ell^- \tilde{\chi}_\ell^0, \tilde{\chi}_k^0 \rightarrow q \bar{q} \tilde{\chi}_\ell^0 \\ \text{or } \tilde{\chi}_k^0 &\rightarrow \ell^\pm \tilde{\nu}^{(-)} \tilde{\chi}_\ell^\mp, \tilde{\chi}_k^0 \rightarrow q \bar{q} \tilde{\chi}_\ell^\mp \end{aligned}$$

where $\tilde{\chi}_\ell^0$ is the lighter neutralino; likewise, $\tilde{\chi}_\ell^\mp$ is the lighter chargino. The charginos are linear combination of winos, charged higgsinos, and wiggisinos; they may also decay leptonically or hadronically according to:

$$\tilde{\chi}_\ell^\mp \rightarrow \ell^\pm \tilde{\nu}^{(-)} \tilde{\chi}_k^0 \text{ or } \tilde{\chi}_\ell^\mp \rightarrow q \bar{q} \tilde{\chi}_k^0$$

Obviously the case of a neutralino being the LSP creates a much more complicated scenario than that of the $\tilde{\gamma}$ as the LSP. For instance, if the gluino is heavier than the \tilde{q} , \tilde{q} will decay according $\tilde{q}_j \rightarrow q' + \tilde{\chi}_k^0$ or $\tilde{q}_j \rightarrow q' - \tilde{\chi}_\ell^\mp$, where $\tilde{\chi}_k^0$ and $\tilde{\chi}_\ell^\mp$ will then decay according to the decay modes described above until the lightest neutralino is reached. If, on the contrary, $m_{\tilde{g}} < m_{\tilde{q}}$, the decay $\tilde{q}_j \rightarrow q \tilde{g}$ with $\tilde{g} \rightarrow q \bar{q} \tilde{\chi}_k^0$ will be the dominant one.

As a consequence, the reactions (1), (2), and (3) will provide more complicated additional signatures, involving purely hadronic products and/or lepton(s) and/or γ 's. Moreover, the total missing energy produced in such events, will be in general “diluted” compared to the case where the $\tilde{\gamma}$ is the LSP. Studies implying such neutralinos have been done in the case of e^+e^- ^[6] and ep ^[7] colliders, at least at the phenomenological level. Up to now, this is not the case for pp collisions, which is slightly more difficult since one has to deal with \tilde{q} and \tilde{g} instead of sleptons. Considering all the various possibilities for sparticles to decay into $\tilde{\chi}^0$'s would, in the case of pp collisions, imply not only a large effort on the phenomenological side, but also a very detailed

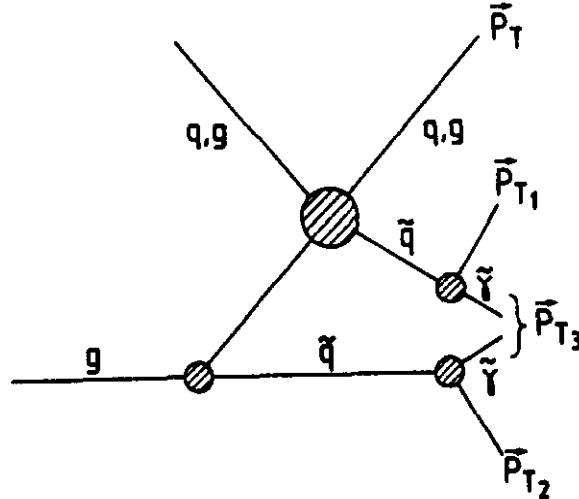
study of the ways to detect the corresponding signals. This is not done here: however, we mention later on what happens if the $\tilde{\gamma}$ as LSP only represents some percent of the total branching ratio of the sparticles decay (say 11% in BR, i.e. a factor 2% only of the corresponding cross sections for the processes (1), (2), and (3) instead of 100%).

Three kinds of situations are considered here. The first one correspond to the hypothesis $m_{\tilde{g}} \geq m_{\tilde{q}}$. As a consequence, the gluino decays into an antiquark plus a scalar quark, and the scalar quark decays into a quark and a photino: thus the processes $p\bar{p}$ or pp going to $\tilde{g}\tilde{g}$, $\tilde{q}\tilde{q}$, or $\tilde{g}\tilde{q}$ have almost the same signatures. This first alternative is particularly favorable for the low-energy case (i.e. for masses less than or equal to 100 GeV), as we will see later.

The second set of situations is provided by the cases where $m_{\tilde{g}} < m_{\tilde{q}}$; the discrepancy between the two masses can be quite large. The most probable decay mode for the squark is then that the scalar quark decays into the corresponding quark and gluino. The gluino decays into a quark plus an antiquark and a photino. The main consequence of this second picture is that the signatures of the processes (1), (2), and (3) are rather different and that the rates are different, too.

This second scenario may be pushed a little bit more, and one may consider the case of a very light gluino and a much heavier squark ($m_{\tilde{g}} \ll m_{\tilde{q}}$). We have found it interesting to distinguish two sets of conditions imposed on the decay products. The first set corresponds to the dominant decay mode, namely: $\tilde{g} \rightarrow q\bar{q}\tilde{\gamma}$ and $\tilde{q} \rightarrow q\tilde{g}$ (with $BR \simeq 93\%$). But much more striking signatures are obtained with events with $m_{\tilde{g}} \ll m_{\tilde{q}}$, produced at relatively very low p_T and with \tilde{q} decaying into $q\tilde{\gamma}$. This

decay mode is not the dominant one as $m_{\tilde{q}} > m_{\tilde{g}}$, and it represents only about 7% of the total branching ratio. As the gluino is very light compared to the squark and as both are produced at very low p_T , the signature of the process $pp \rightarrow \tilde{g}\tilde{q}$ is dominated by the squark. This process will appear, under such conditions, as $qg \rightarrow \tilde{q} \rightarrow q\tilde{\gamma}$ (i.e. a “Madrid – like”^[8] reaction). For the low c.m. energy machines, it will result in an “anomalous” rate of high E_t monojets and large missing energies. Going higher in c.m. energy, it will produce relatively low jet multiplicity events (i.e. ≤ 3 jets at LHC or SSC energies^[3]). Whereas, if the $\tilde{q} \rightarrow q\tilde{g}$, even at low p_T , the striking low jet multiplicity plus large amount of missing energy signature will be diluted by the subsequential decay of the \tilde{g} into $q\tilde{q}\tilde{\gamma}$. Moreover, it has been demonstrated^[9] that this process at relatively low p_T not only goes through a fusion mechanism, but also gets a contribution of the excitation mechanism which may even be substantial (especially when going to higher energies).



To reproduce this situation at the CERN $p\bar{p}$ collider, we have chosen as low p_T range, $2 \leq p_T \text{ (GeV/c)} \leq 20$ (the usual p_T range for this c.m. energy being:

$10 \leq p_T \leq 110$ in GeV/c. The usual ranges are chosen for computational simplicity, and correspond to almost all of the production cross-section) and $(m_{\tilde{g}}; m_{\tilde{q}}) = (10; 100)$ in GeV/c².

The value $m_{\tilde{g}} = 10$ GeV/c² corresponds to a mass just above the limit given by beam dump experiments. Note that the process $qg \rightarrow \tilde{q}\tilde{g}$ is dominant as the pair production of gluinos provides of course a tremendous number of events, but these events will not pass the first level trigger (both on E_T^{jet} and/or E_T^{miss}); on the other hand, the pair production of \tilde{q} will give very striking events but too low rate for this c.m. energy and relatively very low luminosity.

At the Tevatron, we consider $5 \leq p_T \text{ (GeV/c)} \leq 30$ (the usual range being from 20 to 200 GeV/c) and $(m_{\tilde{g}}; m_{\tilde{q}}) = (50; 250)$ in GeV/c². This value for $m_{\tilde{g}}$ is chosen assuming that a gluino with a mass in the range of a few GeV up to 50 GeV would be or is already ruled out by the CERN $p\bar{p}$ collider. (see Section 3). For this set of smasses, $\tilde{g}\tilde{q}$ and $\tilde{g}\tilde{g}$ reactions will be considered.

At very high c.m. energies (i.e. LHC or SSC) two analogous cases have been considered in great detail^[3]. They are defined by a p_T^{\min} of 20 GeV/c (the usual p_T range for these c.m. energies is from 100 to 1000 GeV/c) for $(m_{\tilde{g}}; m_{\tilde{q}}) = (100; 500)$ in GeV/c² and a p_T^{\min} of 30 GeV/c for $(m_{\tilde{g}}; m_{\tilde{q}}) = (200; 1000)$ in GeV/c².

For the two other scenarios, $m_{\tilde{g}} < m_{\tilde{q}}$ and $m_{\tilde{g}} \geq m_{\tilde{q}}$, different set of $(m_{\tilde{g}}; m_{\tilde{q}})$ have been chosen to cover the region in smass going from a few GeV to the 0(1 TeV). The p_T range considered for generating the initial partons (\tilde{g}, \tilde{q}) are respectively 10 to 110 GeV for the CERN $p\bar{p}$ collider, 20 to 200 GeV at the Tevatron, and 100 to 1000 GeV at the supercolliders. All the various set of $(m_{\tilde{g}}; m_{\tilde{q}})$ considered in this

work are indicated in Fig. 1a for the CERN $p\bar{p}$ collider and the Tevatron, and Fig. 1b for the supercolliders.

Within our theoretical framework, we have defined the reactions, the corresponding masses, decay modes, and branching ratios; now we need a program to “realistically” generate these various processes.

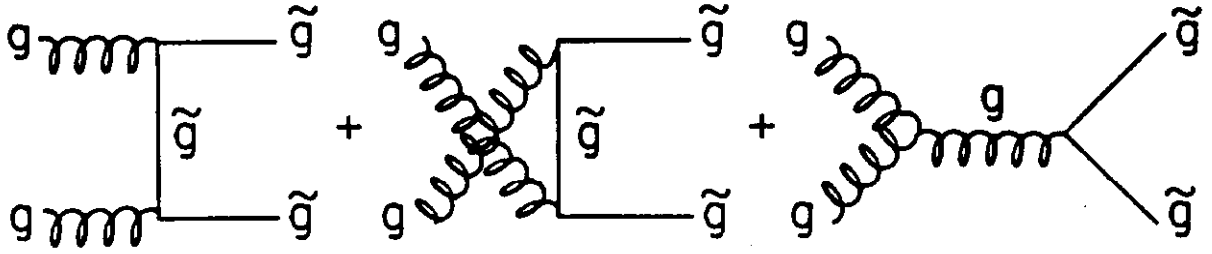
2.2 The Generator Program and Its Main Expectations

To do so, a Monte Carlo program, ISAJET^[10], able to generate the elementary processes implied by reactions (1), (2), and (3), as well as the main corresponding backgrounds is used. ISAJET includes the generation of a hard interaction by the convolution of (i) hard scattering matrix elements and (ii) structure functions; the addition of (iii) initial and (iv) final state radiation (which has been turned to fit the underlying part of UA1 events at 630 GeV c.m.); the inclusion of (v) beam jets; and finally (vi) the fragmentation of partons into hadrons and subsequent decays. Isajet has adapted the independent fragmentation. The hard matrix elements of $2 \rightarrow 1$ and $2 \rightarrow 2$ subprocesses are exactly calculated, whereas the case of $2 \rightarrow 3$ reactions are computed in an approximate way by the inclusion of initial and final state radiation. The main aspects of the section of this program devoted to the generation of SUSY processes have been implemented by F. Paige^[10] for Snowmass 1984 and includes the EHLQ calculations^[11] for the matrix elements

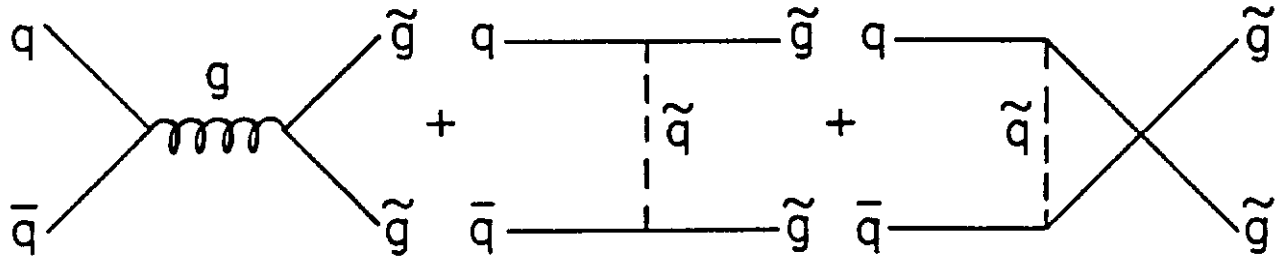
In this program, sparticles are produced with an extension of the $SU(2)_R \times SU(2)_L \times U(1)_Y$ model of weak and electromagnetic interactions. The left and right scalars partners are assumed to be degenerate, the same mixing is used for photino-zino as for photon- Z^0 , and mixings of gauginos with higgsinos are ignored. The

couplings are completely determined by the standard model and the cross-sections by the masses assumed in it. New vertices are therefore generated where the standard particles are replaced by their superpartners with the same coupling constants. For instance, the standard $q\bar{q}g$ vertex with coupling constant g_s (where: $\alpha_s = g_s^2/4\pi$) is replaced by the vertex $\tilde{q}\tilde{q}g$, or $\bar{q}\bar{q}\tilde{g}$ or $q\tilde{q}\tilde{g}$, with the same coupling constant g_s . Thanks to these Feynman rules, the various contributions to the diagrams for the production of superpartners can be calculated. $O(\alpha_s^2)$ processes are included.

To generate gluino pairs, ISAJET considers the two elementary processes: $gg \rightarrow \tilde{g}\tilde{g}$ according to the following diagrams (4):

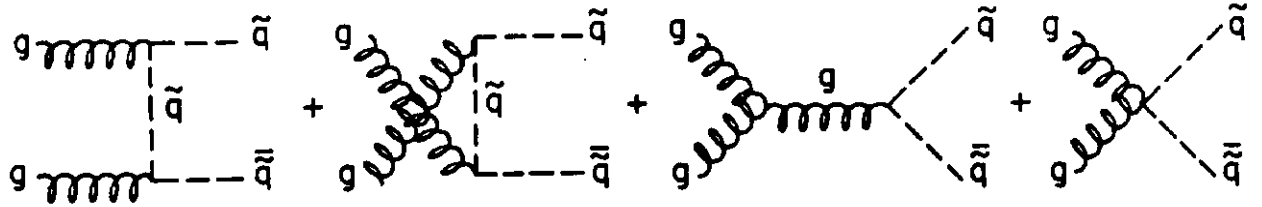


and the process $q\bar{q} \rightarrow \tilde{g}\tilde{g}$ with the following diagrams (5):

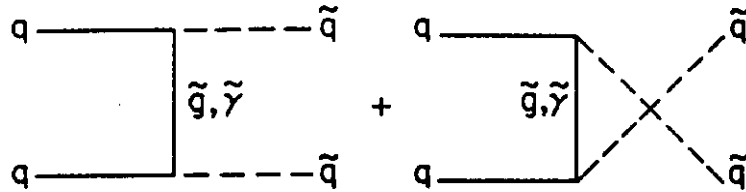


Note that the elementary cross-sections for processes (4) only depend on the mass of the gluino, whereas for processes (5) they also depend on the squark mass. As usual in ISAJET, the masses of sparticles as well as the decay modes are introduced by the users by means of data cards.

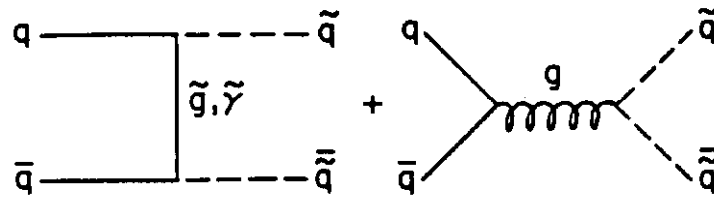
To generate squark pairs, three types of elementary reactions are used in ISAJET; the first one is $gg \rightarrow \tilde{q}\bar{\tilde{q}}$, with the following diagrams (6):



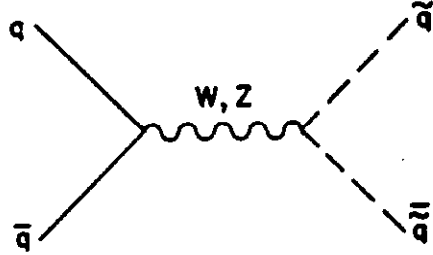
The second contribution is given by $q\bar{q} \rightarrow \tilde{q}\bar{\tilde{q}}$ for which the considered diagrams are (7):



The third contribution $qq \rightarrow \tilde{q}\bar{\tilde{q}}$ follows the diagrams (8):

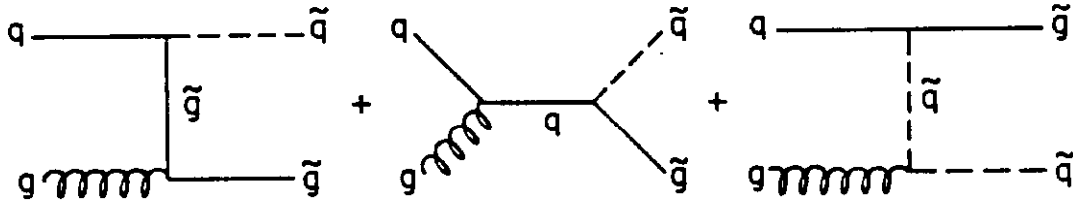


Squarks produced by W or Z^0 decays according to:



are ignored here, since they give a much smaller contribution than (6), (7), or (8).

To produce $\tilde{g}\tilde{q}$, only one elementary process contributes to the cross section: $gq \rightarrow \tilde{g}\tilde{q}$; it is provided through the following diagrams (9):



The matrix elements corresponding to each of these diagrams are computed according to EHLQ.

This is the general framework within which we have generated our theoretical hypothesis. ISAJET offers the user the freedom to introduce, “by hand”, the mass of sparticles as well as their decay modes. To be sure that Isajet correctly reproduces

EHLQ's calculations, we have performed the following check reported in Fig. 2. The cross-sections calculated by Isajet for the $pp \rightarrow \tilde{g}\tilde{g}$ process, as a function of the gluino mass are shown in Fig. 2. This computation is done assuming: $m_{\tilde{g}} = m_{\tilde{q}} (y_1 \leq 1.5, \Lambda = 290 \text{ meV at } \sqrt{s} = 0.630, 2, 10, \text{ and } 40 \text{ TeV}$ and considering almost the full accessible p_T range (i.e. p_T goes from 10 to 500 GeV for $\sqrt{s} \geq 2 \text{ TeV}$ and p_T goes from 5 to 200 GeV for $\sqrt{s} = 0.630 \text{ TeV}$). We compare these results with these given by EHLQ^[11] under the same assumptions^[12]. As expected, a very good agreement between these two calculations is shown in Fig. 2. A similar check of the process $pp \rightarrow \tilde{g}\tilde{q}$ also gave good agreement. This gives us confidence that the results given by Isajet are quite compatible with EHLQ's expectations.

Moreover, this Monte Carlo program includes another section that we will use to study the standard background; Isajet incorporates perturbative QCD cross-sections, initial-state and final-state QCD radiative corrections in the leading-log approximation, independent fragmentation of quarks and gluons into hadrons, and a phenomenological model tuned to minimum-bias data for the beam jets (to fit in particular UA1 data). Apart from the hard scattering, which mainly leads to two high- p_T jets and includes $gg \rightarrow gg$, $gq \rightarrow gq$, and $gg \rightarrow q\bar{q}$, with the default structure functions of EHLQ^[11], the QCD radiative corrections are added to allow the possibility of many jets. This is essential in order to get the correct event structure, especially when going to higher energies.

The Drell-Yan production of W or Z^0 within the Standard Model is also included in this part of Isajet. For zero transverse momentum of the W , the process is simulated by $q\bar{q} \rightarrow W$. If non-zero limits on the transverse momentum of the W are

set, then the processes $q\bar{q} \rightarrow W + g$ and $qg \rightarrow W + q$ are simulated instead, including the full matrix element for the W decay. Similar tools are provided to simulate Z^0 production.

Isajet is for the moment the only general “realistic” Monte Carlo, offering a way of reproducing, at the same time, SUSY reactions and Standard Model processes. We are aware of the various limitations of such an approach; but we think this tool is good enough to at least give a first idea of whether or not, from an experimental point of view (i.e. introducing various experimental set-ups) we will be able to identify these possible new phenomena, and to extract them out of their corresponding standard backgrounds.

We are going to apply this uniform approach to the various following experimental set-ups: UA1 at the CERN $\bar{p}p$ collider, upgraded UA1 (with a finer-grained calorimetry) or UA2 (total 4π coverage by fine grained calorimetry) at ACOL (assuming an integrated luminosity 10 times higher than that recorded during 1981 to 1985 at CERN); the CDF detector at the Tevatron, assuming a luminosity first of 10^{36} cm^{-2} , then of 10^{39} cm^{-2} ; finally a fine-grained 4π calorimeter at the LHC or the SSC pp collider, with 10^{40} cm^{-2} integrated luminosity. These different items are discussed in the next sections. But, before describing them, let’s report on the cross-sections and the rates of events corresponding to each scenario.

2.3 Expected Rates and Cross-Sections at Various c.m. Energies and Integrated Luminosities

Cross-sections and rates are calculated with Isajet 5.25. The range in m_{mass} considered in each case is defined in Subsection 2.2 and in Fig. 1 (a, b). The cross-

sections are integrated over a p_T range for sparticles which goes from 10 to 110 GeV/c for the CERN $p\bar{p}$ collider, 20 to 200 GeV/c for the Tevatron, and 100 to 1000 GeV/c for super pp colliders. These p_T ranges can be lowered in the case of $m_{\tilde{g}} \ll m_{\tilde{q}}$ (as already mentioned in 2.1) to 2-20 GeV/c for $\sqrt{s} = 630$ GeV, 5-30 GeV/c for $\sqrt{s} = 2$ TeV, and 20-100 or 30-100 GeV/c for $\sqrt{s} = 17$ TeV and 40 TeV. Therefore, the generated events will always include a minimum value on the p_T of the primary partons (p_T^{\min}) which usually goes from 10 to 20 GeV/c (for $\sqrt{s} = 630$ GeV or 2 TeV, respectively) up to 100 GeV (for $\sqrt{s} = 17$ or 40 TeV).

The rates quoted here are calculated for an integrated luminosity of 715 nb^{-1} at $\sqrt{s} = 630$ GeV (corresponding to the total luminosity recorded on tape by the UA1 experiment until 1986 shutdown), 10^{39} cm^{-2} at $\sqrt{s} = 2$ TeV (which should be achieved provided an improvement of the Tevatron to increase the peak luminosity up to $5 \times 10^{31} \text{ cm}^{-2} \text{ s}^{-1}$). For the super pp colliders a total integrated luminosity of 10^{40} cm^{-2} per year is the present hypothesis of performance. The case of ACOL, with 10 times more integrated luminosity than the present score at CERN $p\bar{p}$ collider is treated separately in the next section. The case of 10^{36} cm^{-2} at $\sqrt{s} = 2$ TeV which could be reached by CDF experiment within the next forthcoming run (1988) is described in detail also in Section 3.

In Fig. 3 we present the results obtained for the case where $m_{\tilde{g}} < m_{\tilde{q}}$ at $\sqrt{s} = 0.63, 2, 17$, and 40 TeV; Fig. 3a and b show the behaviour of the cross-sections as a function of the gluino mass, with the quoted values of $m_{\tilde{g}}$ referring to the set of values $(m_{\tilde{g}}; m_{\tilde{q}})$ for $m_{\tilde{g}} < m_{\tilde{q}}$ considered in this work, for the elementary processes $pp \rightarrow \tilde{g}\tilde{g}, \tilde{g}\tilde{q},$ and $\tilde{q}\tilde{q}$ separately. We remark that at $\sqrt{s} = 17$ or 40 TeV, the cross-

sections differ by an order of magnitude and, as expected, $\sigma(pp \rightarrow \tilde{g}\tilde{g}) > \sigma(pp \rightarrow \tilde{g}\tilde{q}) > \sigma(pp \rightarrow \tilde{q}\tilde{q})$ in this case. At $\sqrt{s} = 2$ TeV, the elementary cross-sections may differ by three orders of magnitude.

The sum of all three elementary contributions for each \sqrt{s} are then reported in Fig. 3c. We see that the LHC and the SSC cross-sections for gluino mass above 200 GeV may differ by 1/2 or one order of magnitude. We also note the tremendous gain in cross-section obtained when going from 2 TeV to 17 or 40 TeV, for gluino masses above 200 GeV. In Fig 4a, we consider the elementary cross-sections for each value of \sqrt{s} corresponding to the case of degenerate masses. We plot them as a function of the smass. The quoted smasses refer to the set of values ($m_{\tilde{g}} \gtrsim m_{\tilde{q}}$) considered in this work. We note that as expected in this scenario, the elementary cross-sections are very similar. In Fig. 4b we plot the sum of the three contributions.

If we consider now the $\bar{p}p$ colliders such as the CERN machine or the Tevatron working with an integrated luminosity of $10^{36} \text{ cm}^{-2}/\text{year}$, i.e. the first generation of $\bar{p}p$ machines, a reasonable cross-section for the production of any new signal is of the order of the nanobarn. Such a level is obtained at the CERN $\bar{p}p$ collider for smasses of the order of 40 GeV, and at around 100 GeV for the Tevatron. The LHC or SSC pp colliders are expected to run at a luminosity of about 10^{40} cm^{-2} ; therefore, cross-sections of the order of the picobarn could be explored. This corresponds to smasses of the order of 1 TeV for these super pp colliders. This is a first, very rough, estimate of the kind of discovery limits which will be reachable by each machine.

An important part of our job is to define accurately these limits. Another way to express these numbers is by giving the various rates per year that may be expected

for each machine, in each theoretical framework we consider, and as a function of the smasses. In Fig. 5a we show the expected rates corresponding to the total integrated luminosity recorded at the CERN $\bar{p}p$ collider by the UA1 experiment. It shows that, in any case, above about 0(40 GeV), the rates drop dramatically below a few events which, as we will see later on, is too low to give any experimental evidence. Fig. 5b gives the rates for the degenerate-mass case at each considered value of \sqrt{s} , taking values of the integrated luminosity of $10^{40} \text{ cm}^{-2}/\text{year}$ at 17 and 40 TeV, 715 nb^{-1} at $\sqrt{s} = 0.63 \text{ TeV}$, and $1.5 \times 10^{39} \text{ cm}^{-2}$ at $\sqrt{s} = 2 \text{ TeV}$ (i.e. improved luminosity case). It is already important to note that, for smasses of the order of 1 TeV, the LHC will record about 10^5 events and the SSC about 10^6 events, whereas, at about 200 GeV mass, the LHC is expected to give about 10^8 events/year and the SSC again about 10 times more. The Tevatron with an integrated luminosity of $0(10^{39} \text{ cm}^{-2})/\text{year}$ will record about 10^3 to 10^4 SUSY events per year at 200 GeV and about 10^6 at 100 GeV mass range. We note that for the considered luminosity recorded so far by UA1 for events with large missing transverse energy (715 nb^{-1}), at 100 GeV the expected rate of SUSY events/year is only of order 10. Figure 5c represents the rates for the case $m_{\tilde{g}} < m_{\tilde{q}}$, within the same conditions for the luminosity than the ones defined for Figure 5b. For $m_{\tilde{g}} \sim 500 \text{ GeV}$ SSC gives about 10 times more events than LHC; for $m_{\tilde{g}} \sim 200 \text{ GeV}$ the Tevatron gives a few 10^3 events and about 10^6 events for $m_{\tilde{g}} \sim 100 \text{ GeV}$ (for an upgraded luminosity); UA1 only expects about 10 events under the same conditions and for 715 nb^{-1} . Finally in Fig. 5d, we represent the case of a very light gluino and a relatively heavy squark.

The main standard backgrounds generated with Isajet are the $2 \rightarrow 2$ QCD

process with light constituents and heavy quarks, the $2 \rightarrow 1$ Drell Yan process to produce W 's which then decay into $\tau\nu_\tau$ and Z^0 's decaying into $\nu\bar{\nu}$. As we will see in details in the next sections, these are the main sources of background as they may give rise also to a relatively fair amount of missing transverse energy.

We summarize in Table 1 the cross sections in mbarns of the different standard processes at different c.m. energies and for different values of the P_T^{\min} threshold applied to the P_T of the primary partons. It gives an idea of the small value of the ratio S/B before any cut is applied (but P_T^{\min} cut). In addition we show in Fig. (6) the E_T^{miss} distribution at the c.m. energy of the CERN $p\bar{p}$ collider provided by the standard backgrounds and two different Susy signals. Figure 6a and b shows the E_T^{miss} distribution for the decay of the W into $\tau\nu_\tau$ and for the QCD signal with different values of P_T^{\min} . Figure 6c, shows the same distribution for a Susy signal corresponding to low smasses (namely $m_{\tilde{g}} = 35$ GeV and $m_{\tilde{q}} = 80$ GeV), and a Susy signal corresponding to high smasses (namely: $m_{\tilde{g}} = 84$ GeV and $m_{\tilde{q}} = 80$ GeV) It clearly shows how low P_T QCD events will perturb low smass signals whereas the higher P_T tail plus W 's and Z^0 's will mainly disturb higher smass signals.

Several orders of magnitude enhancement of S/B must be accomplished to detect supersymmetric signals. This is the main goal we will attempt to reach in the next sections.

Table 1: Expected Contributions from Standard Background in various pp Colliders. Cross-sections are in millibarns.

<u>Background</u>	<u>ACOL</u>	<u>Tevatron</u>	<u>LHC</u>	<u>SSC</u>
QCD				
$p_T^{jet} > \text{in GeV}$				
10	.117	0.737		
20	$.49 \times 10^{-2}$	0.57×10^{-1}		
50	$.26 \times 10^{-4}$	0.11×10^{-2}		
80	$.8 \times 10^{-6}$	$.088 \times 10^{-4}$		
100	$.11 \times 10^{-6}$	0.23×10^{-4}	0.37×10^{-2}	0.13×10^{-1}
100			1.2×10^{-4}	5.0×10^{-4}
300			2.8×10^{-6}	1.7×10^{-4}
500			0.2×10^{-6}	0.18×10^{-4}
$W \rightarrow \tau \nu$				
$p_T^W > \text{in GeV}$				
10	$.51 \times 10^{-7}$	0.46×10^{-6}		
20	$.15 \times 10^{-7}$	0.20×10^{-6}	0.38×10^{-6}	0.10×10^{-4}
50	$.98 \times 10^{-9}$	0.27×10^{-7}	0.97×10^{-6}	0.024×10^{-4}
100	$.23 \times 10^{-10}$	0.30×10^{-8}	0.018×10^{-6}	0.0067×10^{-4}
300			0.43×10^{-8}	0.20×10^{-7}
$Z^0 \rightarrow \nu \bar{\nu}$				
$p_T^Z > \text{in GeV}$				
10	$.43 \times 10^{-7}$	0.4×10^{-6}		
20	$.13 \times 10^{-7}$	0.16×10^{-6}	0.29×10^{-6}	0.92×10^{-6}
50	$.10 \times 10^{-8}$	0.27×10^{-7}	0.73×10^{-6}	0.02×10^{-4}
100	$.22 \times 10^{-10}$	0.28×10^{-8}	0.018×10^{-6}	0.0061×10^{-4}
300			0.4×10^{-8}	0.19×10^{-7}

We have summarized in this section what are the main expectations given by the program which generates the processes, and the different hypotheses we want to study. We jump now from the world of partons to the real world. This real world is obtained by simulating these reactions inside the various detectors which are installed at the different pp machines. We start with the UA1 experiment at the CERN $\bar{p}p$ collider which represents the “low-mass” range.

3. SUSY at the CERN $\bar{p}p$ Collider

The UA1 experiment^[13] is a pioneering detector for pp machines. It is characterized by a 4π hermetic calorimetry (including both e.m. and hadronic parts) , a muon detector covering the whole apparatus down to 15 degrees with respect to the beam axis and a very precise central tracking with a dipole magnetic field of 0.7 Tesla. Using many of these properties, the so-called “missing-energy technique”, has been developed to measure and analyze events where ν or ν -like particles are produced^[14].

3.1 Missing-Energy Technique in the UA1 Detector

It is important to note first that in $\bar{p}p$ (or pp) colliders, it is not possible to measure properly the total missing energy of an event, but only its transverse component: E_T^{miss} . This is clear when looking at the plots of Fig. 7 where we note that owing to the beam jets produced in such collisions, a large fraction of the energy is lost in the beam pipe. Thus the component of the energy along the beam axis is very badly measured. We are then restricted to defining a transverse missing energy, by considering the component along the two axes in the plane perpendicular to the

beam axis (i.e. components E_y and E_z). By projecting the energy of each calorimeter i cell onto the transverse plane, we obtain the transverse energy vector E_{Ti} given by:

$$\vec{E}_{Ti} = \vec{E}_{Yi} - \vec{E}_{Zi}$$

The corresponding total transverse energy E_T^{tot} of the event is defined as the scalar sum of the transverse energies of all i -cells:

$$E_T^{\text{tot}} = \sum_i |\vec{E}_{Yi} + \vec{E}_{Zi}|$$

and the total transverse missing energy is given by:

$$E_T^{\text{miss}} = -E_T^{\text{tot}} = -\sum_i |\vec{E}_{Ti}|$$

This method may be applied if, and only if, the calorimeter is really 4π and hermetic. In the case of the UA1 detector, “good 4π coverage” is ensured by the central, forward, and very forward calorimetry which covers the range down to 2 degrees with respect to the beam axis and by a muon-detector (able to detect muons down to about 15 degrees from the beam axis) plus a good handling of the cracks and dead region (which are inevitable in any 4π -detector technology). There is in the UA1 detector a main dead region: it is defined as a cone of ± 15 degrees around the vertical up and down axis in the central calorimeter (covering the region in pseudorapidity η defined by $|\eta| \leq 1.5$). This dead zone is due to the separation into two gondola hemispheres. Some energy may flow in this region without being detected by the calorimeter. However, this leakage may be detected by the central detector (CD) (which is able to see at least, the charged component of this possible energy flow).

This information from the CD may be used to tag a good fraction of the so-called vertical events. This is taken into account in the validation of the total missing transverse energy measured in an event.

Moreover, an estimate of the resolution on E_T^{miss} has been made by measuring the resolution on E_T^{tot} on a sample of minimum-bias data and of high E_T^{jet} triggers. The result is plotted in Fig. 7b: the resolution on E_T^{miss} derived from this measurement is given by $\sigma = 0.7\sqrt{E_T^{\text{tot}}}$. This parameter is used to validate the transverse missing energy measured in an event: a cut, which is a function of σ , is applied to E_T^{miss} . We will consider, in this analysis, two types of cuts¹⁴: a loose cut, which is equivalent to 2.5σ , and a tight cut, which corresponds to 4σ .

The missing-energy technique was first used in UA1 to search for $W \rightarrow e\nu$ events. It has then been extended to study other processes which also produced ν '(s) or ν -like particles. This is what we are considering now.

3.2. Definition of the Missing-Energy Selection in UA1

Until 1984, no missing energy first-level trigger was set. From 1984 on, a missing energy cut has been introduced both at the first level (i.e. in the hardware processor) and at the second level (i.e. using on-line 168E or 3081E emulators). It is done by requesting an imbalance in the total transverse energy of at least 17 GeV between the left and right sides of the central calorimeter, together with at least one jet; in the trigger processor, a jet is defined as a minimal amount of 15 GeV of transverse energy deposited in eight adjacent e.m. cells and the two hadronic cells behind. The estimate of E_T^{miss} in the first-level trigger is biased by the left-right symmetry of the central e.m. calorimetry in UA1 (so-called gondolas).

At the second-level trigger, the on-line emulators recompute E_T^{miss} by using the information provided by all the calorimeter cells in the apparatus; a cut on E_T^{miss} of 3.5σ (where $\sigma = 0.7\sqrt{E_T^{\text{tot}}}$) is applied on these data.

Apart from this on-line selection of missing-energy events, an off-line filter is applied on all the recorded data (i.e. the 10 million triggers which correspond to the total integrated luminosity of 715 nb^{-1}). It is this selection which finally retains 1% to 2% of the data which represents the complete sample of missing-energy data. It includes all the different types of triggers which may be set by the first-level trigger. It also implies that all these data have been completely preprocessed, which means that the calorimetric information has been fully reconstructed (including all the constants of calibration, bookkeeping of dead channels, etc.) It retains, independently of the first-level trigger bit, each event which has a computed transverse missing energy of 15 GeV and validated at 2σ .

It also rejects spurious events such as cosmic rays and beam halo, which fake the missing-energy events. We show in Fig. 8 a diagram of the complete data selection from the on-line trigger to the off-line filter.

Let us now discuss in more detail the three types of filters we will use and finally analyze here. The filter labelled “ 4σ ” corresponds to an inclusive selection of data after requiring a tight cut on the total missing transverse energy (i.e. $E_T^{\text{miss}} > 4\sigma$). The filter “ 2.5σ no b/b” is defined by requiring the loose cut on E_T^{miss} (i.e. $E_T^{\text{miss}} > 2.5\sigma$) but constraining strongly the requirement on the “non-activity” in the region back to the highest E_T jet in the event. This is done first by demanding that there be no jet, either in the calorimeter or in the CD, back to the trigger jet of

the event. In addition, the sum of all E_T -cell or of all tracks, in a cone in ΔR of 0.4 around the axis back to the axis of the trigger jet is required to be less than a few GeV (6 and 4, respectively). This restrict the possible event topologies to monojet or bijet non-back-to-back. The filter "4 σ no b/b" is defined in the same way as the previous filter, but requiring a tight cut on E_T^{miss} instead of the loose one. The cuts on the non-back-to-back activity were very important, in the case of the UA1 experiment, to beat the major background, that generated by: $W \rightarrow \tau \nu_\tau$ events. We will see below how these filters bias the search for SUSY particles. But before that, let us recall the main results obtained by the UA1 collaboration^[14]. These results are summarized in Table 2.

Table 2: Expected Contributions from the Standard Background to UA1 Experiment (corresponding to 715 nb⁻¹)

Background process	Expected contribution (#. of events)	
	for all data (56 events)	for $L_{\tau^+} < 0$ data (24 events)
$W \rightarrow \tau \nu_\tau \rightarrow \text{hadrons}$	36.7 ± 1.8	8.0 ± 1.0
All leptonic decays of W or Z^0 (except $W \rightarrow \tau \nu \rightarrow \text{hadrons}$)	11.5 ± 1.3	9.2 ± 1.2
Heavy flavour (b, c) production from $p\bar{p} \rightarrow Q\bar{Q}$ and from W and Z^0 decays	0.3 ± 0.8	0.2 ± 0.8
QCD jet-jet fluctuations	3.8 ± 1.7	3.4 ± 1.7
Total	52.3 ± 2.5	20.8 ± 2.0

This table shows that the contribution of all the standard background is 52.3

± 2.4 ; This number corresponds to the 56 events selected from all the data recorded between 1983 and 1985 by the UA1 detector and corresponds to a tight cut on E_T^{miss} plus a requirement on the non-back-to-back activity. Therefore, not much room is left for anything but a standard model explanation for these events.

Anyhow, this result is already important to set limits on the smasses which could have been detected in this experiment according the various scenarios we have studied.

3.3-1 Effect of the Filters on the Rates of Expected Events

We have given at the end of section 2, in Fig. 5, the rates of expected events according to Isajet, for the various scenarios applied to the case of the UA1 detector working at the CERN $\bar{p}p$ collider and recording a total of 715 nb^{-1} . In Table 3, we show how these numbers are changed when applying the different filters (including also the trigger). This table describes in detail the different scenarios which have been considered for the CERN $\bar{p}p$ collider and lists the results for each elementary process. It is divided in three parts: Table 3a concerns the various cases where the gluino and squark masses are non-degenerate ($m_{\tilde{g}} < m_{\tilde{q}}$). In Table 3b, we report one example with a very light gluino and a relatively very heavy squark ($m_{\tilde{g}} \ll m_{\tilde{q}}$): $m_{\tilde{g}} = 10 \text{ GeV}$ and $m_{\tilde{q}} = 100 \text{ GeV}$. In this special case, we look at both the dominant decay mode of the squark into $q\tilde{g}$ (about 93% of branching ratio) and the case where $\tilde{q} \rightarrow q\tilde{\gamma}$ (which represents about 7% of the branching ratio). Finally Table 3c summarizes the case where the gluino and squark are almost degenerate in mass ($m_{\tilde{g}} \gtrsim m_{\tilde{q}}$). In this last case, the rates between each of the

Mass ₂ (GeV/c ²)	Process Decay mode	Expected rates (No. of events)	Percentage of events passing each filter		
			Trigger	4σ inclusive	2.5σ non-b/b
$m_{\tilde{g}} = 21$	$\bar{p}p \rightarrow \tilde{g}\tilde{g}$	63635	24	4.5	4.5
$m_{\tilde{q}} = 19$	$\bar{p}p \rightarrow \tilde{g}\tilde{g}$	47548	26	3	3
	$\bar{p}p \rightarrow \tilde{q}\tilde{q}$	85136	23.2	4	3.5
$m_{\tilde{g}} = 42$	$\bar{p}p \rightarrow \tilde{g}\tilde{g}$	1358	67	26	9.2
$m_{\tilde{q}} = 40$	$\bar{p}p \rightarrow \tilde{g}\tilde{g}$	1537	62	24	10.2
	$\bar{p}p \rightarrow \tilde{q}\tilde{q}$	1573	63	24	11.5
$m_{\tilde{g}} = 63$	$\bar{p}p \rightarrow \tilde{g}\tilde{g}$	69	89	51	9.9
$m_{\tilde{q}} = 57$	$\bar{p}p \rightarrow \tilde{g}\tilde{g}$	136	83	47	11
	$\bar{p}p \rightarrow \tilde{q}\tilde{q}$	207	84	45	12.4
$m_{\tilde{g}} = 73.5$	$\bar{p}p \rightarrow \tilde{g}\tilde{g}$	19	93	55	6
$m_{\tilde{q}} = 66.5$	$\bar{p}p \rightarrow \tilde{g}\tilde{g}$	37	88	51	6.1
	$\bar{p}p \rightarrow \tilde{q}\tilde{q}$	79	90	49	6.9
$m_{\tilde{g}} = 84$	$\bar{p}p \rightarrow \tilde{g}\tilde{g}$	4.7	97	48.5	7.6
$m_{\tilde{q}} = 80$	$\bar{p}p \rightarrow \tilde{g}\tilde{g}$	10.7	95	64	12
	$\bar{p}p \rightarrow \tilde{q}\tilde{q}$	20	93	62	16

Table 3a : No - Degenerate Mass Scenarios, rates and effect of the various filters.

Mass (GeV/c ²)	Process mode	Expected rates (No. of events)	Percentage of events passing each filter		
			Trigger	4σ inclusive	2.5σ non-b/b
$m_{\tilde{g}} = 20$	$\bar{p}p \rightarrow \tilde{g}\tilde{g}$	85800	20	2	2.5
$m_{\tilde{q}} = 30$	$\bar{p}p \rightarrow \tilde{g}\tilde{g}$	20520	35	1	0
	$\bar{p}p \rightarrow \tilde{q}\tilde{q}$	6650	44	2	2
$m_{\tilde{g}} = 25$	$\bar{p}p \rightarrow \tilde{g}\tilde{g}$	28600	33	3.5	2
$m_{\tilde{q}} = 50$	$\bar{p}p \rightarrow \tilde{g}\tilde{g}$	3074	55	3.9	0.5
	$\bar{p}p \rightarrow \tilde{q}\tilde{q}$	500	78	3.9	0.5
$m_{\tilde{g}} = 40$	$\bar{p}p \rightarrow \tilde{g}\tilde{g}$	1716	63	9.3	1.4
$m_{\tilde{q}} = 60$	$\bar{p}p \rightarrow \tilde{g}\tilde{g}$	566	76	9.8	1.4
	$\bar{p}p \rightarrow \tilde{q}\tilde{q}$	171	88	8.6	0
$m_{\tilde{g}} = 50$	$\bar{p}p \rightarrow \tilde{g}\tilde{g}$	307	85	18.3	2.9
$m_{\tilde{q}} = 100$	$\bar{p}p \rightarrow \tilde{g}\tilde{g}$	32	97	17.	0.27
	$\bar{p}p \rightarrow \tilde{q}\tilde{q}$	3.7	100	19	0
$m_{\tilde{g}} = 60$	$\bar{p}p \rightarrow \tilde{g}\tilde{g}$	93	83	18.6	1.5
$m_{\tilde{q}} = 80$	$\bar{p}p \rightarrow \tilde{g}\tilde{g}$	44	90	23	1.5
	$\bar{p}p \rightarrow \tilde{q}\tilde{q}$	23	83.5	22	0

Table 3 b : Degenerate Mass Scenarios, rates and effect of the various filters.

Table 3: Effect of the various filters (trigger included) on the rates of expected

events for the cases a) where $m_{\tilde{g}} < m_{\tilde{q}}$ and b) $m_{\tilde{g}} \geq m_{\tilde{q}}$.

elementary processes remain comparable even after each filter. On the other hand, in the case represented in Table 3a, the production of gluino pairs (which is lighter than the squark) is dominant by about one order of magnitude compared to $\bar{g}\bar{q}$, and by two orders of magnitude compared to $\bar{q}\bar{q}$.

The different filters which impose a cut on E_T^{miss} strongly affect all these cases. In particular, by applying the 4σ inclusive cut on E_T^{miss} in the case where $m_{\tilde{g}} < m_{\tilde{q}}$ and where the smasses are lighter than the W mass (m_W), only a few percent of this events remain, and at most 20% if the smasses are of the order of m_W . If $m_{\tilde{g}} \sim m_{\tilde{q}}$, this filter strongly affects the low-mass case (i.e. when $m_{\tilde{g}} \sim m_{\tilde{q}} \sim 20$ GeV): this effect decreases when the smasses become larger. When $m_{\tilde{g}} \sim m_{\tilde{q}} \sim 40$ GeV, 25% of these events pass the filter, and when $m_{\tilde{g}} \sim m_{\tilde{q}} \sim m_W$, more than 50% of the events remain after this cut is applied. If $m_{\tilde{g}} \ll m_{\tilde{q}}$, the cuts on E_T^{miss} have a drastic effect if $\bar{q} \rightarrow q\bar{g}$ (only at most few per cent of such events pass these cuts), but if $\bar{q} \rightarrow q\tilde{\gamma}$ the corresponding events are much less sensitive to these cuts. It is also important to note that the cut on E_T^{miss} that also requires no-back-to-back activity is a very strong cut, both for $m_{\tilde{g}} < m_{\tilde{q}}$ and $m_{\tilde{g}} \gtrsim m_{\tilde{q}}$; only a few percent of these events survive, independently of the values of the smasses.

Finally, we note that in all these cases, the elementary processes behave in almost the same way with respect to these various E_T^{miss} filters. All these results are summarized in Fig. 9a and b, for the cases with $m_{\tilde{g}} < m_{\tilde{q}}$ and $m_{\tilde{g}} \gtrsim m_{\tilde{q}}$.

3.3-2 Characteristics of the SUSY Events in the UA1 Detector

We first show displays of some typical SUSY events as they would appear in the UA1 detector if the scenarios we have imagined were real. For this purpose, a complete

simulation of the UA1 detector has been applied to various processes generated by the Isajet Monte-Carlo. In Fig. 10. we present views of an event generated by the process $pp \rightarrow \tilde{g}\tilde{q}$ with $m_{\tilde{g}} = 21$ GeV and $m_{\tilde{q}} = 19$ GeV; it appears as a clear monojet event with an E_T of 33 GeV measured by the calorimetry and a p_T of 6.4 GeV/c in the CD (four charged tracks). The missing transverse energy of 27.4 GeV balances quite well the E_T of the jet. In Fig. 11, 12. and 13. we show various jet topologies generated by the same process, $pp \rightarrow \tilde{g}\tilde{q}$, with $m_{\tilde{g}} = 63$ GeV and $m_{\tilde{q}} = 57$ GeV. The decay modes are $\tilde{g} \rightarrow \bar{q}q$ and $\tilde{q} \rightarrow q\tilde{\gamma}$. In Fig. 11. we show a typical monojet, generated by this process. The jet has 40.3 GeV in E_T and 15.7 GeV/c in p_T , with a multiplicity of five charged tracks; an E_T^{miss} of 27.5 GeV balances this jet. Such a process may also generate clear non back-to-back bijets such as the one presented in the views of Fig. 12. One of the two jets has an E_T of 40.8 GeV measured by the calorimetry and 47.8 GeV/c measured in the CD (with six charged tracks). The second jet has an E_T of 39 GeV and 32 GeV/c of p_T . The difference in azimuthal angle between the two jets is of about 130 degrees. A total missing transverse energy of 28.9 GeV is measured in this event. In Fig. 13. we show a trijet event, again generated by the same process. The E_T of each of these jets is respectively 49.7 GeV, 22.1 GeV, and 20.1 GeV, and there is a total missing transverse energy of 32 GeV. The various pictures presented so far correspond to the case where $m_{\tilde{g}} \gtrsim m_{\tilde{q}}$. In Fig. 14 we present a monojet event generated by the process $pp \rightarrow \tilde{g}\tilde{q}$, with $\tilde{g} \rightarrow q\bar{q}\tilde{\gamma}$ and $m_{\tilde{g}} = 10$ GeV, $\tilde{q} \rightarrow q\tilde{\gamma}$ and $m_{\tilde{q}} = 100$ GeV. The jet has an E_T of 46.4 GeV and a p_T of 23.3 GeV/c, balanced by an E_T^{miss} of 42.8 GeV.

These various pictures show first that SUSY processes in the scheme we have

adopted here may generate very clean mono- or multi-jet topologies, with a fair amount of missing transverse energy; secondly, it shows that various types of processes may generate the same kind of topologies, but also that the same process may generate various types of jet topologies. These facts will be explained in the next subsection. For now we will study the main features of the different characteristics which describe the events. Among these quantities, we consider here: the total missing transverse energy (E_T^{miss}), the number of jets in an event (with $E_T^{\text{jet}} > 15$ GeV and applying the standard UA1 jet algorithm^[15]), the transverse energy of the trigger jet in the event (E_T^{jet}).

For a detailed study of the number of jets in the events (i.e. the jet topology), we refer to the next subsection. The other two parameters are displayed in Fig. 15 to 18. In Fig. 15a, are plotted the average values of the E_T of the trigger jet, $\langle E_T^{\text{jet}} \rangle$, for all the cases considered in this study. Fig. 15b shows the average values of E_T^{miss} for each studied scenario. In Fig. 16a, we show the evolution of the E_T^{jet} spectrum as a function of the smasses when they increase from 20 to 80 GeV, in the case where $m_{\tilde{g}} < m_{\tilde{q}}$. Fig. 16b presents the corresponding evolution of the E_T^{miss} spectrum. Fig. 17a shows the evolution of the E_T^{jet} spectrum when the smasses vary from 20 to 80 GeV and $m_{\tilde{g}} \gtrsim m_{\tilde{q}}$. Fig. 17b shows the corresponding E_T^{miss} spectra. Finally, Figures 18a and b show the E_T^{jet} and E_T^{miss} spectra in the case of a very light gluino and a very heavy squark, considering both decays of squark (i.e. $\tilde{q} \rightarrow q\tilde{g}$ and $\tilde{q} \rightarrow q\tilde{\gamma}$). In this last scenario, the main point to note is the E_T^{miss} distribution which, for $\tilde{q} \rightarrow q\tilde{g}$ has an average value of 15 GeV, whereas, in the case of $\tilde{q} \rightarrow q\tilde{\gamma}$ is larger than 30 GeV. The E_T^{jet} distributions are roughly the same. In the case where $m_{\tilde{g}} < m_{\tilde{q}}$, the three

elementary processes give different values for $\langle E_T^{\text{jet}} \rangle$ (especially if the difference in mass between gluino and squark is rather large, as for instance in the case $m_{\tilde{g}} = 50$ GeV and $m_{\tilde{q}} = 100$ GeV) The process $pp \rightarrow \tilde{q}\tilde{g}$ gives, of course, the highest values. When $m_{\tilde{g}} \gtrsim m_{\tilde{q}}$, each elementary process gives roughly the same value for both parameters $\langle E_T^{\text{jet}} \rangle$ and $\langle E_T^{\text{miss}} \rangle$; $\langle E_T^{\text{miss}} \rangle$ is slightly higher in this case than when $m_{\tilde{g}} > m_{\tilde{q}}$, in particular when smasses are reaching values towards m_W .

We will now use these main features of the SUSY events to investigate the “typical SUSY signatures” that one may expect in the UA1 detector and also the way they evolve when applying the various E_T^{miss} filters used in this experiment.

3.3-3 SUSY Signal at UA1.Explanation of the jet pattern

Processes (1), (2), and (3) are mainly “hadronic processes”. This implies that one of the main features of these events is their jet pattern. Another important feature of these events is the amount of missing transverse energy produced by the emission of the $\tilde{\gamma}$ (’s). These are the two striking aspects of the signature of the events we are looking for. We have already explained how some filters have been developed to select events with large E_T^{miss} .

To identify the jet pattern of the events, a program has been built that classifies the events according to their jet structure^[16]. First we consider the events with only one jet with $E_T > 15$ GeV and a minimal amount of transverse momentum: $P_T/E_T > 10\%$. In addition to this trigger jet,

Table 3 and Table 4 for the case where $m_{\tilde{g}} \ll m_{\tilde{d}}$

Mass ₂ (GeV/c ²)	Process Decay mode	Reaction	Expected rates * (No. of events)	Percentage of events passing each filter		
				Trigger	4 σ inclusive	2.5 σ non-b/b
$m_{\tilde{g}} = 10$	$\tilde{g} \rightarrow q\bar{q}$	$p\bar{p} \rightarrow q\bar{q}$	665	89	7.8	0
$m_{\tilde{q}} = 100$	$\tilde{q} \rightarrow q\bar{q}$					0
$m_{\tilde{g}} = 10$	$\tilde{g} \rightarrow q\bar{q}$	$p\bar{p} \rightarrow q\bar{q}$	50	86	64	19.9
$m_{\tilde{q}} = 100$	$\tilde{q} \rightarrow q\bar{q}$					17.5

Table 3b : Very light gluino and heavy squark scenarios, rates and effect of the various filters.

Decay mode	Filter No	Monojets %	Monojets b/b %	Bijets b/b %	Bijets non b/b %	≥ 3 jets %
$\tilde{q} \rightarrow q\bar{q}$	1	2.6	10.2	39	11	25.5
	2	4.6	15.6	9.3	10.9	12.5
$\tilde{q} \rightarrow q\bar{q}$	1	27.6	14.5	8.6	25	8.5
	2	23	15	4	19	7

Table 4b : Various Jet topologies for events with no filter (i.e. filter 1) or 4 σ inclusive filter (i.e. filter 2) applied for the very light gluino and heavy squark scenarios

small- E_T jets (i.e $7 \leq E_T^{\text{jet}}$ (GeV) ≤ 15) can be part of this kind of events, provided they are not back in azimuth to the trigger jet within a cone in $\Delta R \leq 0.4$. Such events are called “monojet” events. If one of the possible additional small E_T jet is back in azimuth to the trigger jet, the program classifies this event as “MONOJET with activity back”. If there is a second jet in the event with $E_T \geq 15$ GeV, it is referred to as a BIJET event. If these two highest E_T jets are opposite in azimuth, the event is called “BIJET back-to-back”. Otherwise, it is called a “BIJET non back-to-back”. Again in this type of events, additional small E_T jets with $E_T < 15$ GeV are allowed without changing the label of the corresponding pattern. Each time the program finds in the event another jet with $E_T > 15$ GeV, the label of the corresponding jet pattern is increased by one. Therefore the various multijet structures are classified this way.

For each scenario, we have studied the jet topology obtained and the effect of an E_T^{miss} filter on it. The results are summarized in Table 4: the percentage of events having a certain jet pattern, and the evolution for each scenario (i.e: $m_{\tilde{g}} \ll m_{\tilde{q}}$, $m_{\tilde{g}} < m_{\tilde{q}}$ and $m_{\tilde{g}} \gtrsim m_{\tilde{q}}$) when changing the smasses. Also reported in this Table is the change in the jet structure when applying a tight cut on E_T^{miss} (filter 2) or not (Filter 1). In the case of $m_{\tilde{g}} \ll m_{\tilde{q}}$, reported in Table 4b, it is interesting to note that, if $\tilde{q} \rightarrow q\tilde{g}$ and no filter is applied, the dominant jet topology is given by two jets back in azimuth (39% bijets b/b + 10% monojets b/b), then the multijet topology gives 25%, only 11% of bijets no b/b, and almost no monojets at all. For $\tilde{q} \rightarrow q\tilde{\gamma}$, the amount of back to back topologies is much less (only 8,6% of bijets b/b + 14% of monojets with b/b activity) and, on the contrary, there is a large proportion of bijets

no b/b and real monojets (about 25% of each), and much less multijets (only about 8.5%). A tight cut on E_T^{miss} does not really affect the decay $\bar{q} \rightarrow q\bar{\gamma}$ whereas it has a strong effect when $\bar{q} \rightarrow q\bar{g}$, as it cuts drastically the b/b structure and keeps the bijets no b/b and multijets at roughly the same level (i.e. about 10% each one).

The case where $m_{\tilde{g}} \gtrsim m_{\tilde{q}}$ is reported in Table 4a. We note, in this scenario, that if the smasses are near 20 GeV the dominant jet structure are the monojets; this effect is still accentuated by applying the tight cut on E_T^{miss} , about 50% of the remaining events are monojets and almost no bijets or trijets are left. At 40 GeV, monojets and bijets non b/b are at the same level (about 15 to 20% before the tight cut and 20 to 30% after the cut is applied); multijets appear at the few per cent level. When going to higher smasses (i.e. 60 or 80 GeV), the bijets non b/b dominate (40 to 50%), monojets are present to the order of 20 to 15% whereas the number of multijets increases up to about 10%. So when increasing from 20 to 80 GeV, the jet pattern change from about 50% of monojets to 50% of bijets no b/b and each of the three elementary processes behaves in roughly the same way.

If $m_{\tilde{g}} < m_{\tilde{q}}$, the results depend on whether or not these two masses differ by a fair amount. A striking feature is that when going from 20 GeV to 80 GeV, the percentage of multijet structure increases dramatically from about 3% to 30%, becoming predominant in the case of $\tilde{g}\bar{q}$ and $\bar{q}\bar{q}$ processes. The other jet patterns remain at the level of the few per cent or at most 10%.

In this scenario, the jet topology provided by each elementary process differs, especially when the difference between $m_{\tilde{g}}$ and $m_{\tilde{q}}$ becomes larger.

Table 4: Effect on the jet pattern of applying or not a cut on E_T^{miss} , a) in the case where $m_{\tilde{g}} \geq m_{\tilde{q}}$ or b) in the case where $m_{\tilde{g}} < m_{\tilde{q}}$

Mass GeV	Filter No	Monojets %	Monojets b/b %	Bijets b/b %	Bijets non b/b %	≥ 3 jets %
$m_{\tilde{g}} = 21$ $m_{\tilde{q}} = 19$	1	15	10	18.5	8.5	2
	2	50	-	-	-	-
$m_{\tilde{g}} = 42$ $m_{\tilde{q}} = 40$	1	18.5	10.6	17.7	22.3	3.6
	2	34	4.6	4.1	19.3	4
$m_{\tilde{g}} = 63$ $m_{\tilde{q}} = 57$	1	11.5	9	19	37	13.6
	2	9.6	7.4	6.3	35	5.3
$m_{\tilde{g}} = 73.5$ $m_{\tilde{q}} = 66.5$	1	5	6	6.5	31.6	17.6
	2	8.5	4.9	2.4	25.6	13.4
$m_{\tilde{g}} = 84$ $m_{\tilde{q}} = 80$	1	11.5	7.6	14	36	7.8
	2	13.5	6.3	3.6	45	9.4

Table 4a : Various Jet topologies for events with no filter (i.e. filter 1) or 4 σ inclusive filter (i.e. filter 2) applied for the degenerate mass scenarios.

Mass GeV	Filter No	Monojets %	Monojets b/b %	Bijets b/b %	Bijets non b/b %	≥ 3 jets %
$m_{\tilde{g}} = 20$ $m_{\tilde{q}} = 30$	1	9	7	16	10.5	4
	2	-	-	50	-	-
$m_{\tilde{g}} = 25$ $m_{\tilde{q}} = 50$	1	5.3	14.4	19.4	20.4	1.7
	2	6.2	25	9.3	9.3	3.1
$m_{\tilde{g}} = 40$ $m_{\tilde{q}} = 60$	1	4.5	8.6	22	21	23
	2	9.2	9.2	7.9	19.1	10.5
$m_{\tilde{g}} = 50$ $m_{\tilde{q}} = 100$	1	1.1	-	1.6	15.8	8.9
	2	-	2.1	5.5	8.7	7.6
$m_{\tilde{g}} = 60$ $m_{\tilde{q}} = 80$	1	1.5	5.6	15.2	14.7	35.5
	2	-	4.4	2.2	11.1	22.2

Table 4b : Various Jet topologies for events with no filter (i.e. filter 1) or 4 σ inclusive filter (i.e. filter 2) applied for the non - degenerated Mass scenarios

In conclusion, the degenerate-mass case provides easier jet patterns, essentially monojets or bijets non b/b , and a fair amount of E_T^{miss} . The case $m_{\tilde{g}} < m_{\tilde{q}}$, on the contrary, gives trickier structures, with a large contamination of back-to-back signatures and in general less E_T^{miss} . The special case where $m_{\tilde{g}} \ll m_{\tilde{q}}$ and $\tilde{q} \rightarrow q\tilde{\gamma}$ provides events with spectacular features in terms of monojet structure balanced by a fair amount of E_T^{miss} .

It is interesting to push a little bit more this study on the jet-pattern of the events. What we have seen so far is that, the definition of the jet-pattern by simply counting the number of partons emitted in the considered process is really too much naive ! and, part of the time just wrong; We have already seen that the same process (for instance $pp \rightarrow \tilde{g}\tilde{q}(\tilde{g} \rightarrow \tilde{q}\tilde{q} \text{ and } \tilde{q} \rightarrow q\tilde{\gamma})$) may produce different jet-patterns (see Fig. 11, 12 and 13), and not only 3 “jets” events. We have also shown how filters may favor specific jet topologies; moreover, a recent study^[17] shows how the jet-pattern depends upon the decay product angle and the gluon bremssthalung. We are going to study here how the kinematics of a process, influences the jet-pattern of the events it produces.

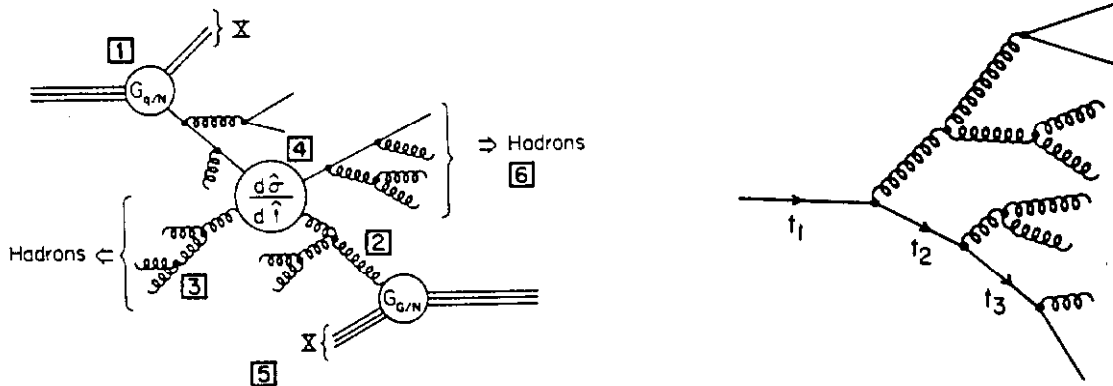
We start with the analytical expression of the matrix elements of the elementary process: $q, g \rightarrow \tilde{g}\tilde{g}$ as it is given at the parton level in Isajet Monte-Carlo, and in fact directly derived from EHLQ^[11].

$$\begin{aligned} \frac{d\sigma}{dt}(q\bar{q} \rightarrow \tilde{g}_1\tilde{g}_2) = & \frac{\pi}{\hat{s}^2} \left[\frac{8}{3} \alpha_s^2 \delta_{qq'} \frac{(\hat{t} - m_{\tilde{g}}^2)^2 + (\hat{u} - m_{\tilde{g}}^2)^2 + 2m_{\tilde{g}}^2 \hat{s}}{\hat{s}^2} \right. \\ & + \frac{32}{27} \alpha_s^2 \delta_{qq'} \frac{(\hat{t} - m_{\tilde{g}}^2)^2}{(\hat{t} - m_{\tilde{q}}^2)^2} - \frac{32}{27} \alpha_s^2 \delta_{qq'} \frac{(\hat{u} - m_{\tilde{g}}^2)^2}{(\hat{u} - m_{\tilde{q}}^2)^2} + \left. \frac{8}{3} \alpha_s^2 \delta_{qq'} \frac{(\hat{t} - m_{\tilde{g}}^2)^2 + m_{\tilde{g}}^2 \hat{s}}{\hat{s}(\hat{t} - m_{\tilde{q}}^2)} \right] \end{aligned}$$

$$\begin{aligned}
& + \frac{8\alpha_s^2}{27} \delta_{qq'} \frac{m_g^2 \hat{s}}{(\hat{t} - m_q^2)(\hat{u} - m_q^2)} + \frac{8\alpha_s^2}{3} \delta_{qq'} \frac{(\hat{u} - m_g^2)^2 + m_g^2 \hat{s}}{\hat{s}(\hat{u} - m_g^2)} \Big] \\
\frac{d\sigma}{d\hat{t}} (gg \rightarrow \bar{g}g) = & \\
& \frac{9\pi\alpha_s^2}{4\hat{s}^2} \left[\frac{2(\hat{t} - m_g^2)(\hat{u} - m_g^2)}{\hat{s}^2} \right. \\
& + \frac{(\hat{t} - m_g^2)(\hat{u} - m_g^2) - 2m_g^2(\hat{t} + m_g^2)}{(\hat{t} - m_g^2)^2} + \frac{(\hat{t} - m_g^2)(\hat{u} - m_g^2) + m_g^2(\hat{u} - \hat{t})}{\hat{s}(\hat{t} - m_g^2)} \\
& + \frac{(\hat{u} - m_g^2)(\hat{t} - m_g^2) - 2m_g^2(\hat{u} - m_g^2)}{(\hat{u} - m_g^2)^2} + \frac{(\hat{u} - m_g^2)(\hat{t} - m_g^2) + m_g^2(\hat{t} - \hat{u})}{\hat{s}(\hat{u} - m_g^2)} \\
& \left. + \frac{m_g^2(\hat{s} - 4m_g^2)}{(\hat{t} - m_g^2)(\hat{u} - m_g^2)} \right]
\end{aligned}$$

where \hat{s} , \hat{t} , and \hat{u} are the Mandelstam variables of the elementary process.

We then parametrize these expressions, within the Monte-Carlo, in function of the following variables: ϕ (the azimuthal angle), θ (the angle with respect to the beam axis), $\Delta R = (\delta\phi^2 + \delta\eta^2)^{1/2}$ (which combines ϕ and θ variables) and p_T (the transverse momentum of partons). And finally, we study the evolution of these elementary processes at each of the various steps defined in the Monte Carlo, to generate the complete reaction: $pp \rightarrow \bar{g}g$ "realistically". This sequence is illustrated in the following diagram.



As a first stage, we have the hard scattering $q, g \rightarrow \tilde{g}_1 \tilde{g}_2$. We show in Fig. 19 a and b, the distributions of $\delta\theta(\tilde{g}_1, \tilde{g}_2)$ (i.e. the difference in θ between \tilde{g}_1 and \tilde{g}_2) and $\delta\phi(\tilde{g}_1, \tilde{g}_2)$ (i.e. the difference in ϕ between \tilde{g}_1 and \tilde{g}_2). We note the exact back to back feature of the $\delta\phi$ distribution (this is just conservation of transverse momentum).

The second step followed by the M.C to describe the reaction, is to produce by cascade shower, the gluon bremsstrahlung (QCD evolution). Figure 19 a and b also shows the distributions $\delta\theta'(\tilde{g}_1, \tilde{g}_2)$ and $\delta\phi'(\tilde{g}_1, \tilde{g}_2)$ where $\theta'_{i=1,2}$ and $\phi'_{i=1,2}$ are the new values of θ_i and ϕ_i obtained from the new 4-momentum $P'_{i=1,2}$ of the gluons 1 and 2 after they have emitted gluons by bremsstrahlung.

We note that the $\delta\phi'$ distribution is smeared; about 15% of the events have $\delta\phi \leq 120$ degrees so typical no back to back structure. It is interesting to note that this QCD evolution affects primarily the transverse plane (compare the change in $\delta\phi$ distribution to the one in $\delta\theta$ distribution).

The last step in the Monte Carlo decays each gluino into final partons which, in the example chosen here are $\tilde{g} \rightarrow \tilde{q}\bar{q}$ and $\bar{q} \rightarrow q\tilde{\gamma}$. The hadronization occurs also at this stage. We then study the corresponding distributions in $\theta, \phi, \Delta R$ and p_T of the final decay products, and we try to identify what will be the jet-topologies. In the special case we consider here: $q, g \rightarrow \tilde{g}\tilde{g} \rightarrow \tilde{q}_1\bar{\tilde{q}}_1 + \tilde{q}_2\bar{\tilde{q}}_2 \rightarrow \tilde{q}_1\bar{q}_1\tilde{\gamma} + \tilde{q}_2\bar{q}_2\tilde{\gamma}$, we expect each \bar{q} (coming from the gluino decay) to be almost collinear to the corresponding squark (as we have set $m_{\tilde{g}} \gtrsim m_{\tilde{q}}$, i.e the degenerate mass case).

In Fig. 20 a and b we note that this feature is clearly reproduced by the M.C. both in θ and ϕ for the decay product of each gluino. And also, as expected, the

p_T -distributions of \bar{q} 's are peaking at very low p_T value (with an average at about 4 GeV) as shown in Fig. 21, whereas most of the p_T is carried by the q 's which come from $\bar{q} \rightarrow q\tilde{\gamma}$ ($\langle p_T^q \rangle \gtrsim 19$ GeV). These are the expected features of the case we are considering here.

If we study the final jet-pattern, we have to consider the ΔR distributions which measure the difference in space-angle between each decay product and the p_T -distributions of each decay product. The choice of these variables strongly depends on the way jets are defined and accordingly on some properties of the detector. In the UA1 experiment, the minimum jet threshold is set to 12 GeV and two jets are considered as well separated if they have ΔR between their axis ≥ 1 . With these definitions, we are not able to distinguish 2 jets as produced by the final products $q\bar{q}$ coming from the decay of each gluino (because $p_T^{\bar{q}} < 12$ GeV, most of the time, i.e about 97%) although about 50% of the events have $\Delta R(q, \bar{q}) > 1$ (Fig. 22). Therefore, we consider that the axis of the jet corresponding to each g is the axis of the quark final decay product, and we look to $\Delta R(q_1, q_2)$ and $p_T^{q_1, q_2}$ to define the jet-pattern finally obtained.

About 72% of the events pass the requirement on $p_T^{q_1} > 12$ GeV. In addition, 42% of these events have $p_T^{q_1} > 12$ GeV and $p_T^{q_2} < 12$ GeV, therefore they will be considered as “monojets” according to the UA1 definitions. Within this framework, a bijet event will be defined by the set of following conditions: $p_T^{q_1} > 12$ GeV and $p_T^{q_2} > 12$ GeV and $\Delta R(q_1, q_2) > 1$. Therefore we are left with: $0.72 \times 0.58 \times 0.96 \sim 40\%$ of “bijet” events (which in fact have ≥ 2 jets). The monojet events are defined in the two following ways; first, if there is only one parton with $p_T^q > 12$ GeV and if

$\Delta R(q_1, q_2) < 1$, this leads to $0.72 \times 0.04 \sim 3\%$ of the events are monojets. Secondly, if $p_T^{q_1} > 12$ GeV and $p_T^{q_2} < 12$ GeV, the corresponding events are also monojets; therefore, we are left with $0.72 \times 0.42 \sim 30\%$ of such monojets. In total, we get an amount of 33% of the events produced by the process $pp \rightarrow \tilde{g}\tilde{g}$ (where $\tilde{g} \rightarrow \bar{q}q$ and $\bar{q} \rightarrow q\bar{\gamma}$) which are monojets.

By comparing with the results listed in the Table 4 for the case of filter 1 (i.e. no filter) and $m_{\tilde{g}} \simeq m_{\tilde{q}} = 40$ GeV we see that roughly we find the same results.

3.3-4 Limits On Gluino and Squark Masses From This Study On UA1 Data

As a final result of the "uniform approach" that we have used to analyze the missing energy data recorded by the UA1 experiment from 1983 to 1986, we may conclude that there is NO EVIDENCE FOR A SUSY-SIGNAL.

From this result one may try to define limits on the smasses. These limits are defined by comparing the expected results from the supersymmetric scenarios we have studied with the results obtained by the UA1 experiment^[18]. We consider the sample of data corresponding to the 4 sigma selection. This sample contains 56 events of which 53 are monojets and 3 are bijets no back to back. The corresponding total contribution of the standard model is 52.2 ± 6.9 (stat.) ± 3.6 (syst.). This means that the difference between these two numbers gives: 3.8 ± 10.5 events.

If we only consider monojets selected with the 4σ filter we get the following limits. If $m_{\tilde{g}} < m_{\tilde{q}}$, the limits are: $m_{\tilde{g}} > 30$ GeV and $m_{\tilde{q}} > 55$ GeV (with 95% C.L.) or $m_{\tilde{g}} > 26$ GeV and $m_{\tilde{q}} > 50$ GeV (with 99.5% C.L.). If $m_{\tilde{g}} \geq m_{\tilde{q}}$ (we suppose $m_{\tilde{q}} = 0.9 \times m_{\tilde{g}}$) then the limits are: $\tilde{m} > 53$ GeV (95% C.L.) which implies $m_{\tilde{g}} > 55.5$ GeV and $m_{\tilde{q}} > 51.5$ GeV or $\tilde{m} > 50$ GeV (99.5% C.L.) which implies $m_{\tilde{g}} > 54$ GeV

and $m_{\tilde{q}} > 50$ GeV.

Now, if we consider not only the monojets but also the bijets non back to back, these limits may be pushed a little bit further and we get for $m_{\tilde{g}} < m_{\tilde{q}}$, $m_{\tilde{g}} > 35$ GeV and $m_{\tilde{q}} > 60$ GeV (95% C.L.) or $m_{\tilde{g}} > 32$ GeV and $m_{\tilde{q}} > 57$ GeV (99.5% C.L.). If $m_{\tilde{g}} \leq m_{\tilde{q}}$, we get $\tilde{m} > 57$ GeV (95% C.L.) which implies $m_{\tilde{g}} > 60$ GeV and $m_{\tilde{q}} > 54$ GeV (95% C.L.) or $\tilde{m} > 55$ GeV (99.5% C.L.) which implies $m_{\tilde{g}} > 59$ GeV and $m_{\tilde{q}} > 53$ GeV (99.5% C.L.).

Still a problem has to be solved; it concerns the bounds for the low masses i.e. $\tilde{m} \leq 20$ GeV. We have studied various scenarios namely: $(m_{\tilde{g}}; m_{\tilde{q}}) = (10;30)$, $(10;50)$, $(10;100)$, $(20;30)$, $(21;19)$. The two first scenarios cannot be excluded so far, because although they give quite high rates, most of them do not pass the UA1 trigger requirements on E_T^{jet} and E_T^{miss} and also they would need the generation of quite a high statistic of events to be definitely excluded. The same thing happens for the case $(20;30)$. The case $(10;100)$ gives a very high contribution from gluino pair production which is totally cancelled by the first level trigger. The other elementary processes gluino squark and squark pair productions give a too small cross-section to be significant with the total integrated luminosity recorded by UA1. Therefore so far, this case cannot be excluded for lack of statistics.

Finally the case $(21;19)$, is definitively excluded, as a tremendous excess of monojet events should have been seen (3100 ± 950 expected monojets with 4 σ validation of E_T^{miss} !)

For the case $(m_{\tilde{g}} < m_{\tilde{q}})$, the “low mass window” (i.e. $\tilde{m} < 20$ GeV) still remains opened.

The results we have presented here are very model-dependent. In particular, they depend strongly on the belief that the photino is the LSP. We also see that even within this assumption, the results we obtained are very much dependent on which of the gluino or squark is the heavier particle.

This search for sparticles done with the UA1 data shows how difficult it will be to discover these new particles even if they are what we suppose them to be. We have suffered from the lack of statistics and some apparatus deficiencies such as the bad calorimeter granularity. We see in the next section how ACOL may improve the situation.

3.4 ACOL and Upgraded UA Detectors: Prospects for the Sp \bar{p} S

The upgrading of the CERN $\bar{p}p$ “complex” will consist in an improvement of the $\bar{p}p$ collider with ACOL and an improvement of the UA1 and UA2 detectors. ACOL^[20] is expected to provide an increase in luminosity of a factor of about 10 with respect to the previous $\bar{p}p$ run at CERN, at $\sqrt{s} = 630$ GeV. The major upgrade of UA1^[21] consists in rebuilding the central calorimetry to replace the present central electromagnetic calorimeters (the gondolas). In order to get a better granularity (G’s have no ϕ -granularity and a rather poor granularity in η), the new calorimeter will be made of uranium plates and TMP^[21]. The experiment UA2 has aimed at a full 4π coverage of its present granular calorimetry, plus an improvement of its central tracking and of the e^- recognition^[22]. However there will still be no magnetic field, no μ -detector, and the central tracking is rather poor.

We want to estimate the gain in rate and quality of events which may be expected with about $\gtrsim 10$ times more luminosity and a 4π fine-grained calorimetry.

we will compare to the results obtained by UA1 working with the first version of the CERN $\bar{p}p$ collider (i.e. $\sqrt{s} = 630$ GeV and a total of integrated luminosity of 715 nb^{-1}). However, we cannot just scale the results obtained by UA1 by a factor ≈ 10 higher to get the limits with the new " $\bar{p}p$ configuration" at CERN; we must do a more careful work, trying to estimate also the gain due to the new calorimetry. This will be essential since we are studying hadronic processes, therefore strongly dependent on a good recognition of jets. Moreover, we will have to apply new filters and new jet algorithmes according to this new structure of the calorimetry; as we will see the main gain will be a simplification of the overall procedure.

To achieve this work, we have used a simulation which considers a 4π fine-grained calorimeter segmented in η and ϕ according to elementary cells of $\delta\eta \times \delta\phi = 0.1 \times 0.086$, which represents a total of 120×72 cells and a full coverage in η , defined by $|\eta| \leq 6$. A resolution in e.m. energy of:

$$\Delta E/E = 0.15 \pm 0.01$$

and in hadronic energy of:

$$\Delta E/E = 0.5 \pm 0.05$$

is defined in this simulation.

Because of the fine-grained topology of this device, we use a simple cluster finder which works as follows: it looks for the highest- E_T cell (requiring a minimum E_T of 1.5 GeV in the given tower) and then searches the nearest neighbours, picking up anything above 500 MeV. It does some searching for valleys to determine if two or more clusters are touching. Clusters whose centers have $\Delta R \leq 1$, are merged and

called jets. In addition, a minimum E_T of 10 GeV is asked to define a jet.

We have varied the parameters which are used to define the jets [namely ΔR , $E_T^{\text{jet}(\min)}$], and also the cell size, that we have decreased by a factor 4]. We note that the main change is obtained if we increase the value of $E_T^{\text{jet}(\min)}$: this drastically increases the average number of monojets. Therefore we are quite confident of the stability of the results obtained with the set of parameters stated before (i.e. $\Delta R \leq 1$; $E_T^{\text{jet}(\min)} \geq 10$ GeV and the granularity as previously defined).

We have studied in this upgraded version at $\sqrt{s} = 630$ GeV, a whole set of scenarios. If $m_{\tilde{g}} < m_{\tilde{q}}$ (i.e. $\tilde{g} \rightarrow q\bar{q}\tilde{\gamma}$ and $\tilde{q} \rightarrow q\tilde{g}$), we consider mainly the following couples of gluino and squark masses: $(m_{\tilde{g}}; m_{\tilde{q}})$ in GeV = (35; 80), (50; 100), and (70; 161). If $m_{\tilde{g}} \gtrsim m_{\tilde{q}}$ (i.e. $\tilde{g} \rightarrow \tilde{q}\bar{q}$ and $\tilde{q} \rightarrow q\tilde{\gamma}$), we study the two following cases: $(m_{\tilde{g}}, m_{\tilde{q}})$ in GeV = (84; 80) and (105; 95). We have computed for each case, using the estimation of Isajet integrated in a range in P_T going from 20 to 200 GeV, the differential cross-section $d\sigma/dp_T$ summed over the three elementary processes $pp \rightarrow \tilde{g}\tilde{g}$, $\tilde{g}\tilde{q}$, and $\tilde{q}\tilde{q}$. We list in Table 5 these cross-sections, as well as the expected rates, comparing the case of UA1 (715 nb⁻¹) with ACOL (where we have assumed 10 pb⁻¹ of integrated luminosity).

This Table summarizes the gain due to the increased luminosity provided by ACOL (about a factor of 15 in total, compared to what UA1 has finally recorded).

Table 5: Comparison between ACOL (10^4 nb^{-1}) and UA1 ($L=715 \text{ nb}^{-1}$)

Process ($m_{\tilde{g}} ; m_{\tilde{q}}$) (GeV/c ²)	σ_{eff} (mb) at $\sqrt{s} = 630 \text{ GeV}$ (and $P_T: 20-200 \text{ GeV/c}$)	Expected rate at UA1 ($L = 715 \text{ nb}^{-1}$)	Expected rate at ACOL ($L = 10^4 \text{ nb}^{-1}$)
$m_{\tilde{g}} \ll m_{\tilde{q}}^*$ (10 ; 100) (50 ; 250)	0.92×10^{-6} (6.4×10^{-8}) 0.31×10^{-10} (2.1×10^{-12})	690 -	9200 -
$m_{\tilde{g}} < m_{\tilde{q}}$ (35 ; 80) (50 ; 100) (70 ; 161) (95 ; 218)	3.6×10^{-6} 4.4×10^{-7} 4.6×10^{-8} 4.2×10^{-9}	2600 310 33 3	36000 4400 460 42
$m_{\tilde{g}} \geq m_{\tilde{q}}$ (84 ; 80) (105 ; 95) (157.5;142.5)	4.7×10^{-6} 9.8×10^{-9} 1.7×10^{-10}	30 7 -	470 100 2

*The only process considered in the case where $m_{\tilde{g}} \ll m_{\tilde{q}}$ is $pp \rightarrow \tilde{g}\tilde{q}$ with a P_T range of 5 - 100 GeV/c. In this case the numbers quoted in parenthesis include the branching ratios of the decay $q \rightarrow \tilde{q}\gamma$. For the other cross-sections we have quoted the total cross-section i.e. the sum of the three elementary contributions $pp \rightarrow \tilde{g}\tilde{g}$, $\tilde{g}\tilde{q}$ and $\tilde{q}\tilde{q}$ with a range of P_T from 20 to 200 GeV/c.

Now, to evaluate the limits on smasses accessible at ACOL, we must develop a new way of analyzing and filtering the data in such a new calorimeter. The approach developed in UA1 was strongly influenced by the special features of this detector, we must now change it. We adopt a strategy to recognize the jet pattern of an event which is defined by the granularity in (η, ϕ) . This approach will be applied also to the case of detectors such as CDF (which is also a 4π fine-grained calorimetry, see next section) and, a fortiori, the detectors that we will consider for super pp colliders. (see last section). It is based mainly on the definition of two parameters which rely on a better estimation of the spatial localization in (η, ϕ) of the clusters (thanks to the better granularity of the detection in this plane). These two parameters^[10], called x_E and x_{out} measure the projections of the total missing transverse energy vector onto the sphericity axis of the event or the axis of the highest- E_T^{jet} (both give pretty much the same result) and onto the axis perpendicular to it:

$$x_E = \frac{E_T^{miss}}{E_T^{tot}} \cdot \vec{e}_1, \quad x_{out} = \frac{E_T^{miss}}{E_T^{tot}} \cdot \vec{e}_2$$

\vec{e}_1 and \vec{e}_2 being the unit vectors of the main axis and the axis perpendicular to it, respectively.

Thanks to these new parameters, we show how we may overcome the background and extract possibly SUSY signals in the mass range defined by Table 5.

As shown by the UA1 experiment^[18], the backgrounds to the new processes we will search for, are mainly due to the standard QCD jets and to the processes: $W \rightarrow \tau \nu_\tau$ (where the τ decays into the hadronic decay mode) and $Z^0 \rightarrow \nu \bar{\nu}$. We have made a careful study of these various backgrounds, and in particular of the

main characteristics of the events they produce. We compare them with those SUSY processes that we consider here, and give the corresponding results in Table 6.

Process ($m_{\tilde{g}} ; m_{\tilde{q}}$) (GeV/c ²)	$\langle E_T^{\text{tot}} \rangle$ (GeV)	$\langle E_T^{\text{miss}} \rangle$ (GeV)	$\langle x_E \rangle$	$\langle x_{\text{out}} \rangle$	$\langle \# \text{ jets} \rangle$				$\langle E_T^{\text{max}} \rangle$ (GeV)	$\langle E_T^{\text{min}} \rangle$ (GeV)
					% 1 jet	% 2 jets	% 3 jets	% ≥ 4 jets		
(35 ; 80)	119	15.7	0.10	0.074	2.7				31	17
(50 ; 100)	136	23	0.13	0.096	46	39	12	3	37.5	17.6
(70 ; 161)	159	29	0.14	0.104	30	42	22	6	47	19
					17.6	42.3	31	9		
(84 ; 80)	146	43	0.25	0.13	2.4				54	27
(105 ; 95)	162	51	0.26	0.13	56	34.5	8	1.5	62	26
					46	35	18	1		
(10 ; 100)					2				44	25
$\tilde{q} \rightarrow q\tilde{t}$	117	39	0.32	0.093	71	24	4	1	45	21.5
$\tilde{q} \rightarrow q\tilde{g}$	144	14.6	0.10	0.04	38	40	16	6		
<u>QCD</u>					1.8				34	23
$P_T \geq 20$ GeV/c	102	3.1	0.023	0.12	73	23.5	3	0.5	58	31
$P_T \geq 50$ GeV/c	172	4.2	0.02	0.12	46.5	37.8	12	3.7		
$W \rightarrow \tau\nu_\tau$					1.8				34	23
$P_T^W \geq 20$ GeV/c	98	28	0.25	0.12	90.6	8.8	0.6	0.6	58	31
$P_T^W \geq 50$ GeV/c	140	46	0.29	0.12	68.5	2.5	4.8	6.5		
$Z^0 \rightarrow \nu\bar{\nu}$					1.2				28	25
$P_T^{Z^0} \geq 20$ GeV/c	79	29	0.36	0.07	97.3	2.7	-	-	58	42
$P_T^{Z^0} \geq 50$ GeV/c	117	58	0.49	0.76	90.4	7.6	1.3	2		

Table 6 : Comparison of the main characteristics of the SUSY-Signal and the main sources of background.

Now we will evaluate the limits on the masses of gluino and squark which could be detectable at ACOL with a total integrated luminosity of 10 pb^{-1} . We define these limits of detectability in function of the signal to the background ratio (S/B), the statistical significance (S/\sqrt{B}) and the total number of events which remain after the filtering procedure is applied. We will propose a way to overcome the huge background in order to get a statistically significant signal. However the final extraction of the signal will imply a refined and very sophisticated analysis which will not be done here, because it depends very much on the details of the apparatus and the detailed properties of the signal.

Let us set-up a trigger strategy to obtain reasonable limits on the detectability of the various cases we are looking for. For each background we consider the various contributions according to the value of P_T^{\min} (minimum value of the transverse momentum of the primary partons). In the case of the QCD background, we take as low P_T contribution the one defined by a P_T^{\min} value of 20 GeV.

It is interesting to see the evolution of this background in the E_T^{miss} distribution when varying P_T^{\min} . We summarize in the Table 7 some characteristics of this background and their evolution when increasing P_T^{\min} .

Table 7: Evolution of the average value of some of the main characteristics of the QCD background in function of P_T^{\min} at ACOL

Parameter type	$P_T^{\min} > 20 \text{ GeV}$	$P_T^{\min} > 30 \text{ GeV}$	$P_T^{\min} > 40 \text{ GeV}$	$P_T^{\min} > 50 \text{ GeV}$
$\sigma(\text{in mb})$	0.48×10^{-2}	0.6×10^{-3}	0.11×10^{-3}	0.26×10^{-4}
$\langle E_T^{\text{miss}} \rangle \text{ (GeV)}$	3.1	3.5	3.9	4.3
$\langle n^{\text{jet}} \rangle$	2.3	2.5	2.7	2.8
$\langle E_T^{\text{max}} \rangle \text{ (GeV)}$	25	35.5	46	56
$\langle E_T^{\text{min}} \rangle \text{ (GeV)}$	18.3	23.7	28.6	32.8

Figure (23) shows the evolution of the E_T^{miss} spectrum when P_T^{min} varies from 20 to 50 GeV.

These results show how disturbing is the high P_T tail of the QCD process when looking for these Susy-signals. The lower P_T QCD contribution will indeed also perturb our search in particular when looking for the production of sparticles with relatively low masses. We therefore have to accurately evaluate this background.

To study the low P_T contribution, high statistics are needed because there are very few such QCD events which pass our cuts but their rate is so tremendously high compared to the signal. We have generated 10^5 events according to the process $pp \rightarrow q, g$ (all light constituents included) at $\sqrt{s} = 630$ GeV and requiring in addition that $P_t^{(q,g)} > 20$ GeV. By simply applying a cut of 20 GeV on E_T^{miss} we notice (see Table 8b) that we decrease this background by almost 5 orders of magnitude. Such a strong effect is not obtained on the high P_T tail. By generating a few times 10^4 events according to the process $pp \rightarrow q, g$ with $P_t^{(q,g)} > 50$ GeV, and, applying a cut on E_T^{miss} of 20 GeV, we are still left with 0.4×10^{-7} mb which means only 3 orders of magnitude less. This is not enough to extract higher mass Susy signals which are mainly hidden by this background. Therefore more subtle cuts must be found.

Instead of cutting directly on E_T^{miss} , we use x_E and x_{out} variables and find an optimized result with a combined cut on x_E and x_{out} (see Table 8b). By demanding $x_E > 0.16$ and $x_{\text{out}} > 0.06$, we succeed to decrease by 4 orders of magnitude the high P_T tail contribution of the QCD background.

Table 8: Effects of the "trigger strategy" defined at ACOL to extract Susy signals on a) the considered Susy processes, b) the standard backgrounds.

Process ($m_{\tilde{g}} ; m_{\tilde{q}}$) in GeV/c ²	σ (mb)	cuts on E_T^{miss}		$E_T^{\text{max}} > 40$ GeV	combined cut ($E_T^{\text{max}}, x_E, x_{\text{out}}$)
		$E_T^{\text{miss}} > 20$ GeV	(x_E, x_{out})		
(35 ; 80)	3.3×10^{-6}	9.4×10^{-7}	4.4×10^{-7}	4.0×10^{-7}	-
(50 ; 100)	0.4×10^{-6}	2.0×10^{-7}	0.6×10^{-7}	1.4×10^{-7}	0.19×10^{-7}
(84 ; 80)	0.47×10^{-7}	0.36×10^{-7}	0.18×10^{-7}	0.33×10^{-7}	0.15×10^{-7}
(70 ; 161)	0.43×10^{-7}	0.29×10^{-7}	0.10×10^{-7}	0.27×10^{-7}	0.07×10^{-7}
(105; 95)	0.63×10^{-8}	0.05×10^{-7}	0.028×10^{-7}	0.05×10^{-7}	-
(10; 100) ^{b)}	0.65×10^{-7}	0.56×10^{-7}	0.35×10^{-7}	0.4×10^{-7}	0.21×10^{-7}

Table 8a - Effects of cuts on the SUSY signal at ACOL^{a)}

^{a)} The cut quoted as (x_E, x_{out}) corresponds to the requirement: $x_E > 0.16$, $x_{\text{out}} > 0.06$. The combined cut refers to the same conditions on x_E, x_{out} plus an additional cut on E_T^{max} required to be larger than 40 GeV.

^{b)} The last row includes only the process $\tilde{g}\bar{q}$ where the squark decays into $q\tilde{\gamma}$ (BR $\simeq 7\%$ included in the quoted cross-section).

Table 8b: Effects on the "trigger strategy" defined at ACOL to extract Susy signals on b) the standard backgrounds.

Background and P_T range of the process in GeV/c	σ (mb)	cuts on E_T^{miss}		$E_T^{\text{max}} > 40 \text{ GeV}$	combined cut $(E_T^{\text{max}}, X_E, X_{\text{out}})$
		$E_T^{\text{miss}} > 20 \text{ GeV}$	(X_E, X_{out})		
QCD					
$P_T^{\text{jet}} \geq 20$	0.47×10^{-2}	1.5×10^{-7}	1.7×10^{-7}	60.0×10^{-6}	—
$P_T^{\text{jet}} \geq 30$	0.57×10^{-3}	1.2×10^{-7}	1.2×10^{-7}	0.95×10^{-4}	—
$P_T^{\text{jet}} \geq 50$	0.26×10^{-4}	0.4×10^{-7}	0.026×10^{-7}	24.0×10^{-6}	0.026×10^{-7}
$W \rightarrow \tau \nu_\tau$					
$P_T^W \geq 10$	0.51×10^{-7}	0.27×10^{-7}	0.15×10^{-7}	0.059×10^{-7}	0.033×10^{-7}
$P_T^W \geq 20$	0.15×10^{-7}	0.087×10^{-7}	0.065×10^{-7}	0.03×10^{-7}	—
$Z^0 \rightarrow \nu \bar{\nu}$					
$P_T^Z \geq 10$	0.43×10^{-7}	0.12×10^{-7}	0.13×10^{-7}	0.016×10^{-7}	0.0084×10^{-7}
$P_T^Z \geq 20$	0.13×10^{-7}	0.076×10^{-7}	0.054×10^{-7}	0.016×10^{-7}	—
TOTAL	0.47×10^{-2}	2.45×10^{-7}	2.1×10^{-7}	84.0×10^{-6}	0.067×10^{-7}

TABLE 8b - Effects of cuts on the background at the ACOL *

* The cut quoted as (X_E, X_{out}) correspond to the requirement :

$X_E \geq 0.16$ and $X_{\text{out}} \geq 0.06$. The combined cut refers to the condition

$E_T^{\text{max}} > 40 \text{ GeV}$ and $X_E \geq 0.16$ and $X_{\text{out}} \geq 0.06$.

Now we have seen in Section 2 and Table 6. that the decay of W into $\tau\nu_\tau$ or Z^0 into $\nu\bar{\nu}$ are characterized by a large amount of E_T^{miss} . Therefore, one has to define another cut to get rid of them. By applying a cut on the E_t of the stiffest jet in the event (E_t^{max}) of 40 GeV, we succeed (see Table 8b) to sufficiently overcome these two backgrounds which essentially affect the search of high mass sparticles.

We may now define a trigger strategy which could be used to extract the signals. This trigger strategy will be different for different smass range.

At ACOL the "low mass range" includes the signals defined by $(m_{\tilde{g}}; m_{\tilde{q}}) = (35; 80)$ and $(50; 100)$. For these signals the main background is due to QCD jets with $P_T^{\text{min}} = 20$ GeV; The processes $W \rightarrow \tau\nu_\tau$ or $Z^0 \rightarrow \nu\bar{\nu}$ (with $P_t^{(W,Z)} \geq 10$ GeV) are at least one order of magnitude lower. Therefore, a simple cut on E_T^{miss} is sufficient enough to get $S/B \geq 1$ and enough events remain to perform a more sophisticated analysis.

The high mass range includes the cases where $(m_{\tilde{g}}; m_{\tilde{q}}) = (84; 80), (70; 161), (105; 95)$. They are more sensitive to the high P_T contribution of the QCD background as well as the W and Z^0 backgrounds. This is due to the fact that the corresponding cross-sections are at least one order of magnitude lower than the low smass signal. Therefore, the E_T^{miss} cut is not good enough to reduce the standard background. By combining the cuts on the parameters x_E , x_{out} and E_t^{max} , a good rejection factor is obtained. The effects of these cuts on both the signals and the backgrounds are listed in details in Table 8 a and b. Let us summarize them.

The total background contribution after a cut on E_T^{miss} of 20 GeV is applied, is : $B_{\text{tot}}^{\text{low}} = 2.4 \times 10^{-7}$ mb; after a combined cut on x_E , x_{out} and E_t^{max} is applied.

this total background contribution reduces to $B_{\text{tot}}^{\text{high}} = 0.06 \times 10^{-6}$ mb. Therefore we obtain the following values for S/B , S/\sqrt{B} and the number of remaining Susy events

Table 9: Main results from the trigger strategy defined for ACOL

Process ($m_{\tilde{g}}$; $m_{\tilde{q}}$) (in GeV)	S/B	S/\sqrt{B} (# of σ 's)	Number of remaining events for $L = 10 \text{ pb}^{-1}$
(35 ; 80)	3.8	190	9400
(50 ; 100)	0.8	40	2000
(64 ; 80)	2.5	19	150
(70 ; 151)	1.1	9	70
(10;100) ^{a)}	3.5	250	210

* In this case only the process $\tilde{g}\tilde{q}$ is considered.

This means that the detection of these signals (including also the case (10;100)) should be achievable with ACOL and 10 pb^{-1} of integrated luminosity. But the case (105;95) seems, within these conditions, totally hopeless.

This allows to push further the limits obtained presently at CERN; they are indicated in Fig (28).

A very important result is the one obtained by considering the case of a very light gluino ($m_{\tilde{g}}$; $m_{\tilde{q}}$) = (10; 100). We have demonstrated that, in the case of ACOL with 10 pb^{-1} and a fine-grained calorimeter, there is a very good chance to identify this possibility by considering the process $p\bar{p} \rightarrow \tilde{q}\tilde{g}$ where $\tilde{q} \rightarrow q\tilde{\gamma}$. There will be sufficient events after the combined cuts on x_E , x_{out} and E_t^{max} (about 210 events). Moreover, these events will present a striking signature as they will be (see the analysis presented above on current UA1 data) dominated by monojets with E_t of the jet larger than 40 GeV and bijets non-back-to-back.

The theoretical importance of such a scenario makes it worthwhile to have a good detector running at ACOL with sufficient luminosity to make the test. This low

mass window is very difficult to explore with higher center-of-mass energy machines such as the Tevatron. It therefore provides a unique chance for ACOL to make a fundamental discovery.

4. Supersymmetry with a 2 TeV c.m. Energy $\bar{p}p$ Collider,

Main prospects

The Tevatron has started to successfully run at 1.8 TeV c.m. energy and about $10^{29} \text{ cm}^{-2} \text{ s}^{-1}$ peaked luminosity, beginning of 1987. with the CDF starting to take data. A total of 35 nb^{-1} have been recorded on tapes . It shows nice features of its good functioning: Detection of W's, Z's and high P_t jets. The next run will take place during most of the year 1988 and the CDF detector is expected to record of the order of 1 pb^{-1} data on tape. Around 1992, an upgrade in luminosity is foreseen. A nominal value of $5 \times 10^{31} \text{ cm}^{-2} \text{ s}^{-1}$ should be feasible.

Therefore the Tevatron stands in a key position between the relatively low mass range accessible at the Cern $\bar{p}p$ collider ($O(m_W)$) and the higher mass range accessible at super pp colliders ($O(1 \text{ TeV})$). The main question is to see how this machine will link these two regions and also overlap sufficiently well with each of them. The first issue is the competition starting right now between ACOL and the Tevatron.

4.1 Cross-sections and rates at Tevatron compared to ACOL

Both machines will run in 1988: ACOL at 630 GeV c.m. energy and a foreseen integrated luminosity of 10 pb^{-1} ; and the Tevatron at about 3 times more c.m energy and 10 times less integrated luminosity.

In the next Table, we give a comparison of the cross-sections in mbarns between ACOL and the Tevatron for the processes we have studied in both machines.

For smasses of the order of 40 GeV, the ratio of the total cross-section at ACOL versus the total cross-section at the Tevatron: $\sigma(\text{ACOL})/\sigma(\text{Tevatron})$ is of the order of a few percent (3%). For smasses around of the order of 100 GeV, $\sigma(\text{ACOL})/\sigma(\text{Tevatron})$ is of the order of 0.5%. For the light gluino case the discrepancy between ACOL and Tevatron is even larger; for the case (50:250), $\sigma(\text{ACOL})/\sigma(\text{Tevatron}) = 2.6 \times 10^{-4}$. Therefore increasing the c.m. energy by a factor of 3 gives a very substantial gain in cross section. It is of the order of $(E_{\text{c.m.}}^{\text{low}}/E_{\text{c.m.}}^{\text{high}})^4$ in average. A factor 10 in luminosity cannot recover such a discrepancy.

Table 10: Comparison of Cross-Sections (in mb) between ACOL and Tevatron

$\sigma(\text{ACOL})$	$\sigma(\text{Tevatron})$	$(m_{\tilde{g}} ; m_{\tilde{a}}) \text{ GeV}$	$\frac{\sigma(\text{ACOL})}{\sigma(\text{Tevatron})}$
0.45×10^{-4}	0.7×10^{-3}	(25 ; 50)	0.064
3.6×10^{-6}	1.2×10^{-4}	(35 ; 80)	0.03
0.44×10^{-6}	0.27×10^{-4}	(50 ; 100)	0.014
4.6×10^{-6}	0.5×10^{-5}	(70 ; 161)	0.01
4.2×10^{-9}	8.8×10^{-7}	(95 ; 218)	0.005
—	7.5×10^{-6}	(140 ; 322)	—
0.6×10^{-5}	0.23×10^{-3}	(42 ; 40)	0.026
0.5×10^{-7}	0.5×10^{-5}	(84 ; 80)	0.01
0.98×10^{-8}	1.5×10^{-6}	(105 ; 95)	0.0065
0.17×10^{-9}	1.5×10^{-7}	(157.5 ; 142.5)	0.001
—	1.8×10^{-8}	(210 ; 190)	—
0.27×10^{-6}	0.1×10^{-4}	(10 ; 100)	0.027 (*)
0.26×10^{-10}	0.1×10^{-6}	(50 ; 250)	$2.6 \times 10^{-4} (*)$

In a comparison of the limits in detectability of such signals for both machines, capability of the detector to measure and identify these signals is very important. Moreover the signal to background ratio also is an important factor. From the results quoted in Table (1) in Section 2, we may derive that S/B is about the same in both machines. For instance, it is of the order of 5% when considering the background due

to QCD jets and applying a cut on the Pt of these jets equivalent to the smass we are looking for.

In Subsection 4.4, we compare the limits of detectability of Susy processes at the Tevatron with the ones accessible at ACOL and the super pp colliders. Before doing so, let's describe the main features of the CDF detector and of some types of Susy events as simulated in this detector.

4.2 The CDF Detector

The Collider Detector at Fermilab is a fine-grained 4π calorimetry with electromagnetic calorimetry followed by hadronic calorimetry behind it. Typical energy resolutions are $(0.15 \text{ or } 0.25)/\sqrt{E}$ for the e.m. calorimetry and, $(0.65 \text{ to } 1.0)/\sqrt{E}$ for the hadronic calorimetry. The calorimetry projective tower granularity is typically $\Delta\eta = 0.1$, $\Delta\phi = 5^\circ$ forward, 15° central. The central detector contains a 15 kGauss solenoidal magnetic field filled with tracking chambers for momentum analysis. In addition, there is muon detection over a limited solid angle. See Reference [23] for more details.

During CDF's first extended data-taking run (March-May 1987), approximately 35 nb^{-1} of data was accumulated on tape. Because of the very limited statistics from this run, and because the data is still in the process of being analyzed, we will discuss here predictions from a simulation of the detector performance.

For this study a detailed simulation of the detector, including cracks, dead areas, finite calorimetry thickness and calorimetry non-linearity was used^[24]. CDF has a very sophisticated level 1/level 2 trigger, capable of triggering on clusters of energy, missing E_T , leptons, and various combinations of the above. During normal

data-taking, the threshold for the missing E_T trigger is expected to be approximately 20 GeV^[23]. For the following analysis, thresholds of approximately 50 GeV E_T missing was chosen for offline filtering to insure the removal of trigger threshold effects.

4.3 Susy Events in the CDF Detector

A set of Susy scenarios have been carefully simulated in the CDF detector. For the case $m_{\tilde{g}} < m_{\tilde{q}}$, the following series of values for $(m_{\tilde{g}} ; m_{\tilde{q}})$ have been considered: (25;50), (50;100). For the case $m_{\tilde{g}} \ll m_{\tilde{q}}$, the example with (50;250) has been study in details. Finally if $m_{\tilde{g}} \geq m_{\tilde{q}}$, we have looked at the following set of values: (42;40) and (84;80). These examples have been fully simulated, analyzed and scanned using the different off-line facilities of the CDF experiment.

Some displays of these events are shown in Figures 24 and 25. Figure 24 show various displays of an event generated according to the process $pp \rightarrow \tilde{g}\tilde{q}$ where $m_{\tilde{g}} = 100$ GeV and $m_{\tilde{q}} = 200$ GeV. The gluino decays into $q\bar{q}\tilde{\gamma}$ and the squark decays into $q\tilde{g}$. This event is then fully simulated in the CDF detector. Figure 24a shows the LEGO plot view as provided by the fine grained calorimetry of the detector (the e.m contribution is clearly distinguished from the hadronic contibution, in each tower). There are four clusters in this event (as the fifth one has an E_T smaller than 10 GeV. The trigger cluster has an $E_T = 79.4$ GeV and the three others have $E_T = 25.4, 23.2$ and 20.4 GeV. A total missing transverse energy of 37.8 GeV is measured in this event which is a nice multijet. Figure 24b shows the same event but as viewed by the central tracking (CTC chambers^[23]) again a multijet topology is seen in this detector with a precise reproduction of the charged part of the corresponding clusters. In Figure 25 is shown an event generated following the process $pp \rightarrow \tilde{g}\tilde{q}$ in the degenerate

mass case with $m_{\tilde{g}} = 105$ GeV and $m_{\tilde{q}} = 100$ GeV; the gluino decays into $\tilde{q}\tilde{q}$ and the squark decays into $q\tilde{\gamma}$. After full simulation in the CDF detector the display package reproduces in Figure 25 a, the LEGO plot view of the event and in Figure 25 b, the charged part of the events as seen in the central tracking. A bijet no b/b structure appears in this case, with two clusters with an E_T above 10 GeV (namely 70.5 and 18.7 GeV) and an E_T^{miss} of 74.8 GeV back to the resultant of these two clusters.

To analyze the data we study their jet structure. To define a jet in the CDF detector, we have used a simple clustering algorithm which makes use of the fined-grained calorimetry. It is similar to the one described for ACOL. A cut of 10 GeV is applied as minimum E_t value to define a jet. The aperture in ΔR used to define the jet is of 0.7. Using this algorithm, we studied the jet pattern provided by some Susy scenarios and compared them with those produced by the standard backgrounds. The results are summarized in Table 11 a and b. In CDF the "no back to back" activity is defined by the requirement that there is less than 5 GeV E_T in the ± 30 degrees ϕ region opposite to the considered cluster; an event is classified as a monojet if it has only one cluster with $E_T^{(\text{cluster})} \geq 10.0$ GeV and with $|\eta| < 2.0$ and no activity back in ϕ to this cluster. Likewise a bijet event is defined as an event with 2 clusters both with $E_T^{(\text{cluster})} > 10$ GeV and the ϕ 's of the clusters less than 150° apart.

The main remarks about the numbers quoted in Table 11 a and b are that if $m_{\tilde{g}} < m_{\tilde{q}}$, the multijet structure (i.e. $n_{\text{jet}} \geq 3$ jets) is favoured and the jet multiplicity increases when the smass increases. On the other hand, the case with $m_{\tilde{g}} > m_{\tilde{q}}$ favors relatively low jet multiplicity, namely monojets and bijets non back to back. At relatively low smasses (i.e. of the order of 40 GeV), monojets and bijets

are of about the same amount (of the order of 20% each). When m_{smass} increases say up to 80 GeV, the bijet signature becomes predominant (about 40%) while monojets and trijets are of the same order of magnitude (i.e. about 10%).

Table 11: Jet Pattern as given by Susy Signal (a) and Standard Background (b) in the CDF detector

Table 11a

Jet pattern of susy events in the CDF detector.

Process ($m_{\tilde{g}} ; m_{\tilde{q}}$)	Percentage of events with a given jet topology :						
	Monojet (all)	Monojet no b/b	Bijet b/b	Bijet no b/b	3 jets	4 jets	≥ 5 jets
$\tilde{g}\tilde{g}$ (25 ; 50)	18	4.5	19	27	30	4	—
$\tilde{g}\tilde{q}$ (25 ; 50)	30	6.5	18	20	12	1.2	—
$\tilde{g}\tilde{q}$ (42 ; 40)	41	22	16.5	26	0.5	—	—
$\tilde{g}\tilde{q}$ (50 ; 100)	9	4	10	20	38	18	3.5
$\tilde{g}\tilde{q}$ (50 ; 250)	3	1	18	27	36	12.3	3.6
$\tilde{g}\tilde{q}$ (84 ; 80)	22.5	12.5	21.3	41.7	12.3	—	—

Table 11 b) Jet pattern of the standard background in the CDF Detector

Process : (P_T cut in GeV)	Percentage of events with a given jet pattern						
	Monojets (all)	Monojets no b/b	Bijets b/b	Bijets no b/b	3 jets	4 jets	≥ 5 jets
$W \rightarrow \tau \nu_\tau$							
$P_T^W < 20$	46	23	0.5	1	0.1	—	—
$P_T^W > 20$	44	14.5	13.5	26	3	—	—
$P_T^W > 50$	26	9	22	26	13	3	< 0.5
$Z^0 \rightarrow \nu \bar{\nu}$							
$P_T^{Z^0} < 20$	—	—	—	—	—	—	—
$P_T^{Z^0} > 20$	67.7	29	1	5	—	—	—
$P_T^{Z^0} > 50$	63	25	4	23.3	5	1	—
QCD							
$P_T^{\text{jet}} > 20$	20	—	49.5	8.5	7.5	< 1	< 0.1
$P_T^{\text{jet}} > 50$	—	—	4.6	7	40	10.5	3.6
$P_T^{\text{jet}} > 80$	—	—	32.5	—	37.5	19	11
$P_T^{\text{jet}} > 120$	—	—	26	—	33	27	14

As expected, higher rates of multijets are obtained at the Tevatron energy compared to the case at $\sqrt{s} = 630$ GeV. This means, that from the point of view of the jet topology, QCD events will mimic Susy events as they produce mainly multijets. W 's and Z 's will still provide mainly monojets and bijets non back to back. It is also important to note the large number of QCD events which are bijets back to back. Missing E_T QCD events can be generated either through the intrinsic physics of the event (heavy quark decays with a physical ν) or due to detector performance. Some suppression of heavy quark decay backgrounds can be achieved through veto of events with an identified lepton. Large detectors always have cracks and problem regions, and CDF is no exception. Examples include the ϕ cracks every 15° in the central region, and the interface region between central and intermediate calorimetry. Fairly efficient fiducial cuts can be made, vetoing events where clusters fall in those regions. In the study below, such cuts were not made. Imposition of these geometric cuts will not change the results, since QCD background is not very large due to analysis cuts.

Characteristic E_T^{miss} and the $E_T^{\text{jet-trigger}}$ spectra given by each type of signal and background events are shown in Figure 26 a and b.

A way to overcome the huge background will therefore be to apply cuts on some of the main features we described just now. Direct cuts on E_T^{miss} or on the jet topologies will be studied as well as on projected values of E_T^{miss} . We will define various ways to analyze these events in the next subsection.

4.4 Limits of Detectability of Susy Events With CDF Detector at the Tevatron.

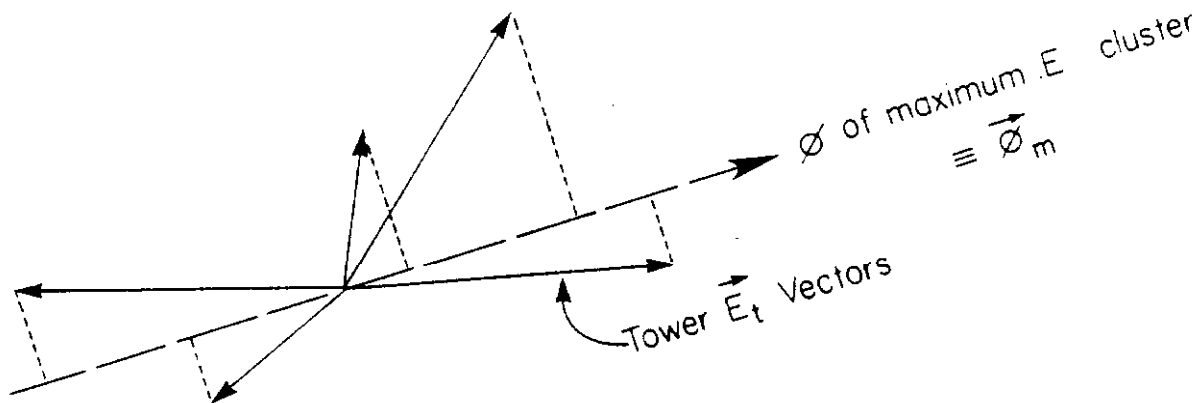
Main Prospects For the Next Run

Two sets of detectability limits of s-masses will be addressed in this paper for

what concerns the Tevatron. The first set of limits are estimated in the case of a total integrated luminosity of 1 pb^{-1} . The second set corresponds to the case of an upgraded machine and therefore 1000 times more luminosity. In this last case, the goal is to see how well Tevatron could "overlap" with the super pp colliders. This is discussed in Section 5. We discuss now various ways to obtain the limits for the low luminosity case.

Projected E_T Analysis

Recalling the x_E discussion earlier, we define an analogous variable, pE_T , parallel projected E_T along the ϕ of the maximum cluster axis. The prescription for determining pE_T is shown in the following schema:



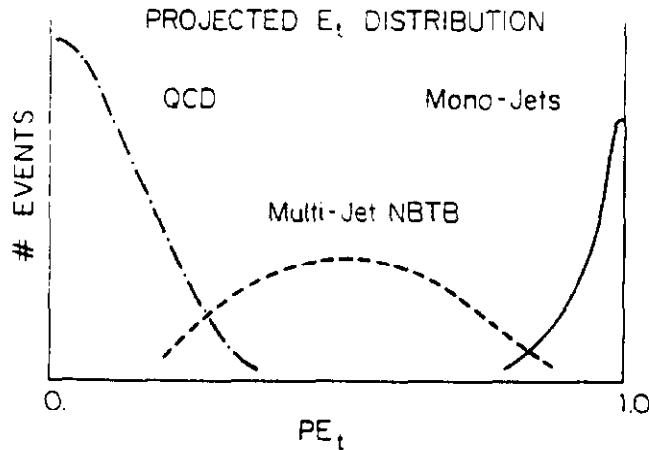
1. Maximum E_T cluster is found. $\vec{\phi}_m$ is the ϕ coordinate of this cluster.

2. All towers are looped over, projecting the E_T vector of the towers onto the ϕ of the cluster. The tower E_T vector has magnitude of the E_T deposited in the tower, and ϕ of the tower center. The vector and scalar sums are formed.
3. pE_T is the ratio of the vector sum to the scalar sum.

$$pE_T = \frac{\sum_i \vec{E}_{Ti} \cdot \vec{\phi}_m}{\sum_i |\vec{E}_{Ti}| |\vec{\phi}_m|}$$

with i summing over all towers.

pE_T sorts events according to their "mono-jetiness". 2-jet events with some missing E_T (small compared to the jet E_T) will populate the region of pE_T near 0. Very monojet-like events will populate the region of pE_T near 1.0. Intermediate topology events (i.e. 2-JET no b/b) will populate the intermediate region.



As an aside, we note that there are other choices of the axis to project E_T vectors on as well as the ϕ of the highest E_T cluster. For example, 2-dimensional thrust or sphericity are natural choices. The case of 2-dimensional thrust has been

studied, and found to yield similar results as will be presented for the choice of maximum E_T cluster.

Figure 27 a and b show pE_T distributions for the background, and for 2 cases of signal: $pp \rightarrow \bar{q}q$ with $(m_{\bar{q}}; m_{\bar{g}}) = (100, 50)$ and $(250, 50)$ GeV for events with more than 50 GeV missing E_T . For the case of $(100, 50)$ GeV masses, the signal is clearly visible above the background, and has a totally different shape from QCD. The case of $(250, 50)$ GeV masses is probably not detectable, due to the relatively low rate, and the similarity of shape between it and the QCD background.

In our analysis of CDF, different sets of conditions have been considered and compared. They are the following 3 sets:

1. Missing $E_T > 50$ GeV and $pE_T > 0.48$ to suppress the QCD 2-jet topology.
2. Only two jets in the event (according to the CDF definition of jets) and Missing $E_T > 50$ GeV.
3. Only one jet in the event (according to the CDF definition of jets) and Missing $E_T > 50$ GeV.

The effect of these various filters on the standard background is summarized in Table 12

Table 12: Effect of various filters on the Standard Background at CDF

Background	Cross-sections (in mb) after requiring		
	$0.5 pE_t + E_t^{\text{miss}} > 50 \text{ GeV}$	Biject no $b/\bar{b} + E_t^{\text{miss}} > 50 \text{ GeV}$	Monojet + $E_t^{\text{miss}} > 50 \text{ GeV}$
QCD	5×10^{-36}	5×10^{-35}	5×10^{-36}
$W \rightarrow \tau \nu_\tau$	1.3×10^{-35}	3.1×10^{-36}	5×10^{-36}
$Z^0 \rightarrow \nu \bar{\nu}$	9×10^{-36}	6×10^{-36}	4×10^{-36}
Total: B_{tot}	0.7×10^{-35}	5.9×10^{-35}	1.4×10^{-35}

The effect of these three filters on the Susy signals that we considered here are summarized in Tables 13 a, b and c (respectively corresponding to conditions 1, 2 and 3)

Process ($m\tilde{g}; m\tilde{q}$) (in GeV)		Acceptance (%)		S/\sqrt{B} (in # of σ 's)	Number of remaining events (per $10^{36} \text{ cm}^{-2}/\text{year}$)
(55;50)	7.3×10^{-32}	1.5	44.4	231	1200
(105;100)	1.9×10^{-33}	19	13.7	71	370
(152;150)	1.6×10^{-34}	34	1.8	9.5	50
(50;60)	6.6×10^{-32}	0.3	8.1	42.3	220
(50;100)	3.8×10^{-32}	0.5	7.4	38.5	200
(100;110)	1.9×10^{-33}	11	7.4	38.5	200
(100;150)	9.5×10^{-34}	9	3	15.4	80
(100;200)	7.3×10^{-34}	8	2.2	11.7	61
(150;160)	1.6×10^{-34}	21	1.1	5.8	30
(150;250)	4.9×10^{-35}	31	-	-	1.5
(200;210)	2×10^{-35}	7	-	-	1.5

a

Table 13: Effect of various filters on Susy signals at CDF

Process ($m_{\tilde{g}}; m_{\tilde{q}}$) (in GeV)		Acceptance (%)	S/B	S/\sqrt{B} (in # of σ 's)	Number of remaining events (per $10^{36} \text{ cm}^{-2}/\text{year}$)
(55;50)	7.3×10^{-32}	0.6	7.3	56	430
(105;100)	1.9×10^{-33}	13	4.4	34	260
(152;150)	1.6×10^{-34}	21	0.6	4.4	34
(50;60)	6.6×10^{-32}	0.4	5	39	300
(50;100)	3.8×10^{-32}	0.3	2	15.5	120
(100;110)	1.9×10^{-33}	8	2.5	19.5	150
(100;150)	9.5×10^{-34}	2.3	0.4	2.9	22
(100;200)	7.3×10^{-34}	6	0.8	6	46
(150;160)	1.6×10^{-34}	14	0.4	3	23
(150;250)	4.9×10^{-35}	4	-	-	2.1
(200;210)	2×10^{-35}	16	-	-	3.2
Process ($m_{\tilde{g}}; m_{\tilde{q}}$) (in GeV)		Acceptance (%)	S/B	S/\sqrt{B} (in # of σ 's)	Number of remaining events (per $10^{36} \text{ cm}^{-2}/\text{year}$)
(55;50)	7.3×10^{-32}	0.6	30	112	420
(105;100)	1.9×10^{-33}	10.5	1.4	5.3	20
(152;150)	1.6×10^{-34}	1.4	-	-	2.2
(50;60)	6.6×10^{-32}	-	-	-	-
(50;100)	3.8×10^{-32}	0.06	0.4	1.6	6
(100;110)	1.9×10^{-33}	0.3	0.4	1.6	5.5
(100;150)	9.5×10^{-34}	0.1	-	-	1
(100;200)	7.3×10^{-34}	0.03	-	-	-
(150;160)	1.6×10^{-34}	0.5	-	-	-
(150;250)	4.9×10^{-35}	-	-	-	-
(200;210)	2×10^{-35}	0.75	-	-	-

b

c

We may make the following remarks. First we have imposed a rather tight cut on the E_T^{miss} in all the three filters. This is due to the fact that in the competition started now with ACOL, obviously the aim of the Tevatron is to discover smasses around the m_W . The second remark is that obviously the condition of monojetiness is even more restrictive than what we already got for UA1 case. Imposing such a condition to search for Susy may lead to miss almost completely the signal in many Susy scenarios. From the two other conditions, the pE_T requirement seems again to be the most successful one.

As a final result, a discovery window created by using the numbers of Tables 12 and 13 is shown in Figure 28 for the Tevatron running with a total integrated luminosity of 1 pb^{-1} , data on tape. It seems that provided this total integrated luminosity is recorded by the CDF detector for the next run and that everything goes well, it will be successfully competing with ACOL and UA2 prime and reach limits in the 150-170 GeV mass range, significantly higher than the UA experiments.

The lowest smass that CDF is likely to be sensitive to is between 10 and 15 GeV, somewhat larger than the mass UA1 is sensitive to. This is a trigger threshold problem: CDF must run with higher E_T thresholds than UA1 simply due to the increased center-of-mass energy.

5. "Overlap" between the Tevatron and the Super pp Colliders

If the Tevatron is upgraded towards 1992²⁵ to gain a factor of 50 in luminosity, it means that within 2 years of functioning it will be possible to reach 1 fb^{-1} . Until then by running at $10^{30} \text{ cm}^{-2} \text{ s}^{-1}$ peaked luminosity a few tens of pb^{-1} will be recorded in CDF and D0 detectors²⁶. Therefore the different cases with smasses around the

mw should be well explored by that time.

The next goal is to determine what are the improvements in the limits of detectability of smasses when getting much higher rates. In particular it is very interesting to understand what could be the overlap between the upper limits from the Tevatron and the lower limits of the super pp colliders²⁷ in the region of smass around few hundred GeV.

5.1 Comparison Between the Rates at an Upgraded Tevatron and the SSC

We first refer the reader to the curves of cross-sections for each scenario and each machine as plotted in Figures 3.4 and 5. It is quite striking that passing from 2 TeV to 40 TeV in the c.m. energy provides several order of magnitudes increase in the Susy cross-sections. Let's assume that for the first year the SSC will run with 10^{39} cm^{-2} integrated luminosity (i.e. the same that the upgraded version of the Tevatron). In Table 14 are listed the rates of events provided by each machine for the Susy scenarios which assume smasses varying from 100 to 300 GeV.

Table 14: Comparison between the rates expected from various Susy signals at an upgraded Tevatron and SSC (assuming a total integrated luminosity of 1 fb^{-1} for both machines)

Process ($m_{\tilde{g}} ; m_{\tilde{q}}$) (in GeV)	Rates at the Tevatron (number of events/ 10^{39} cm^{-2})	Rates at the SSC (number of events/ 10^{39} cm^{-2})
(70;161)	5×10^6	1×10^9
(95;218)	6.8×10^5	5×10^8
(140;322)	7.5×10^4	1.5×10^8
(210;463)	3.5×10^3	2.3×10^7
(105;95)	1.5×10^6	4×10^8
(157.5;142.5)	1.5×10^5	1.2×10^8
(210;190)	1.8×10^4	4.5×10^7
(315;285)	7×10^2	1×10^7
(50;250)	1.5×10^5	8×10^8
(100;500)	8×10^2	5×10^7

Before any cut is applied on the data the amount of expected events at the Tevatron, for the cases considered in the Table 14 above are still sufficiently high to allow further filtering to extract the signals. Before doing so let's remind the main results on the detectability of Susy signals at Super pp colliders.

5.2 Detectability of Susy Signals at the Super pp Colliders

We summarize here the main conclusions obtained by comparing the possibilities of the LHC and the SSC working both at $10^{40} \text{ cm}^{-2} \text{ s}^{-1}$ peaked luminosity³. The same "uniform approach" as the one described in Section 2 has been adopted to perform the work with supercolliders. Different situations have been studied which are reported in Fig 1b and are a prolongation in the plane $(m_{\tilde{g}}, m_{\tilde{q}})$ of the cases considered for lower c.m. energy machines.

To extract the Susy signals as simulated at the SSC or the LHC by a 4π fine grained calorimeter, different set of cuts have been worked out³. They are different depending the values of the smasses. For smasses around a few hundred GeV it is sufficient to apply a simple cut on E_T^{miss} of 140 GeV. The ratio S/\sqrt{B} , the statistical significance S/\sqrt{B} of the signal and the number of remaining events after this cut are reasonable to conclude that such signals are detectable both at LHC and SSC machines. For smasses in the range of 500 to 800 GeV, a combined cut on x_E , x_{cut} and E_T^{max} allow to suppress sufficiently enough the QCD, W and Z⁰ backgrounds. For the case around 1 TeV, this combined cut works for the LHC with still the same values. However it start to be hard for this machine to identify these very high smass signals especially when going above 1 TeV. At SSC it seems more easy to scan the region just above the TeV applying the combined cuts but even with tighter values. Even if the photino being the LSP represents only a small fraction of the possible decay modes of the sparticles, still it seems possible to detect them at masses around 1 TeV with the SSC. This is not the case for LHC.

We have summarized in Table 15 the main results of this analysis as well as

the main conclusions. For each process, we give for each machine, the amount of total remaining standard background (B_{tot}) in mbarns, the ratio S/B and the statistical significance S/\sqrt{B} of the remaining signal and the number of events which are left after the filter is applied. The main features of the filtering procedures are also reported in this summary.

Table 15: Detectability of Susy processes at super pp colliders:main results

Process : ($m\tilde{g}$; $m\tilde{q}$) in GeV	B_{tot} (in mb)	S/B	S/\sqrt{B} (in # of σ 's)	Number of left events	Applied cuts
(210;483) (315;285)	0.24×10^{-5} (0.49×10^{-6})	2.5 (1.5) (2.)	1.5×10^4 (3.4×10^3) (4.3×10^3)	6×10^7 (7.3×10^5) (9.6×10^5)	$E_T^{miss} > 140$ GeV
(350;805) (525;475)	1.2×10^{-7} (0.28×10^{-7})	1.7 (2) 2.5 (1.5)	1.8×10^3 ($1. \times 10^3$) 2.6×10^3 (7.5×10^2)	$2. \times 10^5$ (5×10^5) $3. \times 10^6$ ($4. \times 10^5$)	$X_E > 0.24$ and $X_{out} > 0.06$ and $E_T^{max} > 200$ GeV)
(700;1610) (1050; 950)	$< 0.3 \times 10^{-8}$ (0.28×10^{-7})	> 1 (0.1) > 1 (0.05)	175 (20) 225 (40)	$3. \times 10^4$ (2.4×10^4) 3.8×10^4 (1.3×10^4)	$X_E > 0.24$ and $X_{out} > 0.22$ and ($X_{out} > 0.06$ and) $E_T^{max} > 200$ GeV

As a final result of this study we show in Figure 28 the detectability limits on sparticles, that within our "uniform approach", we have determined for each hadron machine already functioning or scheduled. It shows that both the Cern $p\bar{p}$ machine as well as the Tevatron have started very complementary exploration of the mw range for sparticles. That a super $p\bar{p}$ collider option will be a fundamental tool to scan the 1 TeV range if Susy is that high and that in addition it is very interesting to have an upgrade in luminosity of the Tevatron to ensure a good overlap between presently running $p\bar{p}$ machines and the future super $p\bar{p}$ collider option. The upgraded Tevatron will then be able to link the lower mass range with that explorable by the SSC.

6. Conclusions

The sensitivity of detection limits on SUSY signals on details of detector performance, and on analysis strategies, has been illustrated in this paper. We have shown that filtering and analysis of data are strongly related to the properties of the detector which provides them.

During the eighties, after the Cern $p\bar{p}$ collider has started running, theoretical works²⁸ have emphasized the possibility of looking for supersymmetry in hadron-hadron machines.

The discovery of the "supermonojets" in 1984²⁹ increased the excitement on the subject for a short period of time, and some phenomenological works were carried on using Monte Carlos. Our present approach differs in many important ways from these studies.

First it starts with a Monte Carlo which not only contains the hard scattering

process but the complete picture of a $\bar{p} p$ interaction, by including hadronization process and initial and final gluon bremsstrahlung. In the same way are generated the main standard sources of background. Secondly, these events are pushed through the simulation program which fully reproduces the existing detectors (such as UA1 or CDF) or quite realistically models the future 4π general purpose detectors. Finally, the Susy data and the corresponding backgrounds are analyzed in the same way as real data.

This realistic approach to study physics processes such as Susy events, has been initiated for the first time by the working group on "SUSY at the SSC" in Snowmass'84¹⁰. And it has been pursued with existing detectors such as UA1 and CDF³⁰. It is mandatory to have such a complete approach to define relevant limits of detectability of certain new processes.

Moreover, concerning the unique present source of real data, our specific and detailed study of the missing energy events provided by UA1 experiment shows how this detector and different ways to select and analyze data, change, sometimes drastically, the picture of the collected events. For instance we have demonstrated how and why the same process may provide totally different jet patterns. We also think that the 4σ selection followed by the UA1 Collaboration¹⁹ has a too drastic effect on the signal itself. We have shown here how this filter on E_T^{miss} may almost completely miss many possible Susy scenarios.

We have therefore proposed new ways to select such events, i.e. events characterized in a general way by a certain amount of E_T^{miss} and its jet pattern. We have shown how looser cuts on E_T^{miss} combined with requirements on the jet pattern of the

event or other ways to define the Missing energy and the imbalance in energy in the event (such as the use of the variables x_E , x_{out} or pE_T), may be much more successful in overcoming the backgrounds and still keeping a good fraction of the signal.

Furthermore by extrapolating this approach to future detectors at future machines, we are able to determine the limits of detectability of these new possible mechanisms for each considered set-up and a smass range going from a few GeV up to 1 TeV.

Finally, contrary to other approach, we have chosen to adopt a well defined theoretical framework, namely the Supergravity. However it is still sufficiently general: within it we have considered a whole set of different situations which may be quite interesting as in particular the case that we defined as $m_{\tilde{g}} \ll m_{\tilde{q}}$; it may produce very interesting and typical signatures.

These are the main and peculiar points of our so-called "uniform approach". Now we end up by enumerating the main results we obtain with it.

The immense merit of the UA1 experiment has to have provided for the first time a "champ experimental" to develop technics and experience to search for such events in the environment of $\bar{p}p$ collisions. The limits that we have defined and are summarized in Fig 28 are strongly dependent of the Susy scenario and also suffer of the lack of statistics. They cover a more restricted range than the one lately published by the UA1 collaboration and in addition include a detailed study of the "low smass window" (i.e. from a few GeV up to 20 GeV). We think no conclusion so far can be given in this peculiar region. Moreover if the $\tilde{\gamma}$ is not the LSP and so the decay we have studied instead of being 100% B.R. is only few %. Our conclusions are not

anymore valid: therefore, no limits could be given from the 715 nb^{-1} data recorded so far, with this typical signature.

ACOL with few pb^{-1} should be able to explore the m_W range to almost 100 GeV, and the Tevatron with about 1 pb^{-1} should be able to reach 150-170 GeV. Also the two detectors (CDF and new UA's) with their fine grained calorimetry, offer easier ways to "trigger" on the expected "event pattern" than UA1. Certainly the Tevatron with a significant upgrade in luminosity may be a very important tool to overlap with the region in m_{mass} which may be ultimately cover by super pp colliders such as the LHC or the SSC. But this implies that a substantial upgrade in luminosity will be made, otherwise an intermediate step such as a 10 TeV machine would be required to explore the mass range between the W mass and the 1 TeV range. In the case that the Tevatron receives a good upgrade in luminosity, the upgraded Tevatron will be able to link the lower mass range with that explorable by the SSC. On the other hand, ACOL is certainly a unique tool to search for very light gluinos (i.e. $m_{\tilde{g}}$ of the order of few GeV up to about 10-20 GeV which has not yet been clearly rejected by the present UA1 data. This region is much harder to investigate at the Tevatron than it would be at ACOL. The theoretical importance of this case is such that detection of low mass gluinos would be a fundamental discovery.

Acknowledgement:

E. Eichten has provided usefull comments and critics. We have benefit of valuable discussions with C.A. Savoy who has pointed out to us the interest of studying

the case of a very light gluino. J. Ellis has encouraged the work that two of us (ASN and NZ) have performed on super pp colliders at the La Thuile meeting. We would like to thank all three. Finally two of us (JF and ASN) would like to thank respectively Saclay and Fnal Laboratories for their kind hospitality.

References

1. R.Barbieri, S.Ferrara and C.A.Savoy, Phys.Lett.119B, 343(1982)
E.Cremmer, P.Fayet and L.Girardello, Phys.Lett.112B, 346(1983)
S.Ferrara, D.V.Nanopoulos and C.A.Savoy, Phys.Lett.112B, 214(1983)
L.Alvarez-Gaume, J.Polchinski and M.B.Wise, Nucl. Phys. B221, 495(1983)
J.Ellis, J.S.Haguelin, D.V. Nanopoulos and K.Tamvakis, Phys.Lett.125B, 275(1983)
H.P. Nilles, Supersymmetry, Supergravity and Particle Physics, Phys. Rep.
110, 3 (1984).
2. F.E. Paige and S.D. Protopopescu, Isajet Monte-Carlo, BNL-29777, Brookhaven,
1983.
3. A.Savoy-Navarro and N.Zaganidis, "The Search For Strongly Interacting Spar-
ticles At Supercolliders", Preprint CERN-EP 87-165, 9 Sept 1987, Published in
Vol. II of the Proceedings of the Workshop on Physics at Future Accelerators,
La Thuile and Geneva, 7-13 Jan 1987, CERN 87-07, Vol. II, P.82 (1987).
4. L.E.Ibanez and C.Lopez, Nucl. Phys. b223, 511(1984)
C.Kounnas, A.B.Lahanas, D.V. Nanopoulos and M.Quiros, Nucl. Phys. B236,
438(1984)
A.Bouquet, J.Kaplan and C.A. Savoy, Phys. Lett. 148B, 69(1984) and Nucl.
Phys.262B, 299(1985).
5. H.E. Haber and G.L. Kane, Phys.Rep.117, 77(1984) and references therein.

6. R.Barbieri, G.Gamberini, G.F. Giudice and G. Ridolfi, Pisa Preprint IFUP-TH 19 87 (1987), to appear in Nucl. Phys. B.
T.Bartlow, private communication to A.Savoy-Navarro.
7. A. Bartl, H.Fraas and W.Majerotto, "Production and Decay of Selectrons and Squarks in ep Collisions" Preprint HEPHY-PUB 503-87 (June 87).
8. M.J.Herrero, L.Ibanez, C.Lopez and F.J.Yndurain, Phys.Lett.127B, 463(1983)
9. F.Delduc, H.Navelet, R.Peschanski and C.A.Savoy, Phys.Lett.155B, 173(1985)
10. S.Dawson and A.Savoy-Navarro, Report of the Working Group "Searching for Supersymmetry at SSC", in Proc. Summer Study on the Design and Utilization of the Superconducting Super Collider, Snowmass, Colo., 1984, P 263 and Berkeley preprint LBL-18479
The variables x_E and x_{out} , to extract the Susy signals from the standard background, have been introduced first in this workshop.
11. E.Eichten, I.Hinchliffe, K. Lane and C.Quigg Rev. Mod. Phys., Vol. 56, No. 4, P.579 (Oct. 1984) (Based on calculations by Dawson, Eichten, Quigg from Ref.29)
12. E.Eichten, private communication to A.Savoy-Navarro
13. For references on the UA1 detector see the following papers:
A.Astbury et al., "A 4π solid detector", proposal of the UA1 collaboration CERN/SPSC/78-06
Description of the Muon detector:
K.Eggert et al., Nucl.Instr. and Methods 176(1980) 217 and 223.

- G.Bauer et al., Nucl. Instr. and Methods 253(1987)179.
- Description of the Central Tracking:
- M.Calvetti et al., Nucl. Instr. and Methods 176(1980)255
- M.Calvetti et al., IEEE Trans. Nucl. Sci. NS-30(1983)7
- Description of the Central e.m. and hadronic calorimetry:
- C.Cochet et al., Nucl. Instr. and Methods A243(1986)45
- B.Aubert et al., Nucl. Instr. and Methods 176(1980)195
- M.J. Corden et al., Nucl. Instr. and Methods A238(1985)273.
14. N.Zaganidis These Universite Paris XI on "Mesure de l'Energie Transverse Manquante dans l'Experience UA1.Quelques Interpretations Possibles et leurs Perspectives"
- A.Savoy-Navarro "Experimental Puzzles beyond the Standard Model". Invited lectures given at the Advanced Study on Techniques and Concepts of High Energy Physics, St-Croix (Virgin Islands), 19-30 June 1986. Published in the Proceedings and CERN-EP 86-202 (28 Novembre 1986).
15. G.Arnisson et al., Phys.Lett. 132B(1983)214.
16. A.Savoy-Navarro, P.Verrechia and N.Zaganidis "A Software procedure to classify and analyse multijet events". UA1 Technical Note UA1/TN 85-85.
17. J.Hauptman and A.Savoy-Navarro, "Kinematic Isolation and Reconstruction of Hadronic W and Z⁰ decays at a Super Collider". to be published in the Proceedings of the Workshop on Experiments, Detectors and Experimental Areas for the Superconducting Super Collider, LBL, Berkeley , CA July 1-17, 1987.
18. A. Savoy-Navarro "Experimental evidence for the decay $W \rightarrow \tau \nu_\tau$ of the

- charged intermediate boson at the Cern Collider". in Proceedings of the Fifth Topical Workshop on Proton Antiproton Collider Physics. Saint-Vincent 1985. World Scientific, Singapore (1985). P.196 and CERN-EP/85-64
- C.Albajar et al., UA1 Collaboration, Phys.Lett. B185(1987)233.
19. C.Albajar et al., UA1 Collaboration, Phys. Lett. B198(1987)261.
 20. B. Autin, " The New Generation of Antiproton sources" CERN PS/84-22(AA)
E. Jones, "Progress on ACOL" CERN PS 85-14 (AA)
 21. UA1 Collaboration, "Technical Report on the Design of a New Combined Electromagnetic Hadronic Calorimeter For UA1" CERN SPSC/84-72, SPSC P92 ADD.5, 24 Sept. 1984
 22. C.N. Mooth, " The UA2 Experiment at ACOL" CERN EP/87-78 and in the Proceedings of the Vith Topical Workshop on Proton Antiproton Collider Physics. Aachen June 30-July 4, 1986.
 23. For a description of the CDF detector:
F.Bedeschi et al., "Design and Construction of the CDF Central Tracking Chamber"
H.B. Jensen, "CDF Calorimetry" In Proceedings of the International Conference on Advances in Experimental Methods for Colliding Beam Physics, Stanford Linear Accelerator Center, Stanford, CA, March 9-13, 1987 and FERMILAB-Conf-87/62,2563.
 24. J. Freeman, "CDF simulation detector", to be published
 25. Helen Edward "Proposal for an Upgrade in Luminosity of the Tevatron"

26. Design Report: The D0 experiment at the Fermilab Antiproton-Proton Collider. November 1984.
P. Grannis. "The D0 Detector at the Fermilab Collider". D0 Note 558. 5 May 1987 (Submitted to the Proceedings of Les Rencontres de la Vallee d'Aoste) and "Specifications for the D0 Detector". D0 Note 560. Nov. 16. 1987.
27. References for LHC and SSC:
"Proceedings ECFA-CERN Workshop on Large Hadron Collider in the LEP Tunnel". Geneva-Lausanne. 1984 (report ECFA 84-85. CERN 84-101. CERN. Geneva (1984)).
"SSC Central Design Group Conceptual Design of the Superconducting Super Collider". report SSC-SR-2020 (1986).
28. For the search for supersymmetric particles at $\bar{p}p$ colliders, see among others:
G. Altarelli, B. Mele and S. Petrarca. preprint CERN-TH-3822 (1984)
S. Dawson, E. Eichten and C. Quigg. Phys. Rev. D31. 1581 (1985)
J. Ellis and H. Kowalski. Phys. Lett. 142B:441 (1984)
J. Ellis and H. Kowalski. Nucl. Phys. B259:109 (1985)
E. Reya and D.P. Roy. Phys. Lett. 141B:442 (1984) and Phys. Lett. 53:881 (1984).
F. Delduc, H. Navelet, P. Peschanski and C.A. Savoy. Phys. Lett. 155B:173 (1985)
R.M. Barnett, H.E. Haber and G. Kane. Nucl. Phys. B267:625 (1986).
29. G. Arnison et al., Phys. Lett. 139B (1984) 115
30. A. Savoy-Navarro. "Experimental Tests of New Physics". invited talk at the

Conference on Tests of Electroweaks Theories. Polarized Processes and other Phenomena. Miramare-Trieste. 10-12 June 1985 .unpublished.

Figure Caption

1. Set of the different scenarios defined in the scatter plot of $(m_{\tilde{g}} : m_{\tilde{q}})$ and used in our study: a) At low c.m. energies (CERN, FNAL $\bar{p}p$ Colliders), b) At high c.m. energies (LHC, SSC pp Colliders).
2. Comparison between the estimate as done by Isajet and EHLQ¹¹ of the distribution $d\sigma/dm_{\tilde{g}}(pp \rightarrow \tilde{g}\tilde{q} + X)$ (in nb), in function of $m_{\tilde{g}}$ and for different values of the c.m. energy (0.63, 2, 10 and 40 TeV). The values given by Isajet are the black points, the ones given by EHLQ are the white points.
3. Expected cross-sections, assuming $m_{\tilde{g}} < m_{\tilde{q}}$, as a function of $m_{\tilde{g}}$ for the SSC, LHC and FNAL Tevatron for :a) Each of the elementary processes: $pp \rightarrow \tilde{g}\tilde{g}$, $\tilde{g}\tilde{q}$ or $\tilde{q}\tilde{q}$; b) the resulting full production of gluinos and squarks including also the CERN $\bar{p}p$ Collider. The quoted $m_{\tilde{g}}$ refers in fact to the set of values $(m_{\tilde{g}} : m_{\tilde{q}})$ defined in this work for the case $m_{\tilde{g}} < m_{\tilde{q}}$. Quoted cross-sections include a P_T^{\min} cut as described in Section 2.
4. Expected cross-sections, assuming $m_{\tilde{g}} \geq m_{\tilde{q}}$, as a function of the smass for the SSC, LHC and FNAL Tevatron Collider for: a) Each of the elementary processes: $pp \rightarrow \tilde{g}\tilde{g}$, $\tilde{g}\tilde{q}$ or $\tilde{q}\tilde{q}$; b) The resulting full production of gluinos and squarks, including also there the case of the CERN $\bar{p}p$ Collider. The quoted smasses refer to the set of values $(m_{\tilde{g}} : m_{\tilde{q}})$ considered in this work. Quoted cross-sections include a cut on P_T^{\min} as defined in Section 2.
5. Total expected rates per year, per Susy scenario and for various pp Colliders:

- a) The CERN $\bar{p}p$ Collider and a total integrated luminosity of 715 nb^{-1}
 - b) The 4 pp Colliders considered in this study, as a function of smass for the scenario where $m_{\tilde{g}} \geq m_{\tilde{q}}$.
 - c) The 4 pp Colliders and as a function of the gluino mass for the scenario where $m_{\tilde{g}} < m_{\tilde{q}}$.
 - d) The Tevatron, the LHC and SSC machines as a function of the gluino mass in the case of a very light gluino compared to a relatively heavy squark.
6. E_T^{miss} distributions at ACOL as given by various processes:
- a) For the decay of the W into $\tau\nu$ - and two different values of the P_T^{mun} threshold applied
 - b) For the QCD process and two different values of the P_T^{mun} threshold applied
 - c) For two Susy signals. One corresponds to the case where $m_{\tilde{g}} = 35 \text{ GeV}$ and $m_{\tilde{q}} = 80 \text{ GeV}$. The other one corresponds to the case where $m_{\tilde{g}} = 84 \text{ GeV}$ and $m_{\tilde{q}} = 80 \text{ GeV}$.
7. Resolution on the components of the total energy in UA1 for minimum bias data
- a) Vector sum of the X-component of the energy vector $\sum_i \vec{E}_{Xi}$ versus E_T^{tot} and Vector sum of the Y-component of the energy vector $\sum_i \vec{E}_{Yi}$ versus E_T^{tot}
 - b) Resolution on E_T^{tot} in the UA1 experiment for minimum bias and jet triggered events.
8. Flow diagram of the data selection for missing energy events in the UA1 experiment
9. Efficiency of the filter "4 σ " (defined by $E_T^{\text{miss}} > 4\sigma$) in the UA1 detector, in

function of the gluino mass: a) for the case where $m_{\tilde{g}} < m_{\tilde{q}}$ and b) for the case where $m_{\tilde{g}} \geq m_{\tilde{q}}$.

10. Different views given by the interactive display facility in UA1 of an event generated by the process $pp \rightarrow \tilde{g}\tilde{q}$ with $m_{\tilde{g}} = 21$ GeV and $m_{\tilde{q}} = 19$ GeV and with the gluino decaying into $\bar{q}q$ and the squark into $q\tilde{\tau}$. It is then fully simulated in the UA1 detector. It shows a clear monojet structure.
11. Different views given by the interactive display facility in UA1 of an event generated by the process $pp \rightarrow \tilde{g}\tilde{q}$ with $m_{\tilde{g}} = 63$ GeV and $m_{\tilde{q}} = 57$ GeV. The gluino decays into $\bar{q}q$ and the squark into $q\tilde{\tau}$. This event fully simulated in the UA1 detector shows a typical monojet structure.
12. Event generated according to the same conditions than in Figure 11 but now it shows a clear bijet no $b\bar{b}$ structure.
13. Event generated according to the same conditions as in Figure 11 but showing now a clear trijet structure.
14. Different views as given by the interactive display facility in UA1. of an event generated according to the process $pp \rightarrow \tilde{g}\tilde{q}$ with $m_{\tilde{g}} = 10$ GeV and $m_{\tilde{q}} = 100$ GeV. The gluino decays into $q\bar{q}\tilde{\tau}$ and the squark decays into $q\tilde{\tau}$. It is fully simulated in the UA1 detector and shows a typical monojet structure.
15. Distribution of the average values of the a) E_T of the trigger jet and b) E_T^{miss} for all the different Susy scenarios considered in this study for the case of the CERN $\bar{p}p$ Collider.
16. Evolution of the distributions of the main characteristics of Susy events in the

- case where $m_{\tilde{g}} \geq m_{\tilde{q}}$, when the smass varies from 20 to 80 GeV at 630 GeV c.m. energy:
- a) Evolution of the E_T spectrum of the trigger jet
 - b) Evolution of the E_T^{miss} spectrum for these events
17. Evolution of the distributions of the main characteristics of Susy events in the case where $m_{\tilde{g}} < m_{\tilde{q}}$, when the smass varies from 20 to 80 GeV at 630 GeV c.m. energy:
- a) Evolution of the E_T spectrum of the trigger jet
 - b) Evolution of the E_T^{miss} spectrum for these events
18. Main characteristics of the events produced at 630 GeV c.m. energy, by the process $pp \rightarrow \tilde{g}\tilde{q}$ with $m_{\tilde{g}} = 10$ GeV and $m_{\tilde{q}} = 100$ GeV. The gluino decays into $q\tilde{q}\tilde{\gamma}$ and for the squark the two possible decay modes are considered, namely $q\tilde{\gamma}$ (dashed line) and $q\tilde{g}$ (full line):
- a) $E_T^{(\text{jet})}$ distributions given by these events for the two considered decay modes of the squark.
 - b) E_T^{miss} distributions given by these events for the two considered decay modes of the squark.
19. Study of the difference in θ and ϕ , between the two gluons issued from hard scattering $q,g \rightarrow \tilde{g}_1\tilde{g}_2$, after the cascade shower process (gluon bremsstrahlung):
- a) $\delta\theta'(\tilde{g}_1, \tilde{g}_2)$ distribution
 - b) $\delta\phi'(\tilde{g}_1, \tilde{g}_2)$ distribution
20. Difference in θ and ϕ between the gluino and the squark decay product of the gluino:

- a) $\Delta\theta(\tilde{g}, \tilde{q})$ distribution
 - b) $\Delta\phi(\tilde{g}, \tilde{q})$ distribution.
21. P_T -distribution of each quark decay product of the gluino
 22. $\Delta R(q, q)$ distribution between the two quarks which are the final decay products of the gluino decay
 23. Various E_T^{miss} distributions as given by QCD for different values of the P_T^{min} threshold, varying from 20 to 50 GeV/c applied on the P_T of the primary partons at $\sqrt{s} = 630$ GeV.
 24. Some views as given by the display facility of the CDF experiment, of an event generated according to the process $pp \rightarrow \tilde{g}\tilde{q}$ with $m_{\tilde{g}} = 100$ GeV and $m_{\tilde{q}} = 200$ GeV. The gluino decays into $q\bar{q}\tilde{\gamma}$ and the squark decays into $q\tilde{g}$. The event is fully simulated in CDF detector
 - a) Shows the Lego plot view of the event as given by the CDF calorimetry.
 - b) Shows a transverse view of the event as seen by the Central Tracking (CTC chambers)
 25. Various views as given by the display facility of the CDF experiment of an event generated according to the process $pp \rightarrow \tilde{g}\tilde{q}$ with $m_{\tilde{g}} = 105$ GeV and $m_{\tilde{q}} = 100$ GeV. The gluino decays into $\bar{q}\tilde{q}$ and the squark decays into $q\tilde{\gamma}$. The event is fully simulated in the CDF detector.
 - a) Shows the Lego plot view of the event as given by CDF calorimetry
 - b) Shows a transverse view of the event as seen by the central tracking (CTC chambers).

26. Comparison of some of the main characteristics of the Standard Background and Susy signals in the CDF detector. The standard background includes QCD process as well as the decay of the W into $\tau\nu_\tau$ and of the Z^0 into $\nu\nu$. The Susy signals correspond to the process $pp \rightarrow \tilde{g}\tilde{q}$ with $m_{\tilde{g}} = 50$ GeV and $m_{\tilde{q}} = 100$ GeV.
 - a) E_T^{miss} distribution for these processes
 - b) Monojet E_T distribution for these processes.
27. pE_T distributions for various standard backgrounds and Susy signals in the CDF detector.
28. Limits of detectability derived for the CERN $\bar{p}p$ Collider, the FNAL Tevatron and the LHC and the SSC, as a function of the masses of the gluino and squark, within the framework of the "uniform approach" used here.

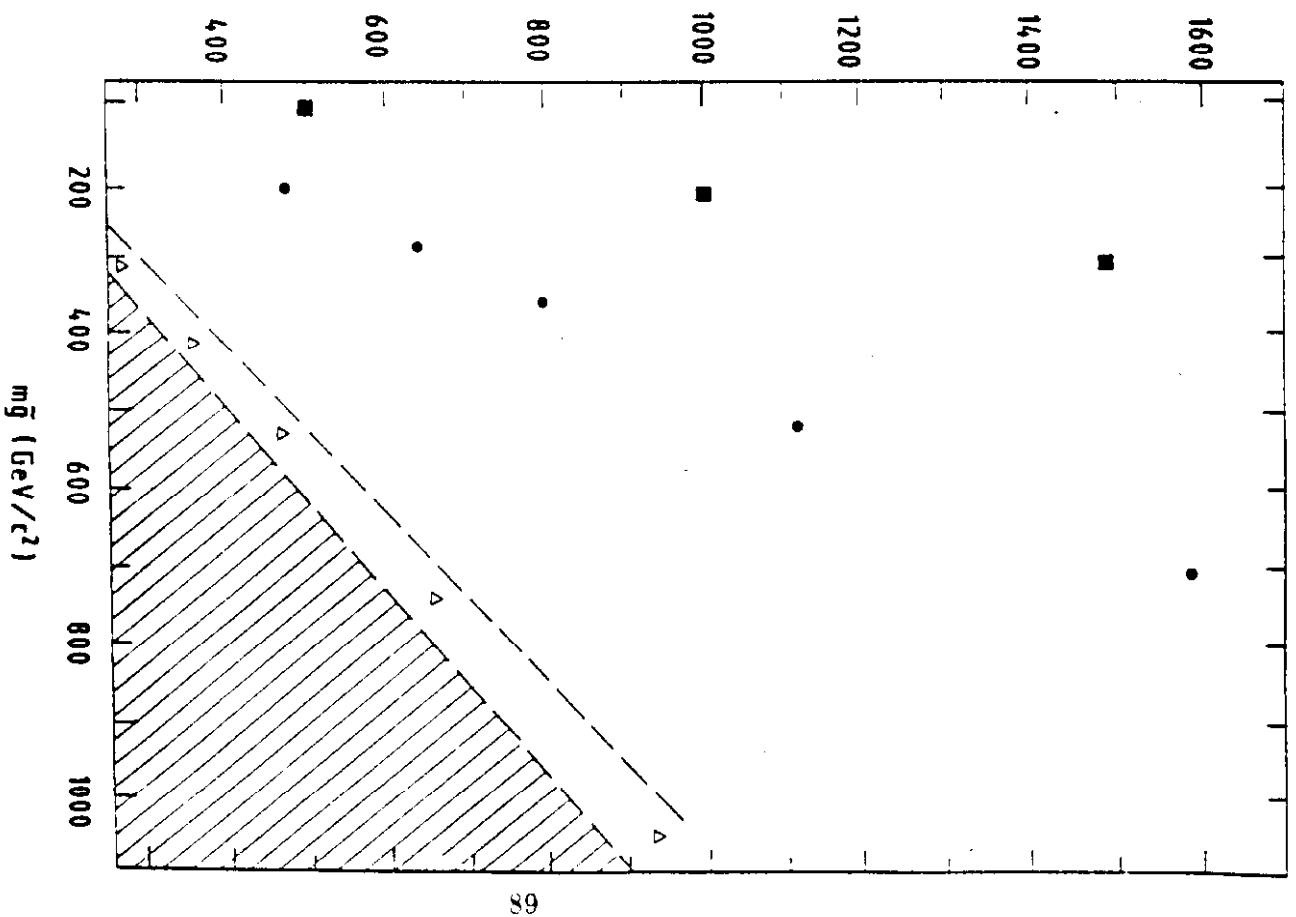
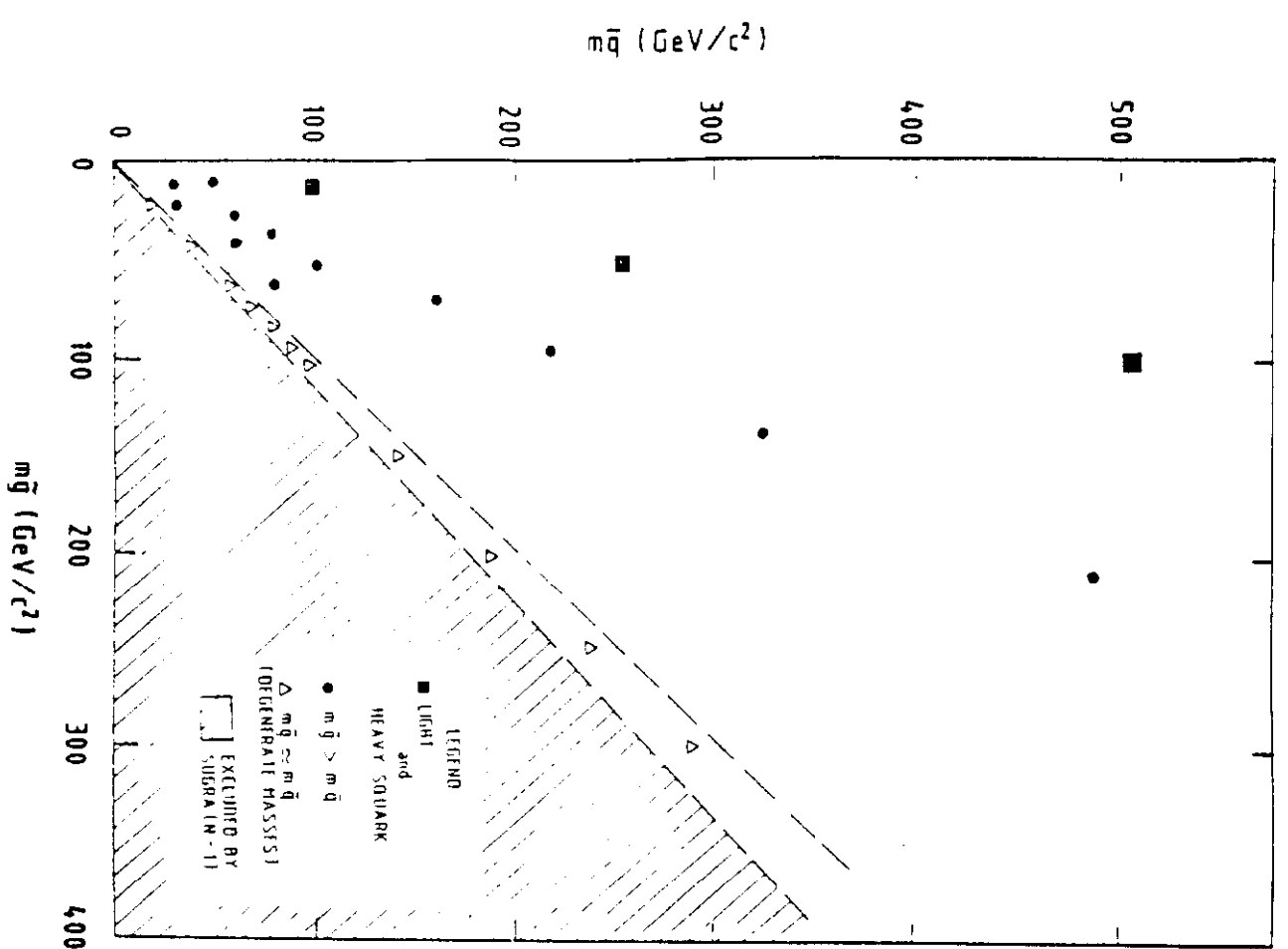


Fig. 1

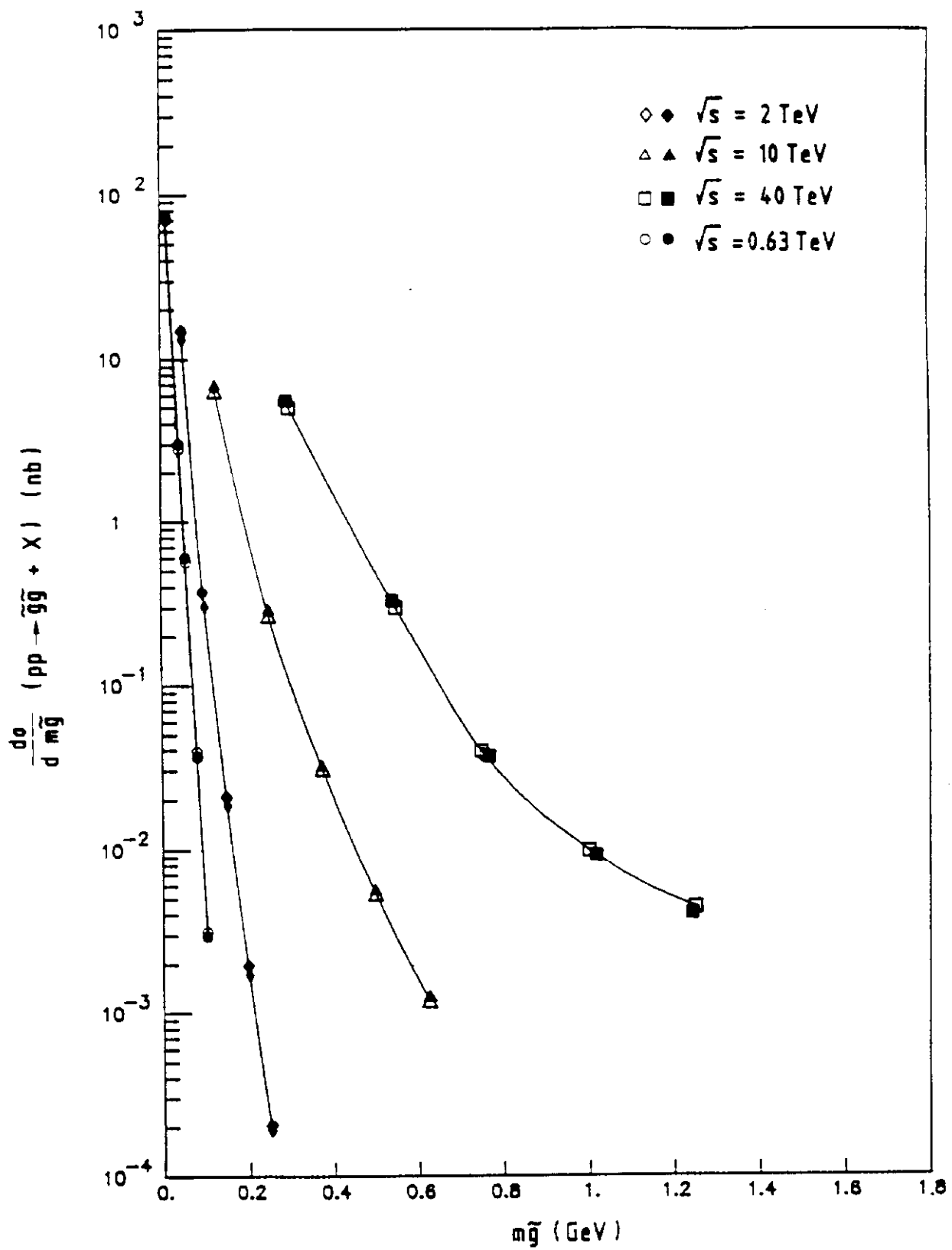


Fig. 2

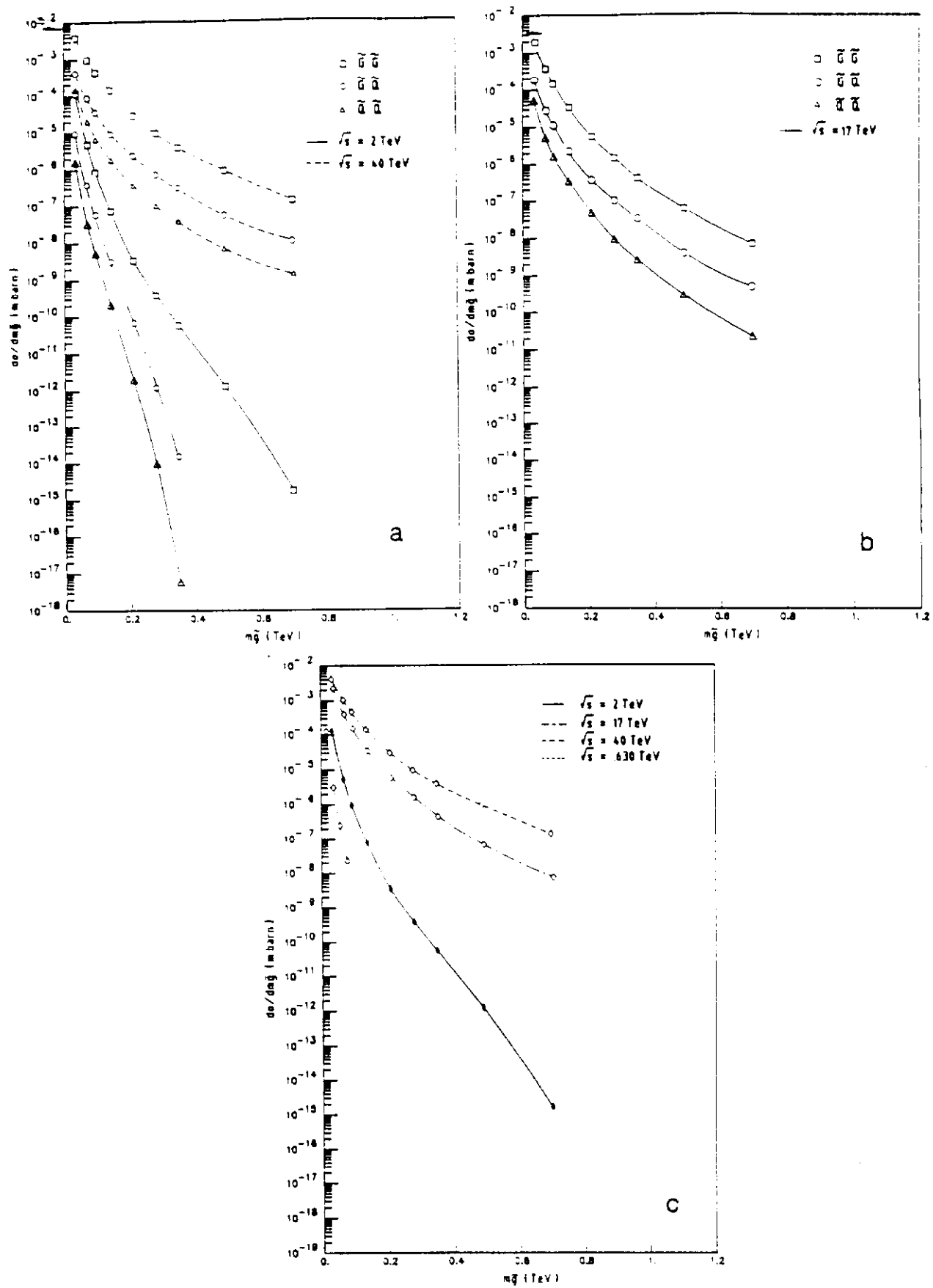
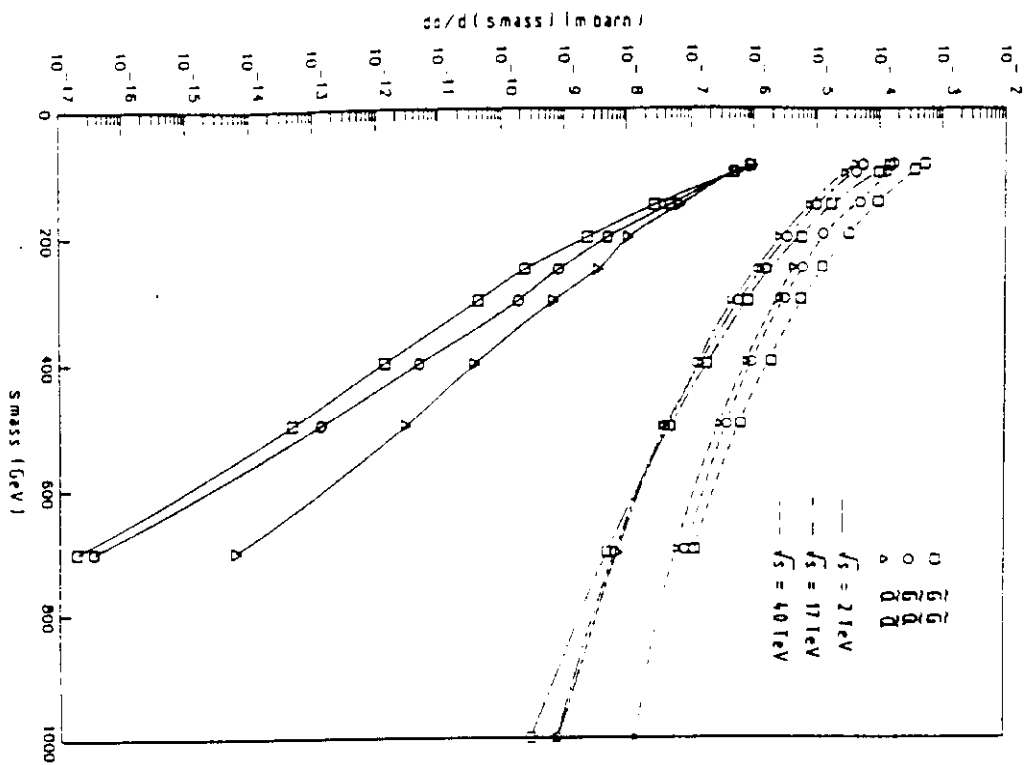
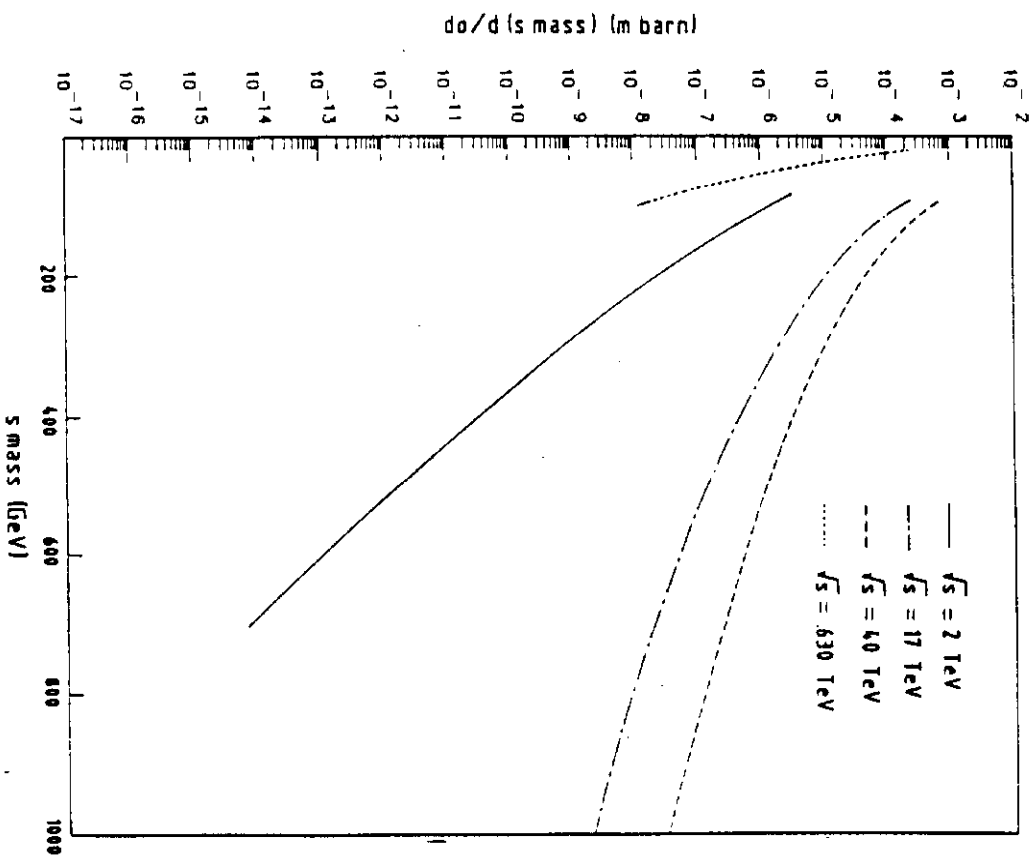


Fig. 3



a



b

Fig. 4

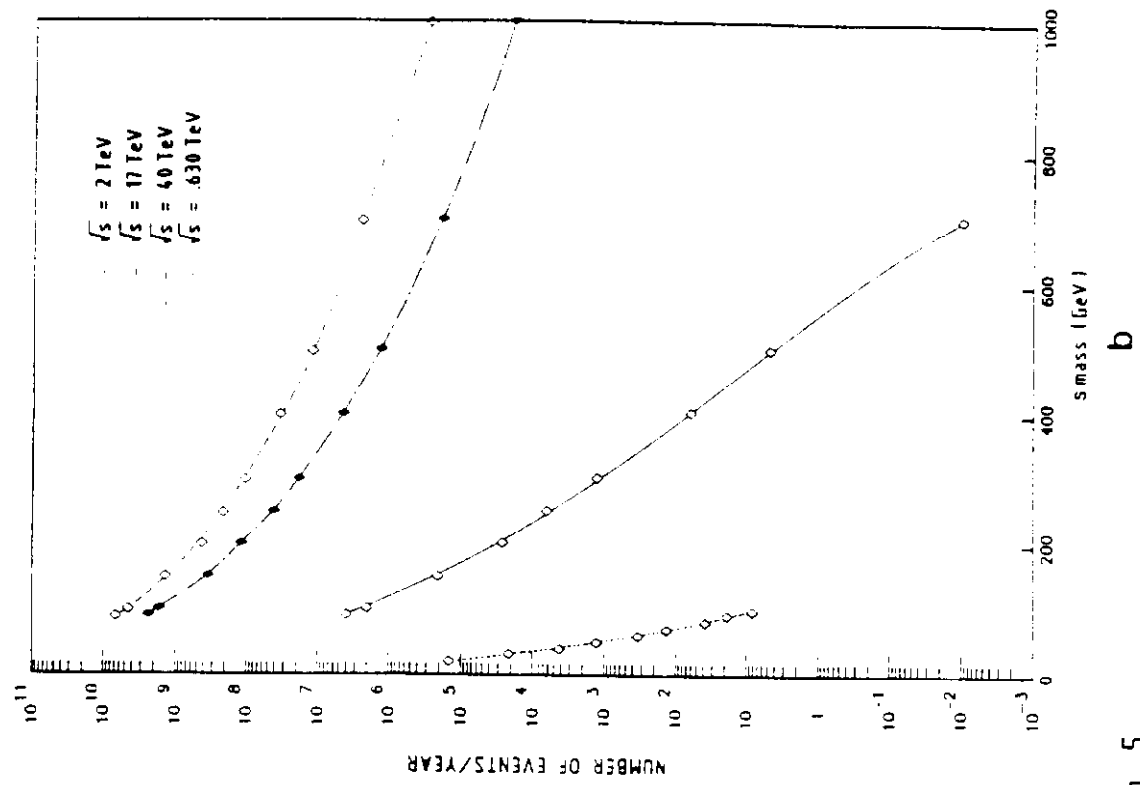
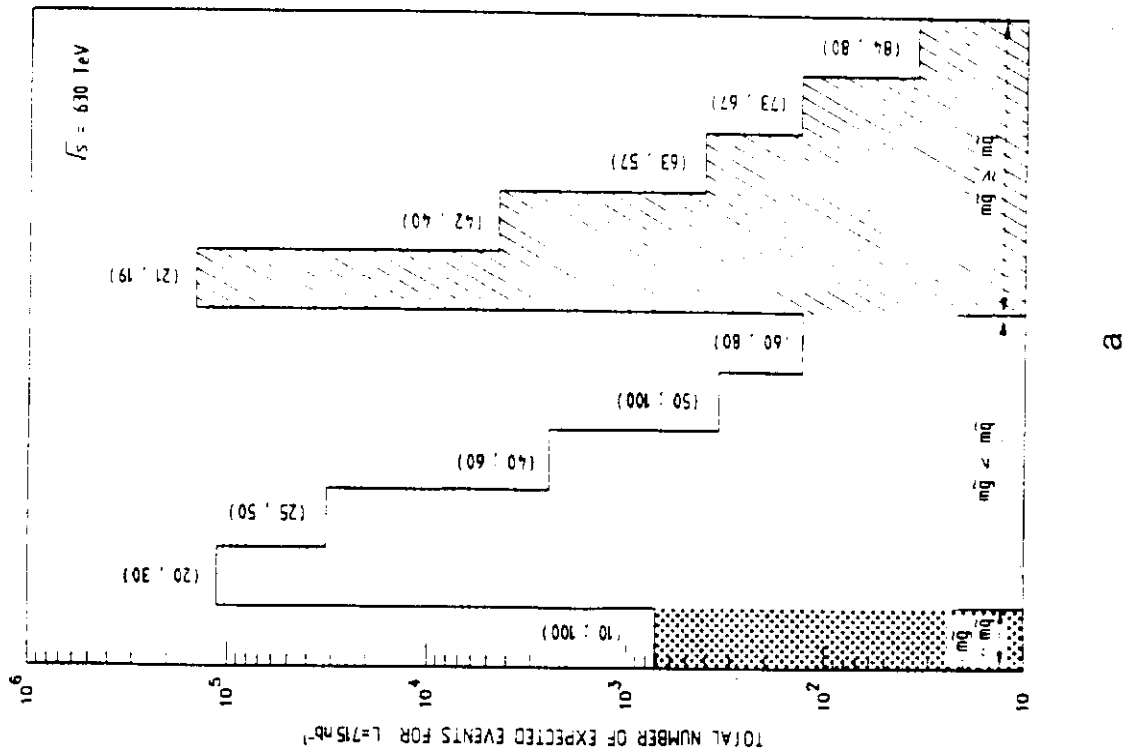


Fig. 5

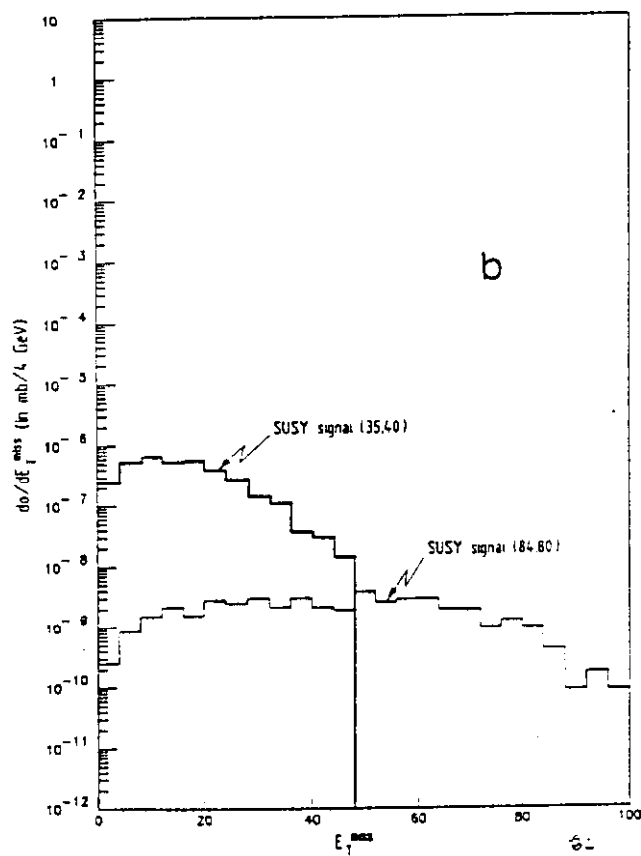
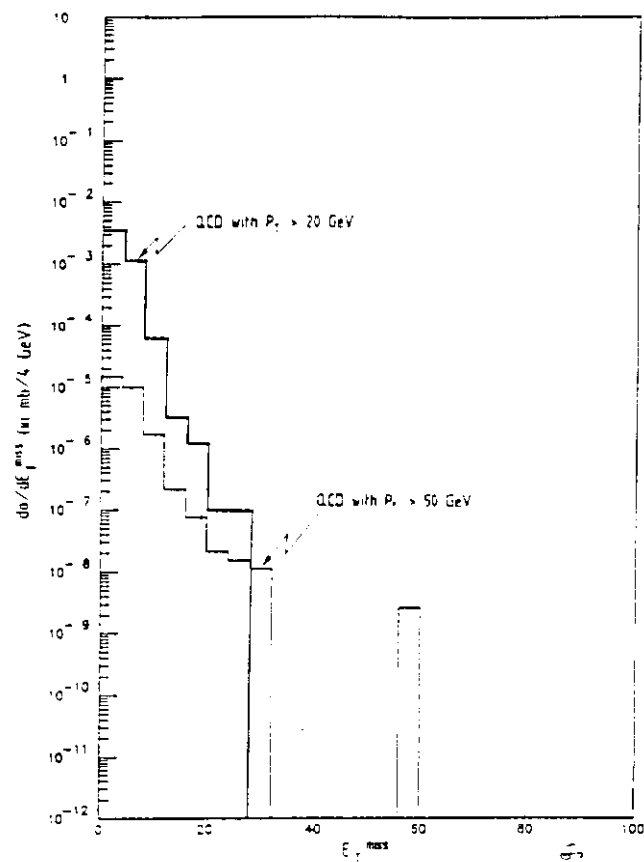
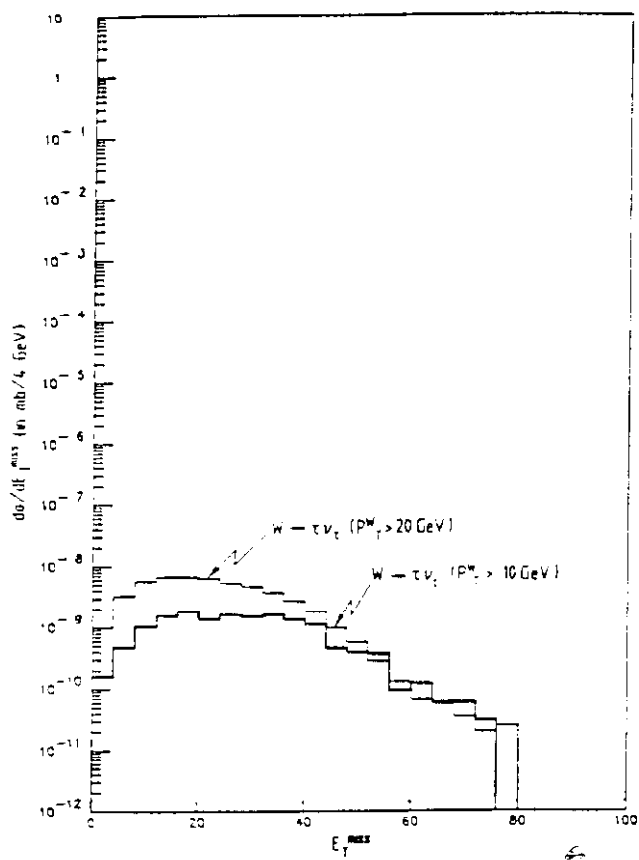


Fig. 6

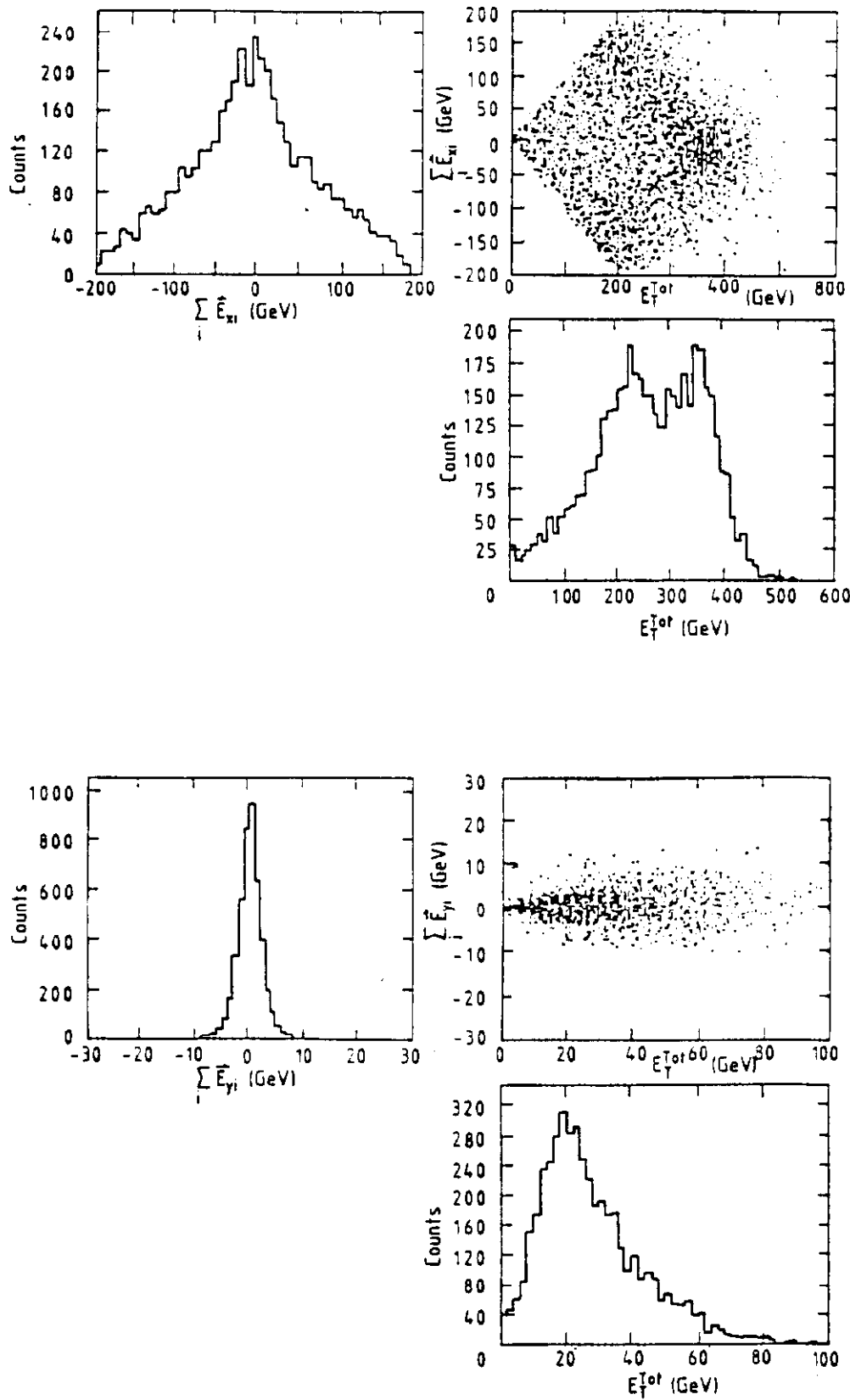


Fig. 7a

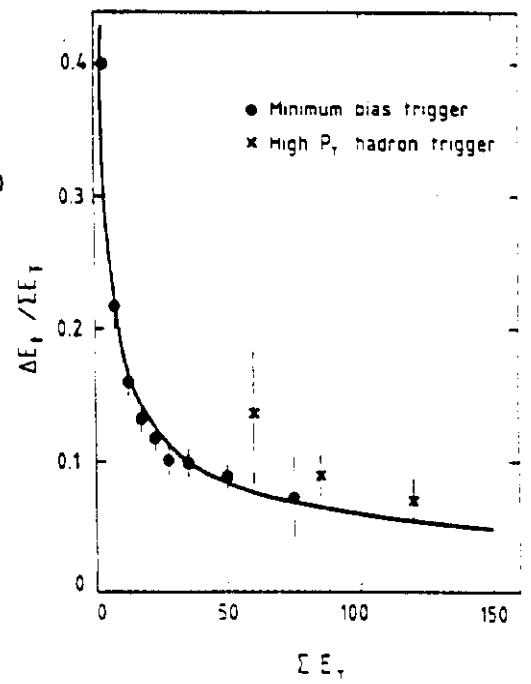
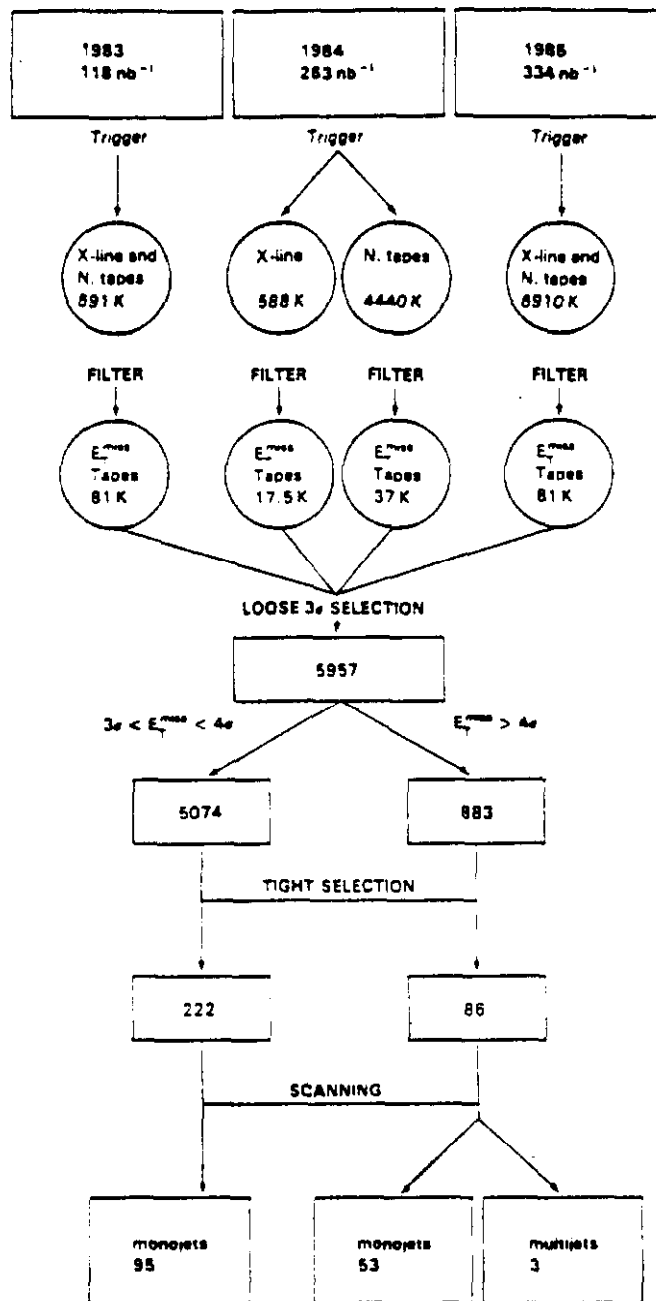


Fig. 7b



Flow diagram of the data selection for missing energy events in the UA1 experiment.

Fig. 8

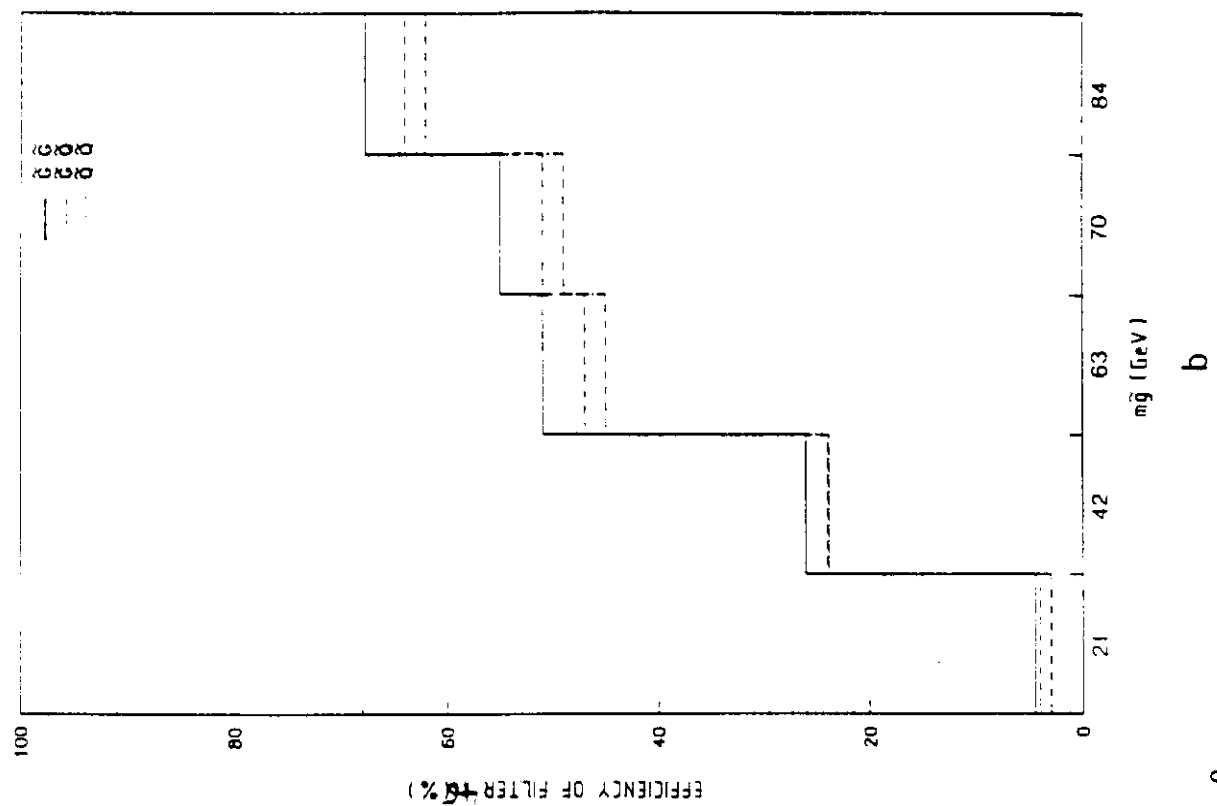
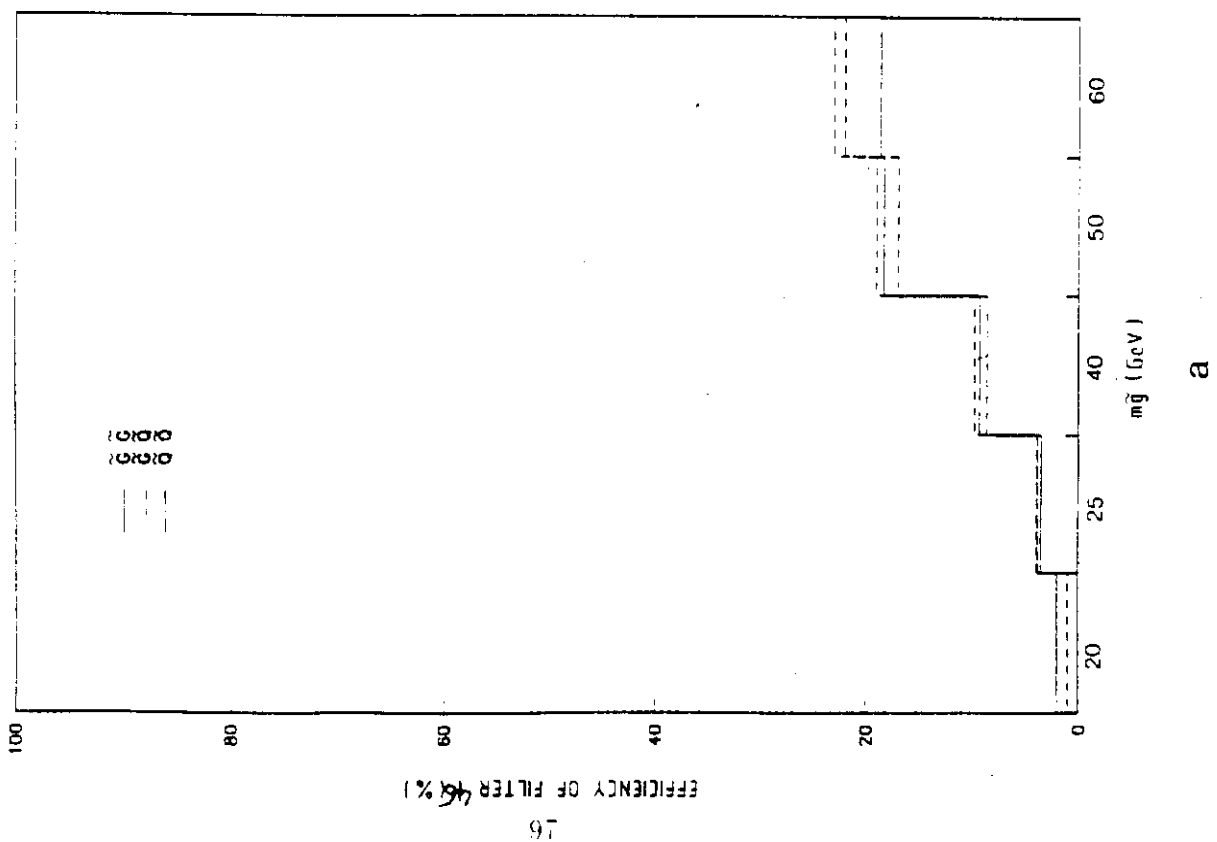


Fig. 9

Figure 10

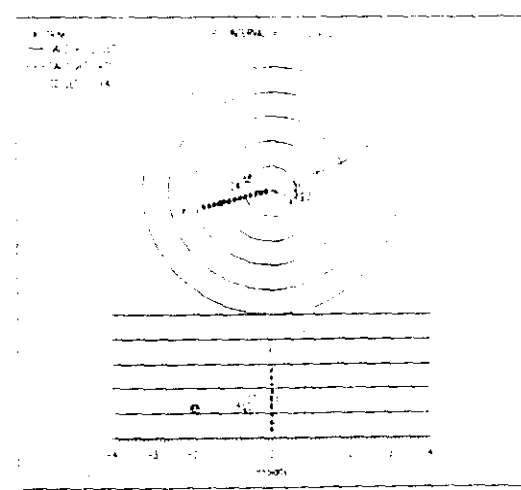
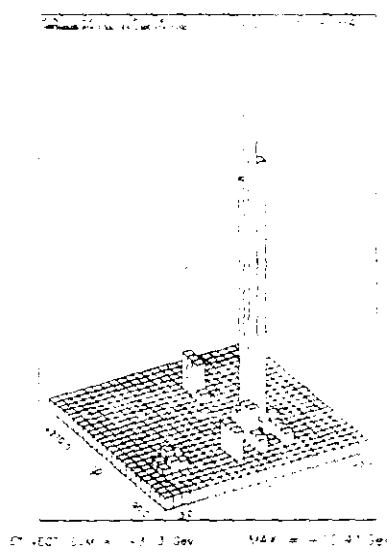
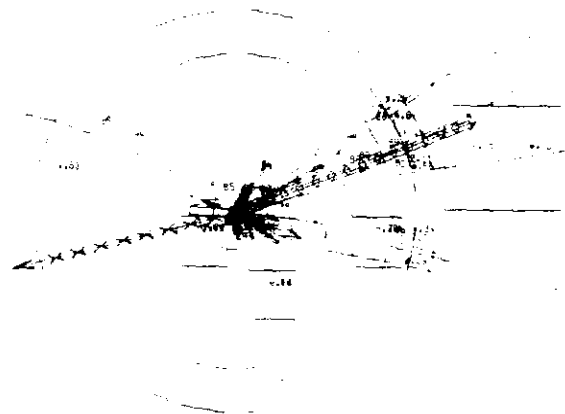
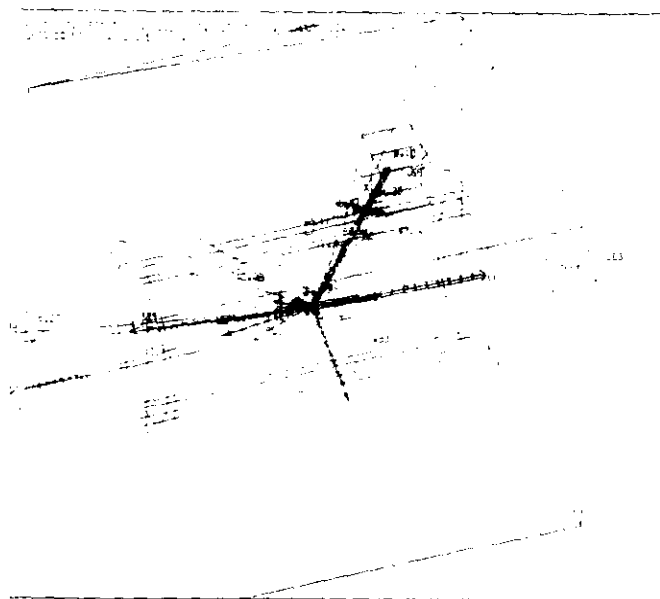
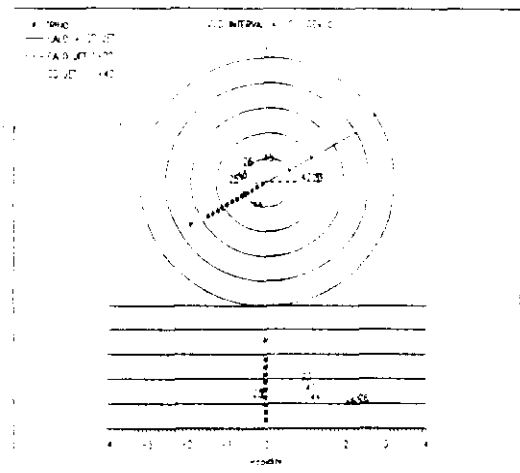
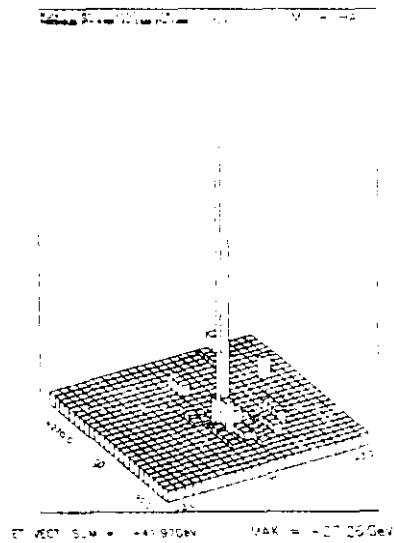
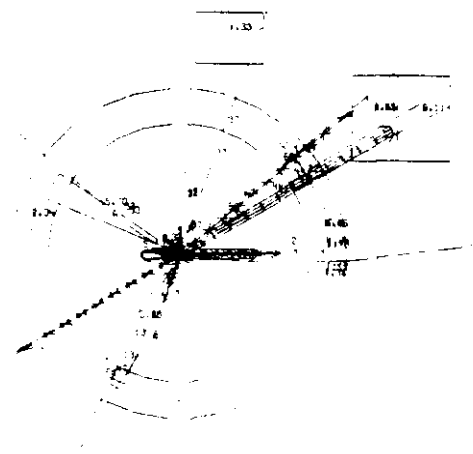
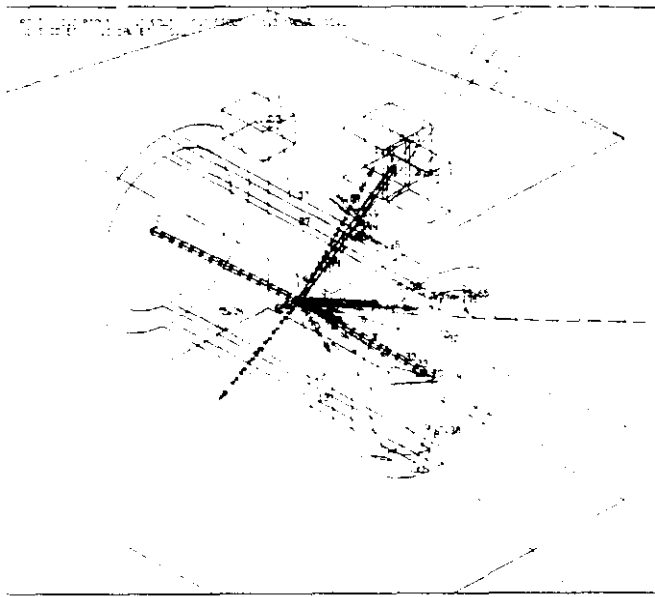


Figure 11



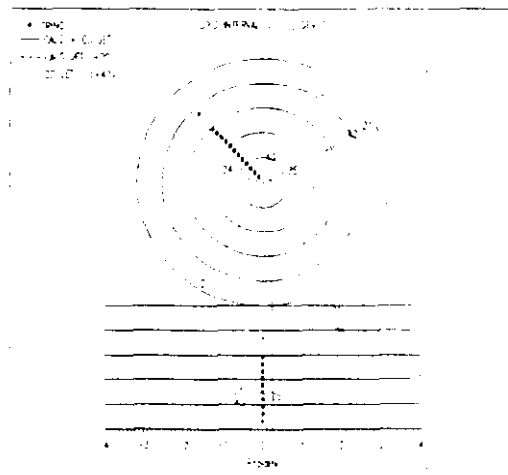
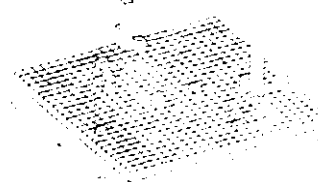
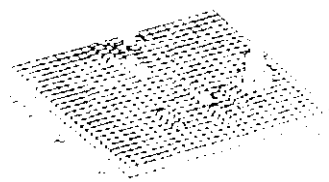
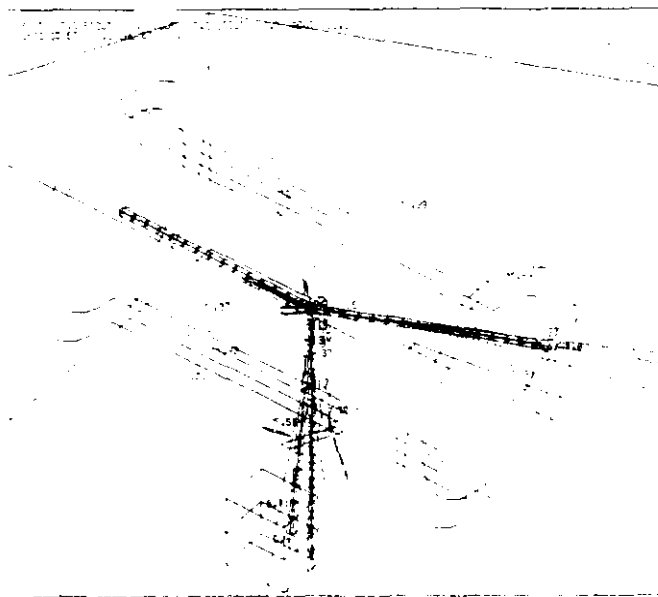


Fig. 12

Figure 13

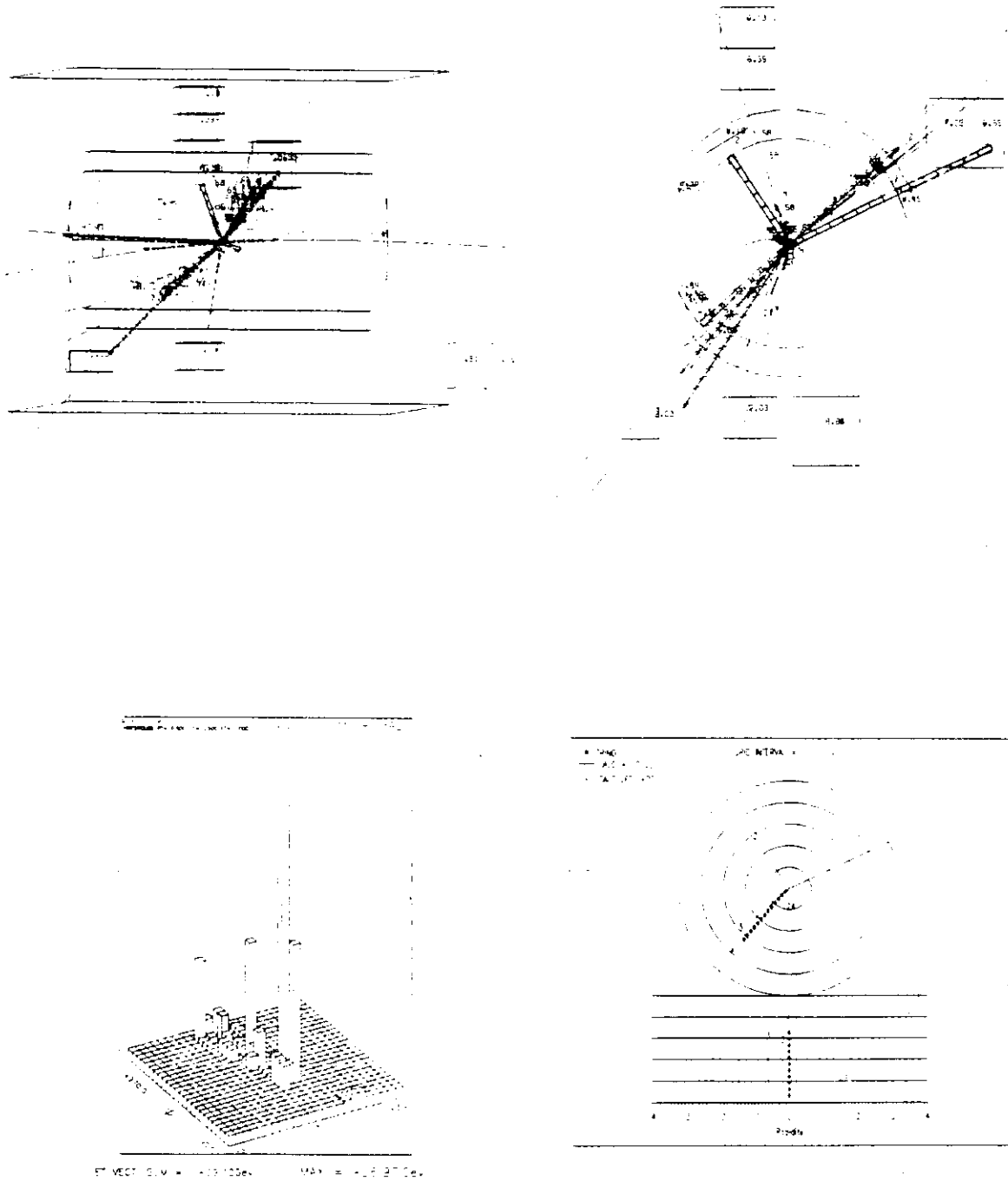
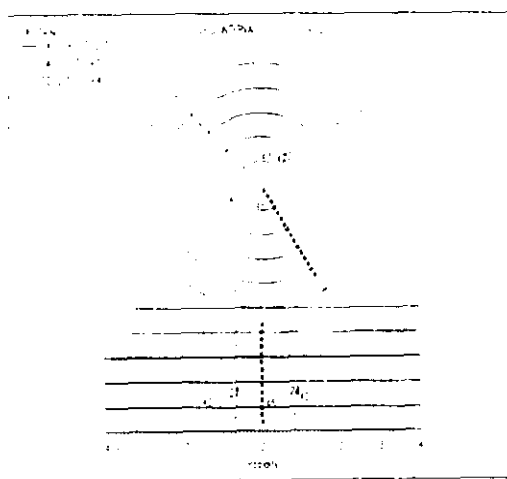
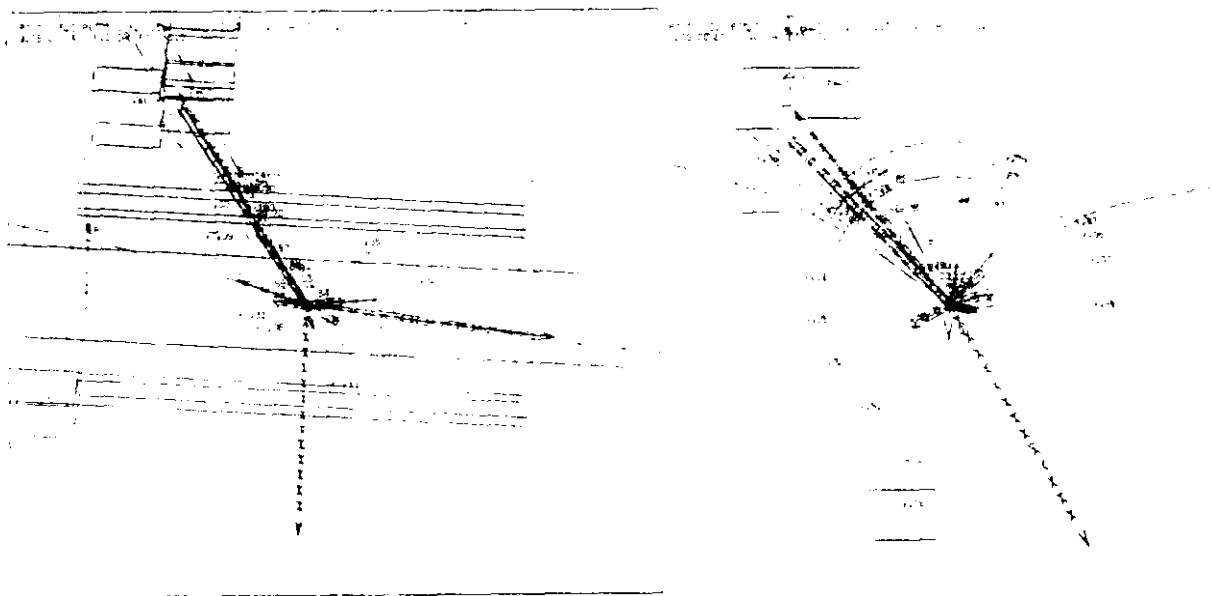
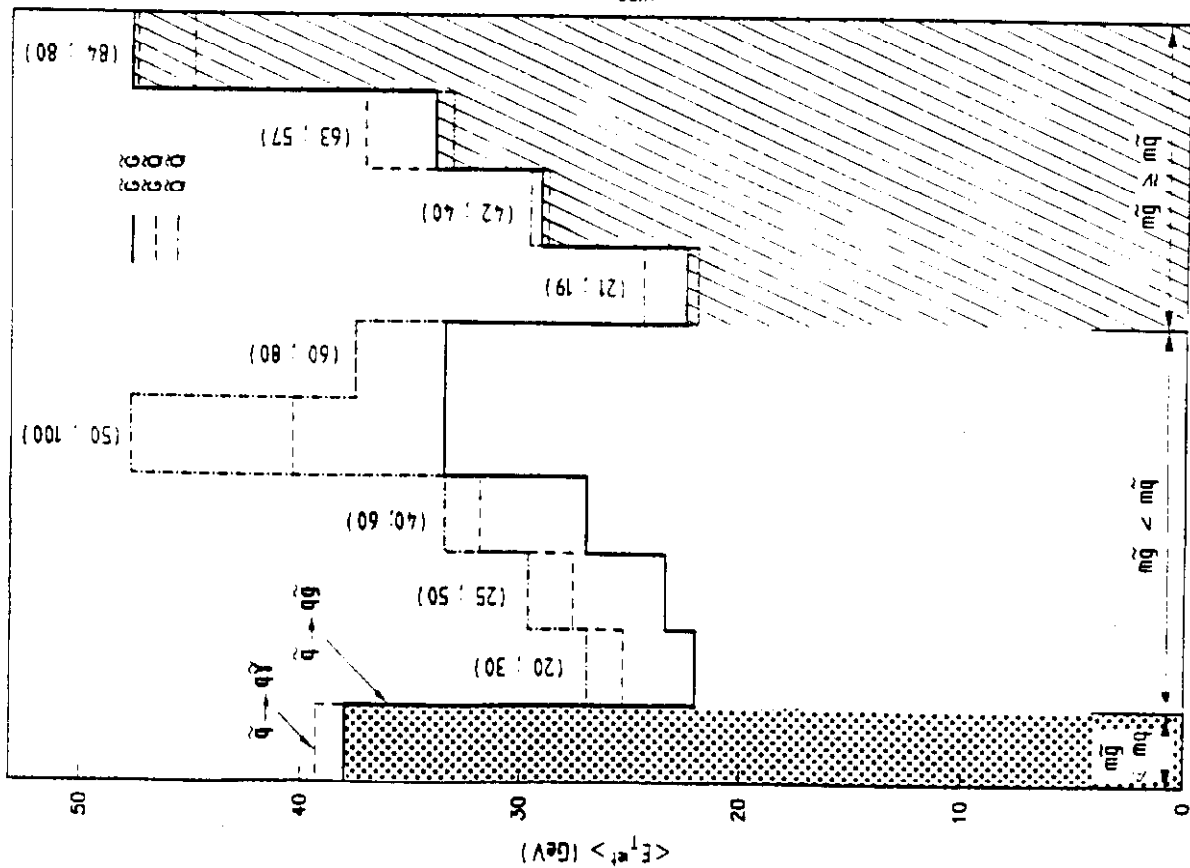
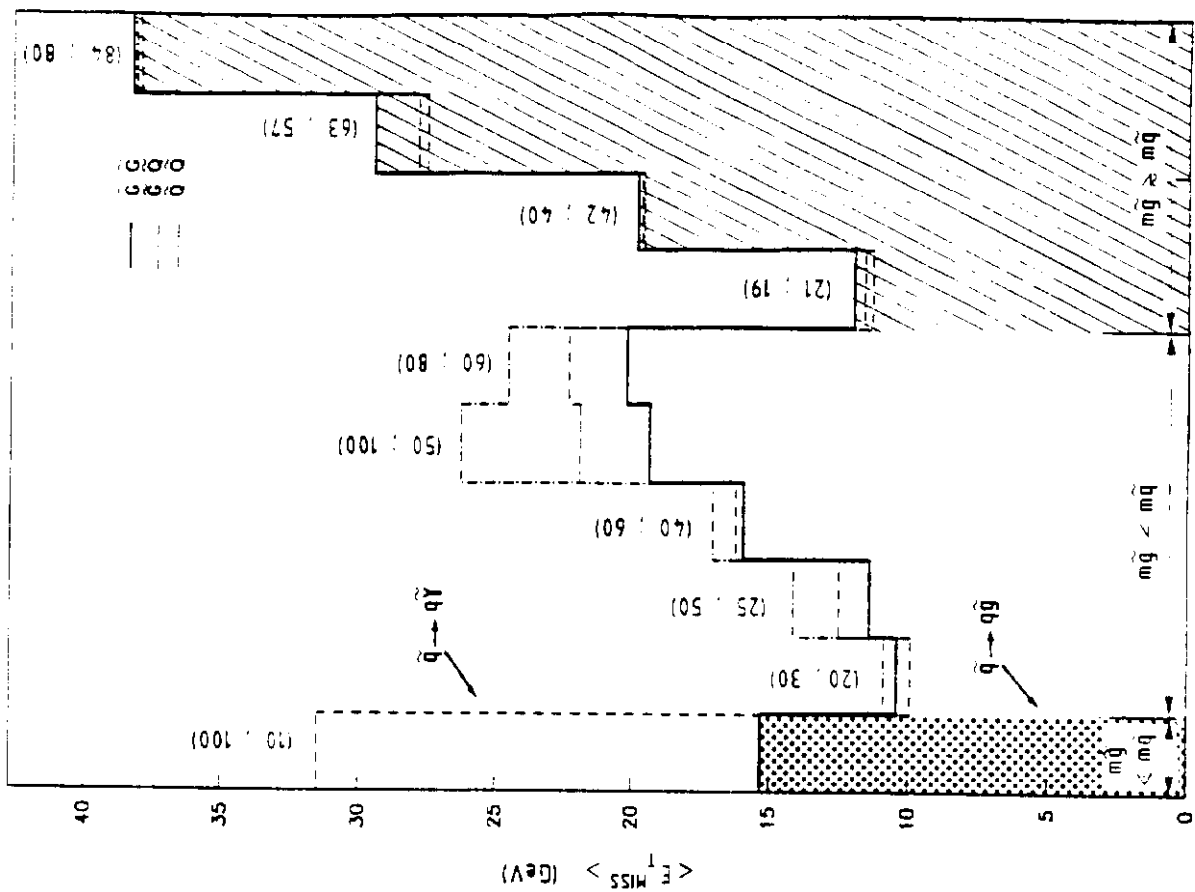


Figure 14





a



b

Fig. 15

a

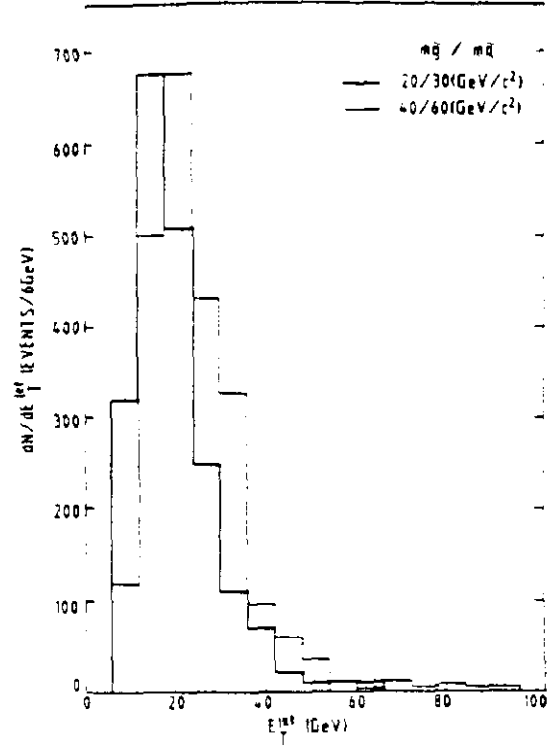
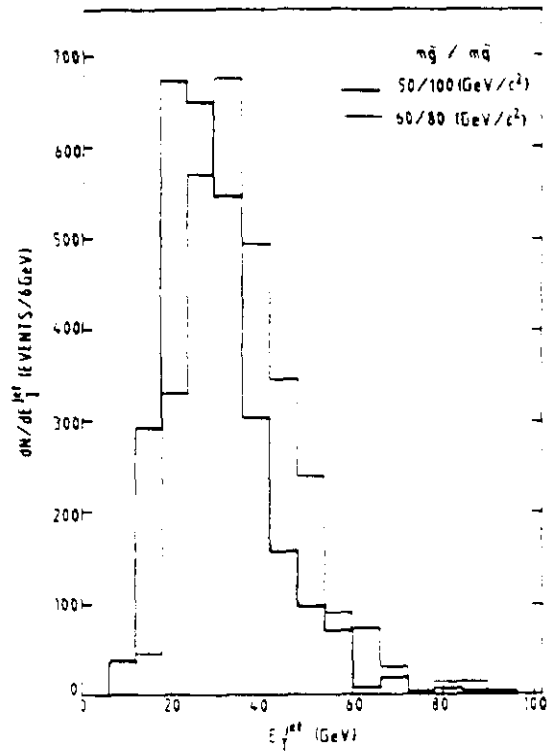
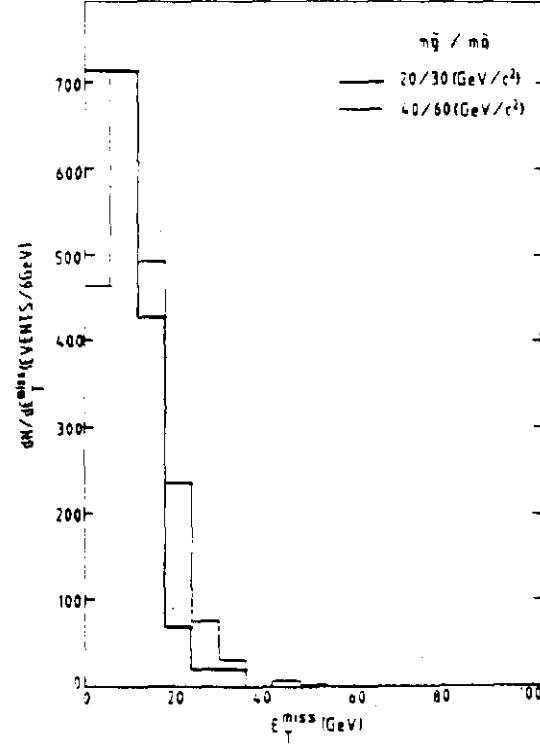
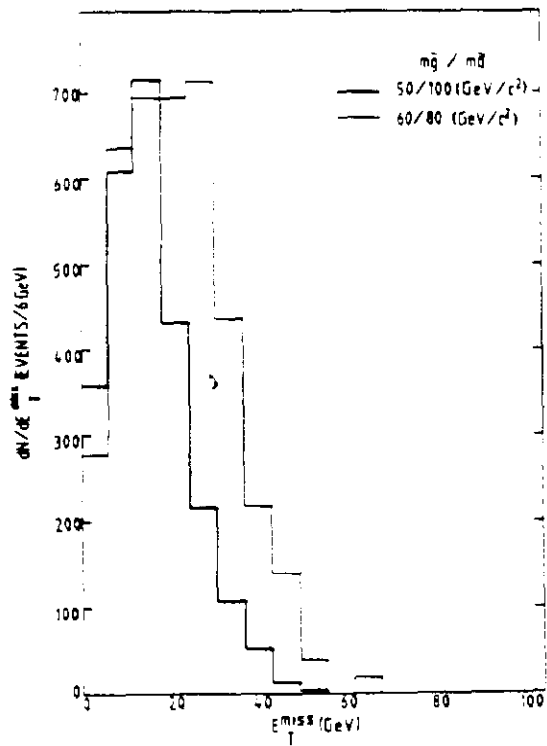


Fig. 16

b



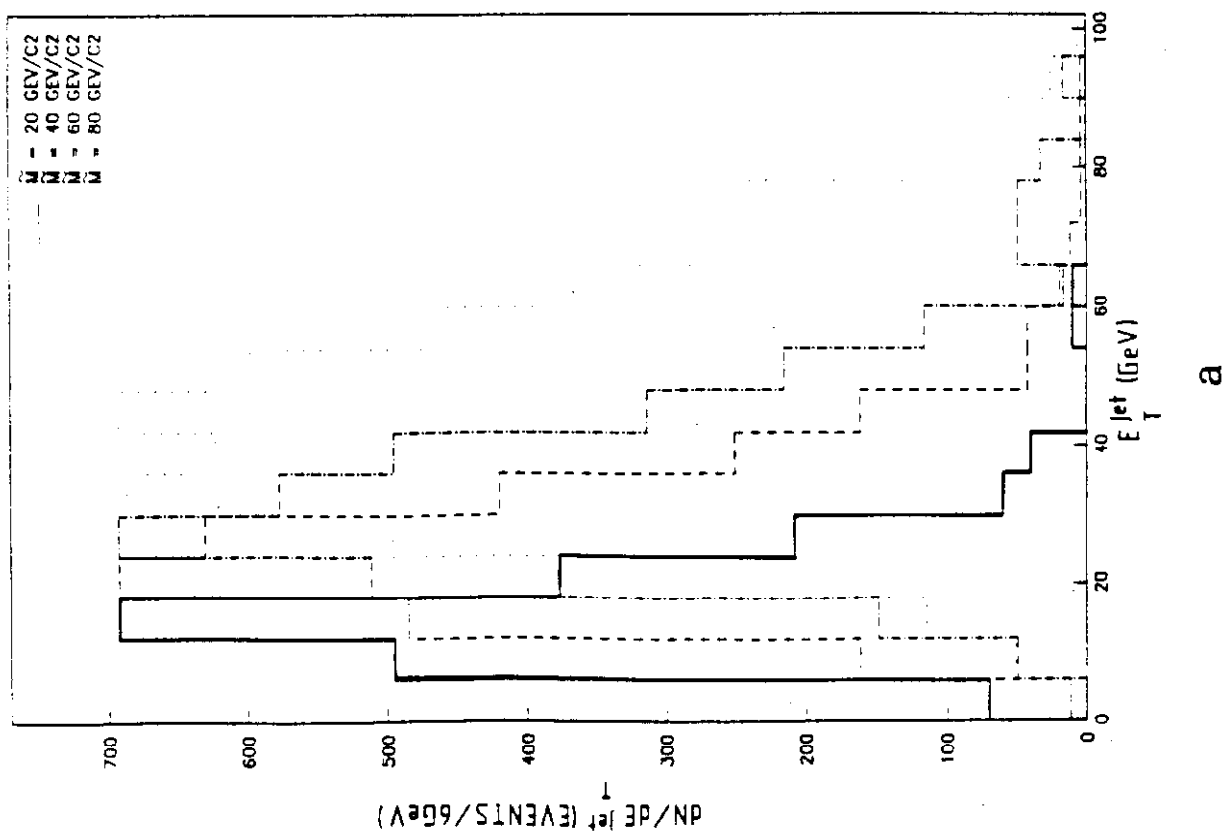
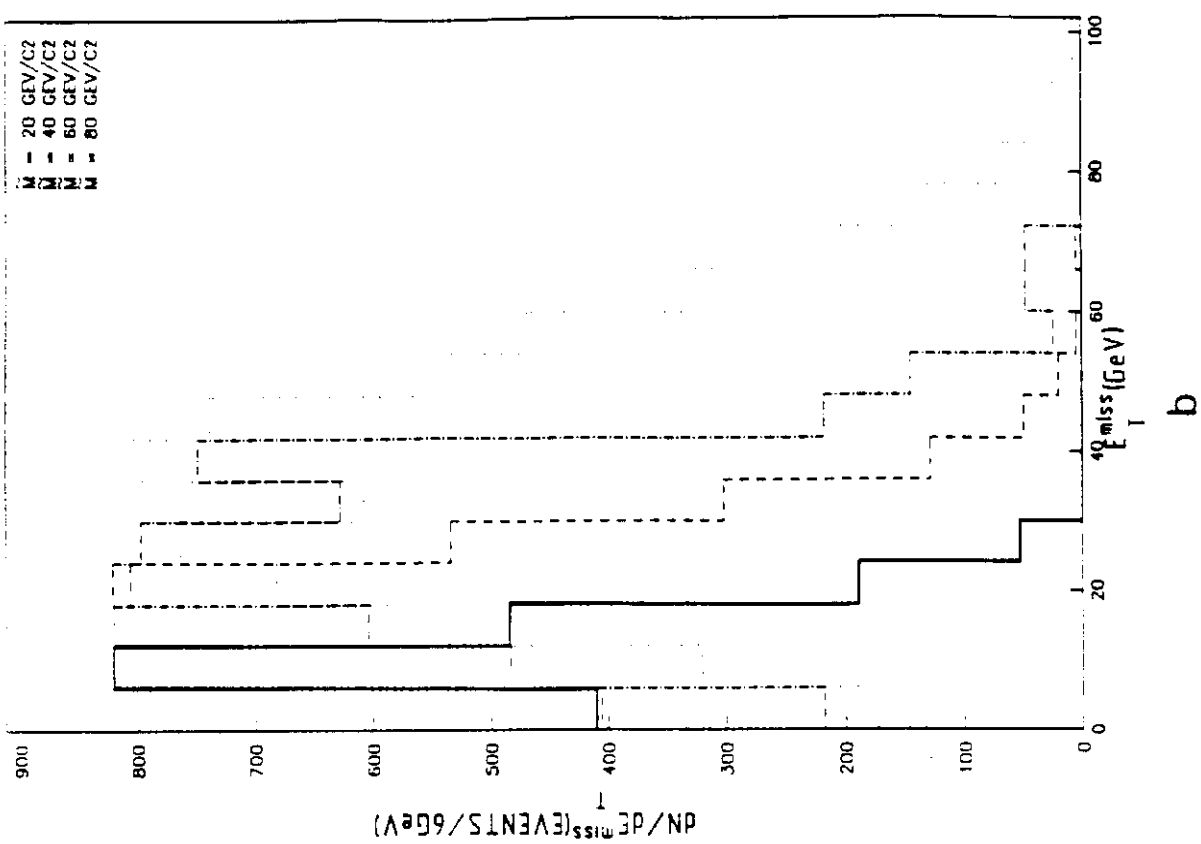


Fig. 17

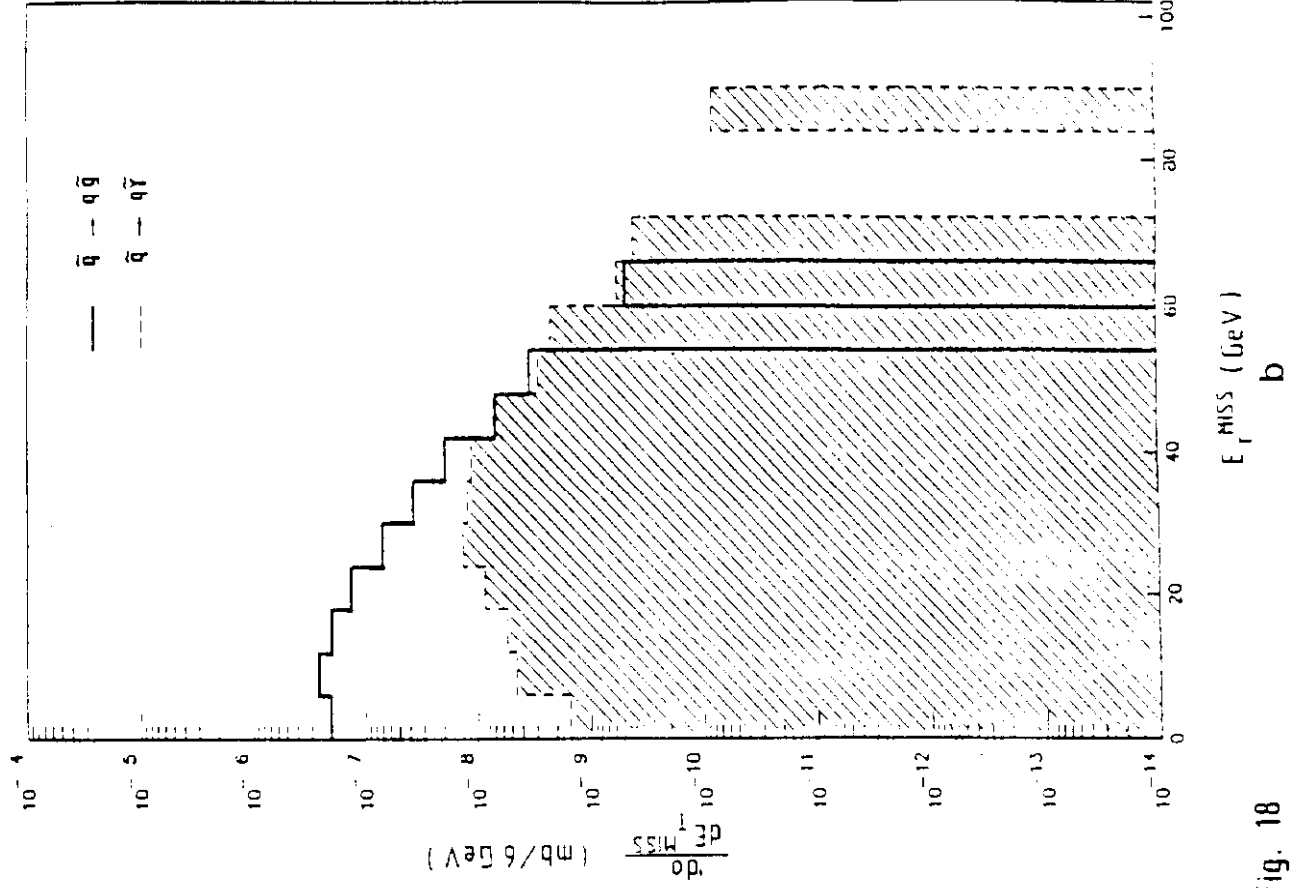
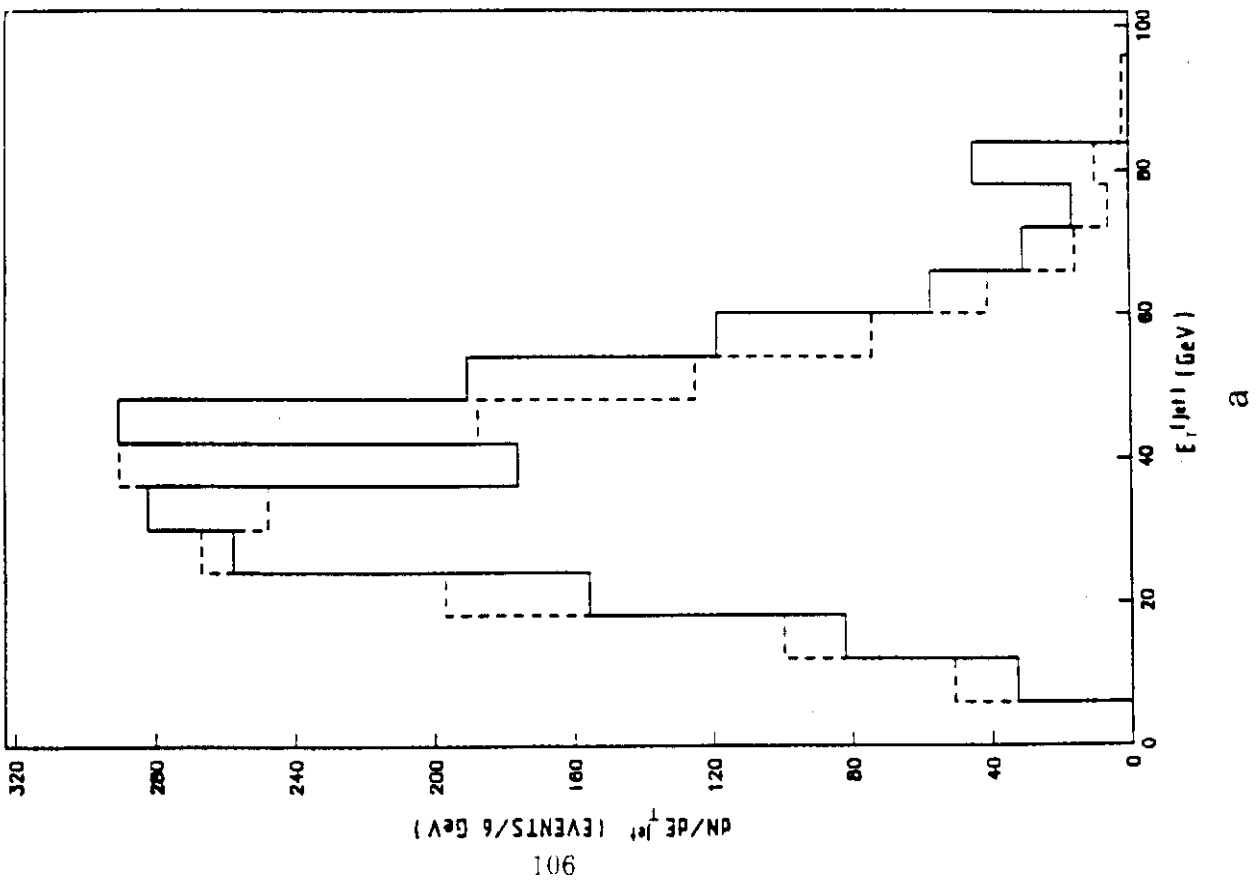


Fig. 18



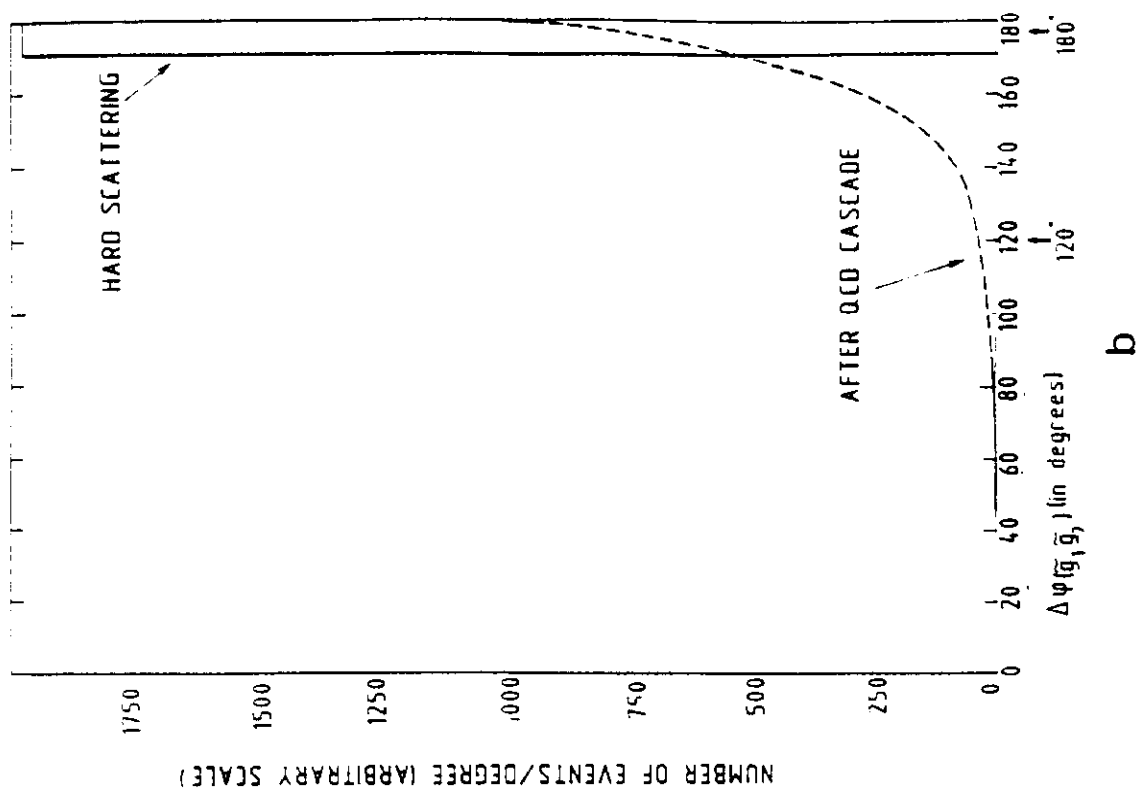
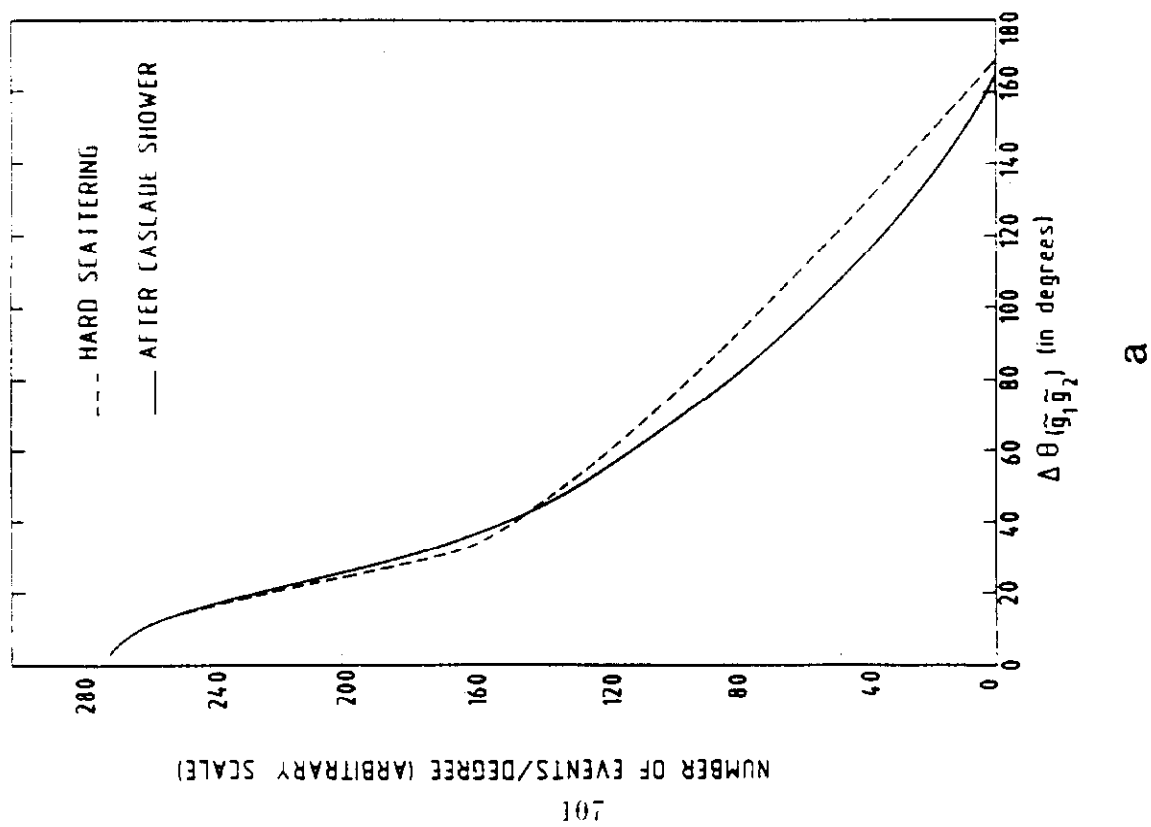


Fig. 19

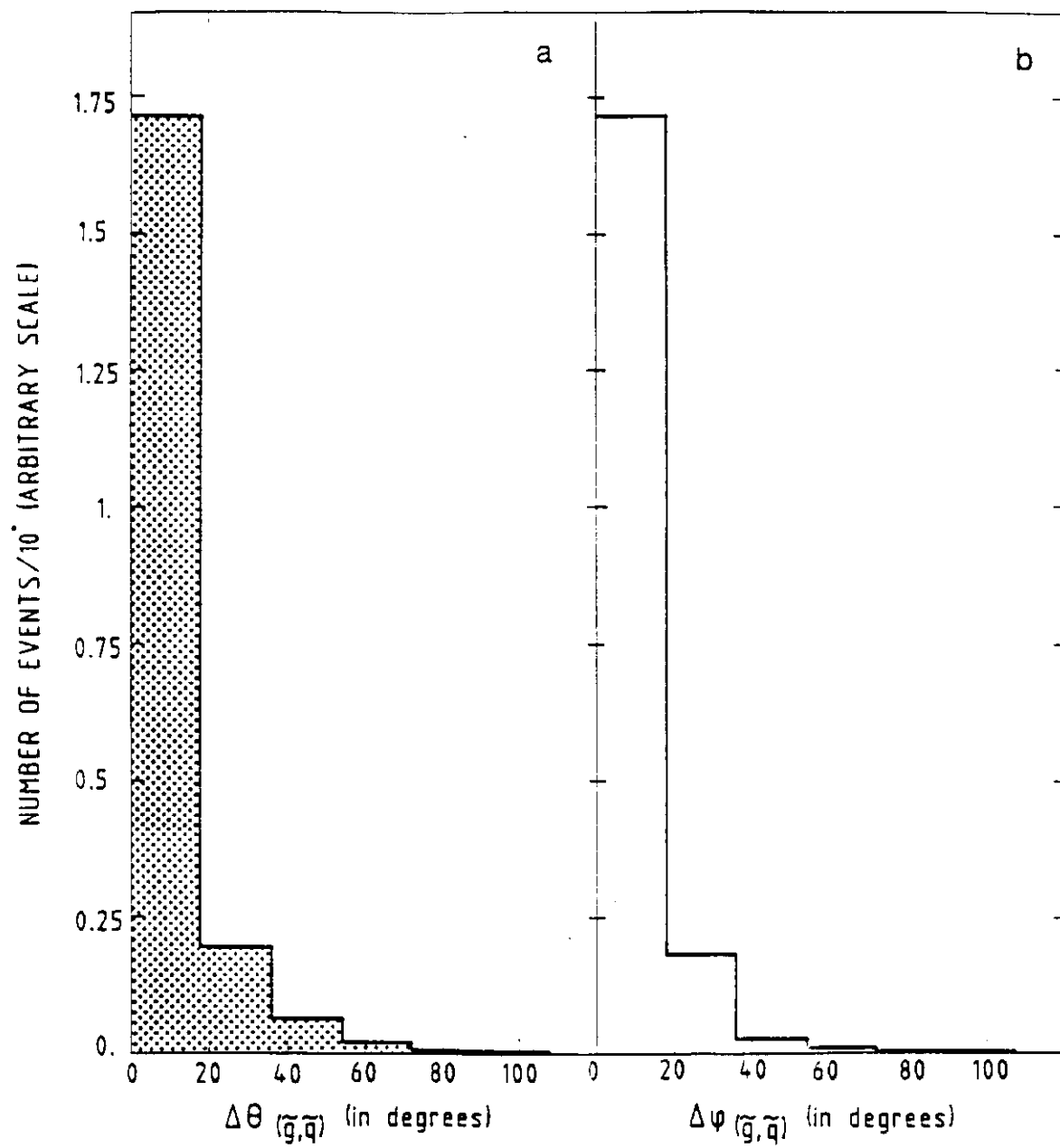
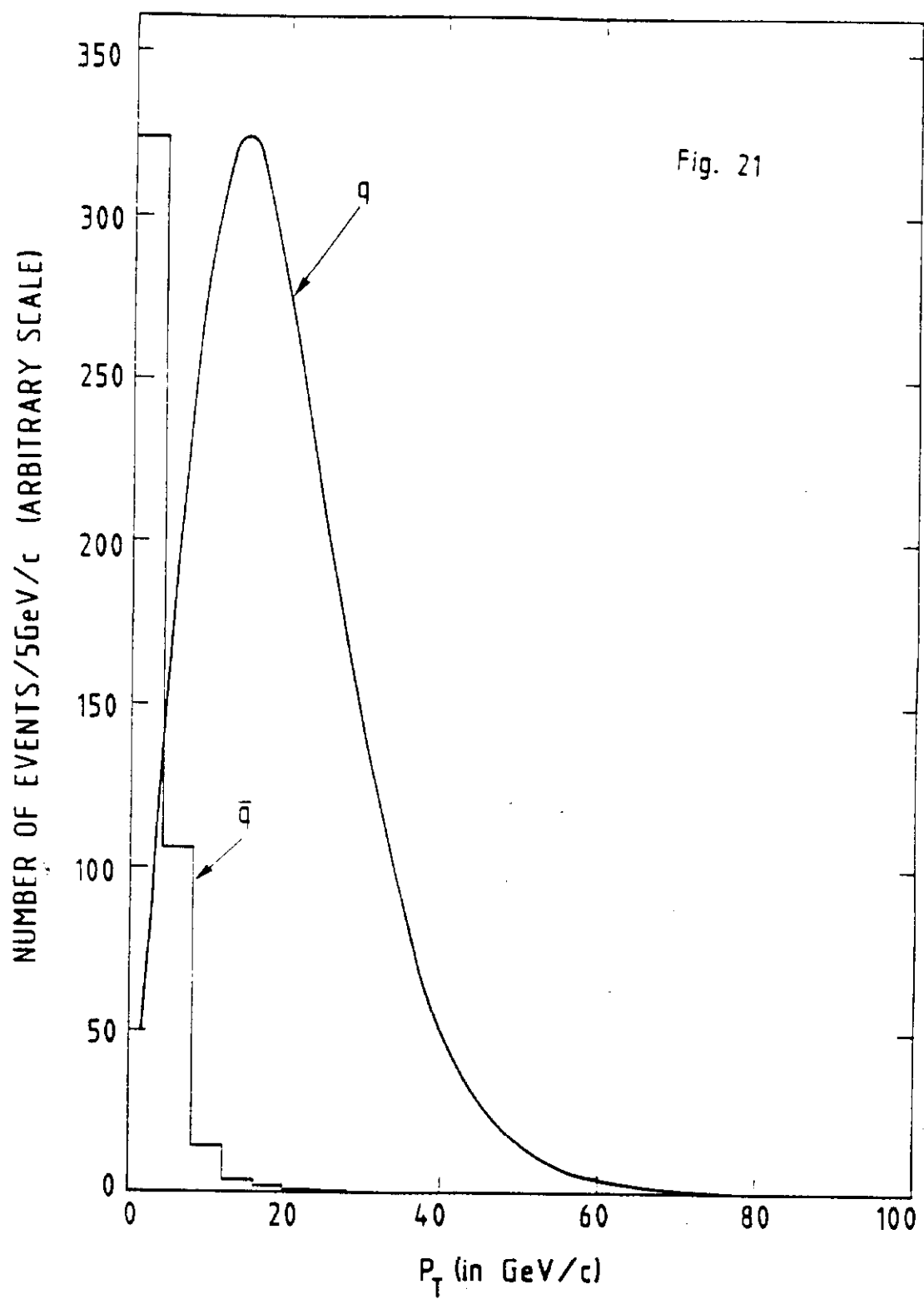


Fig. 20



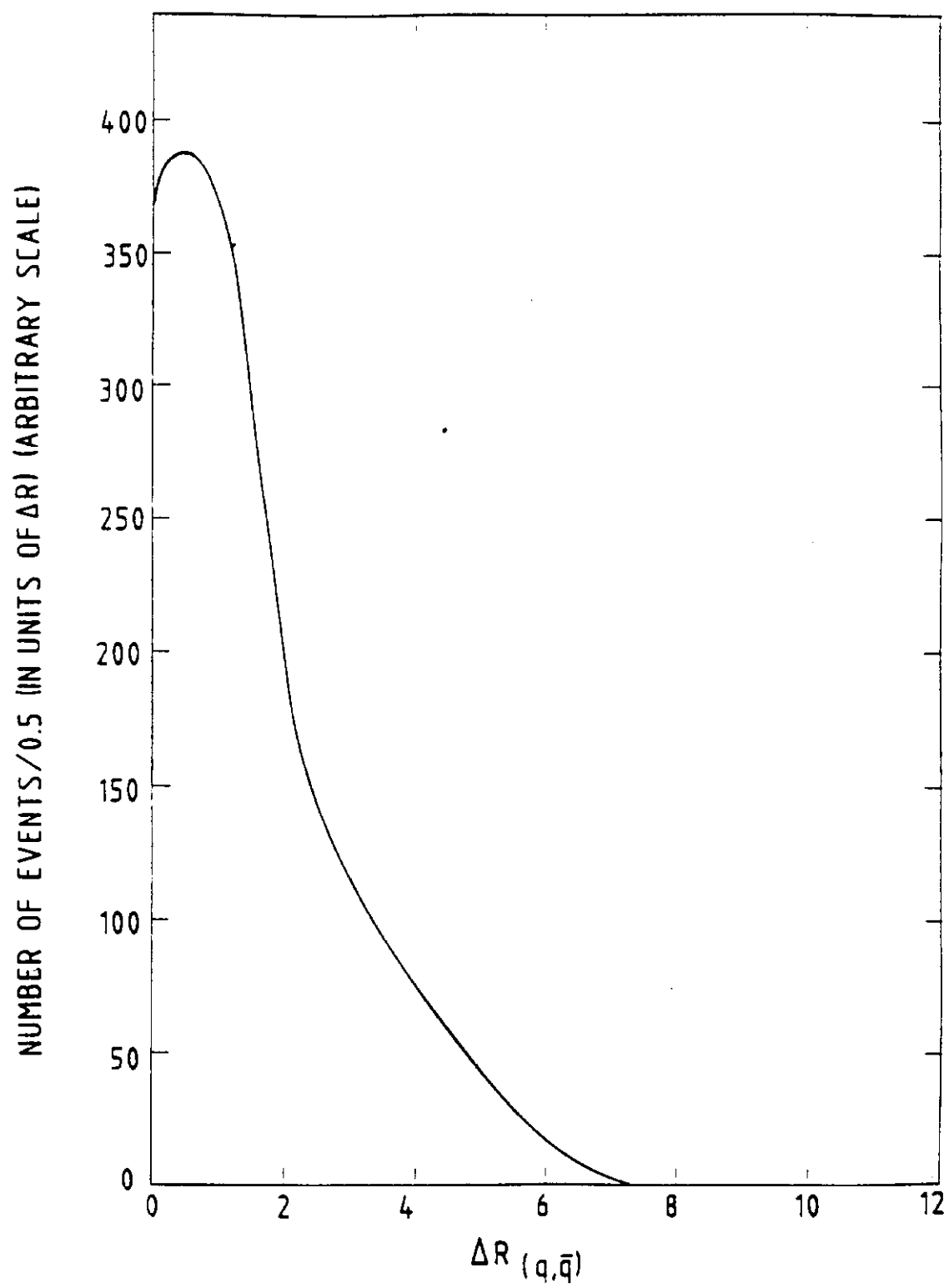
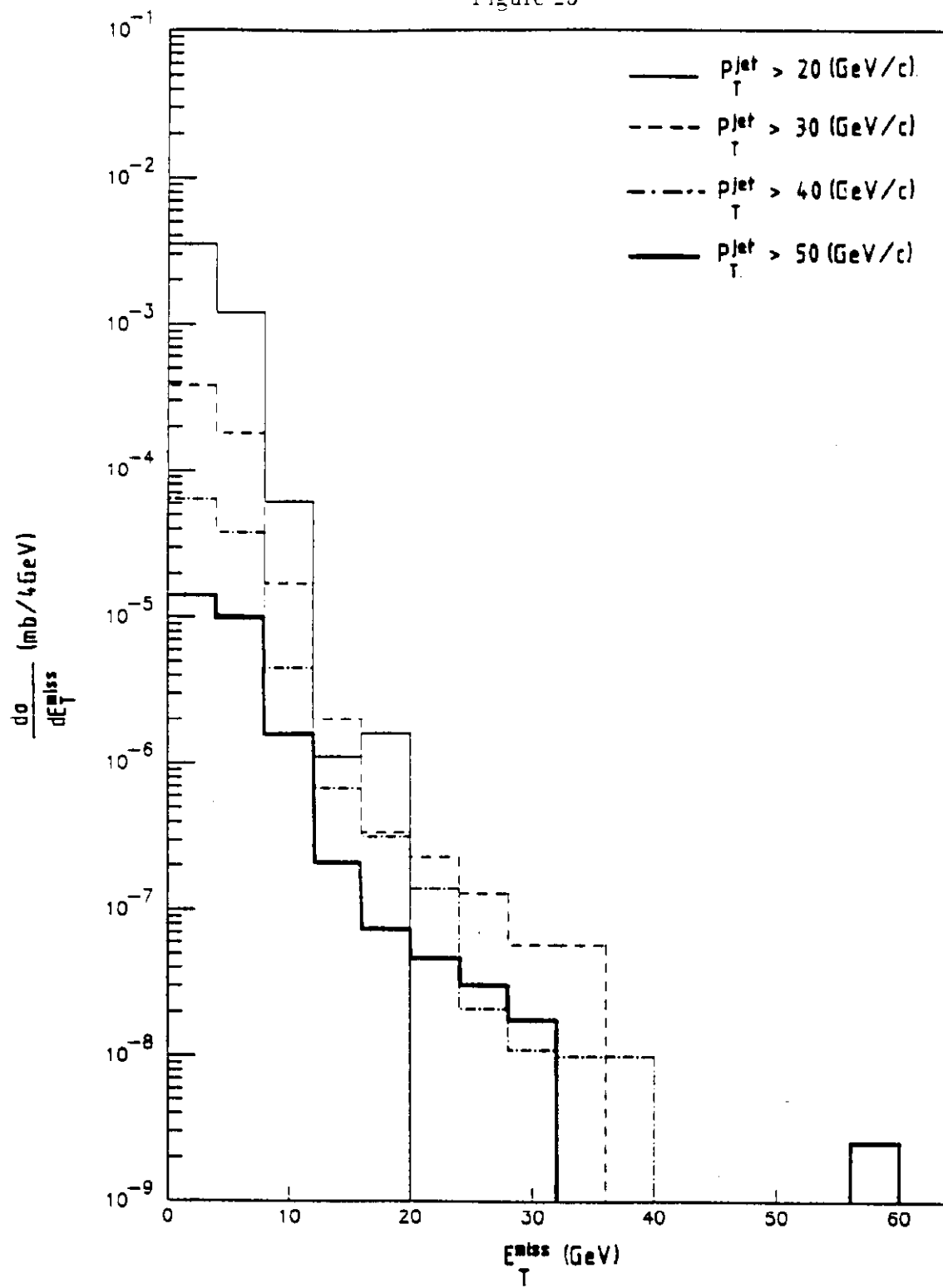
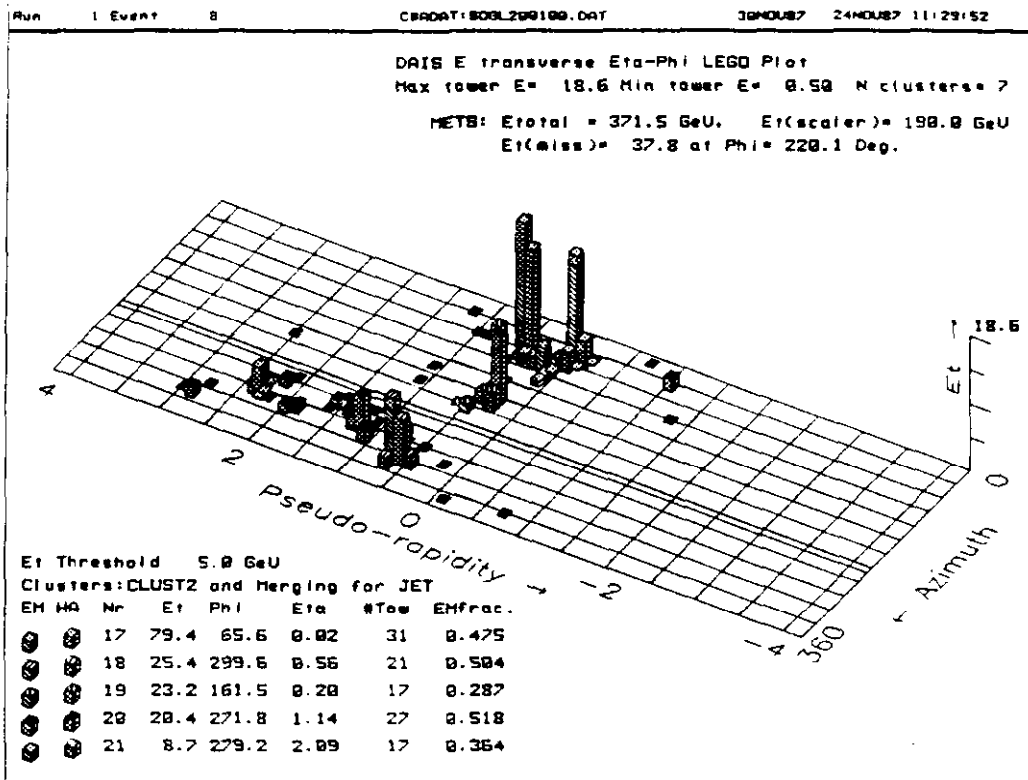


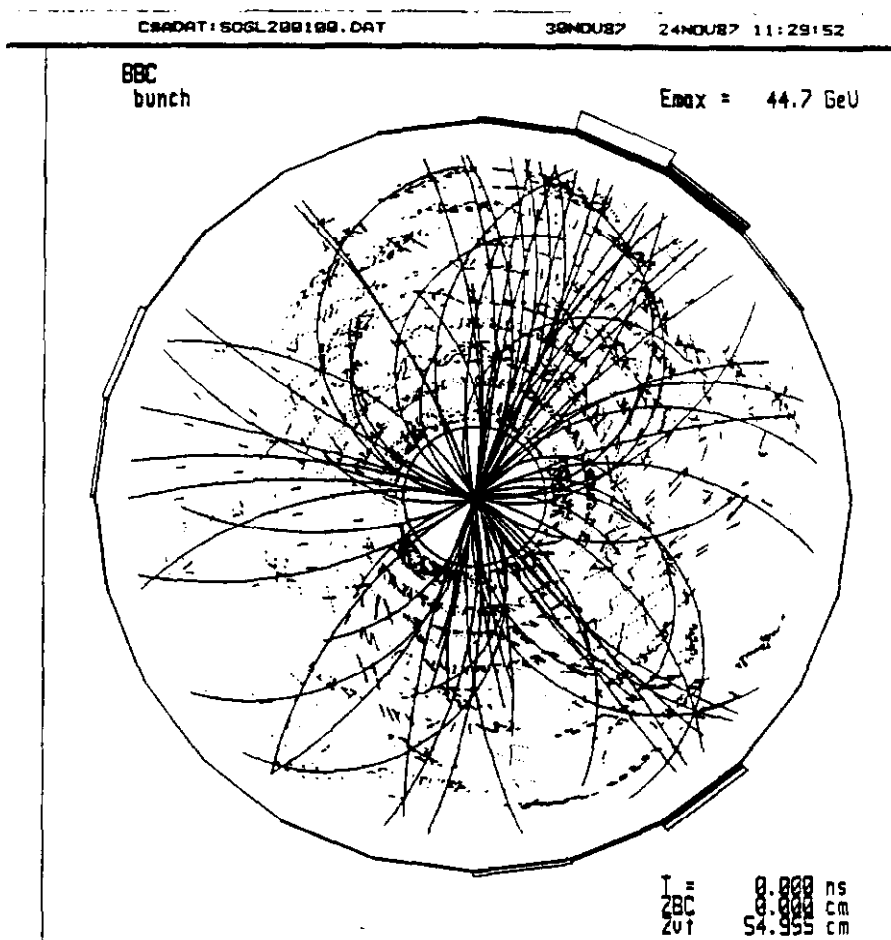
Fig. 22

Figure 23



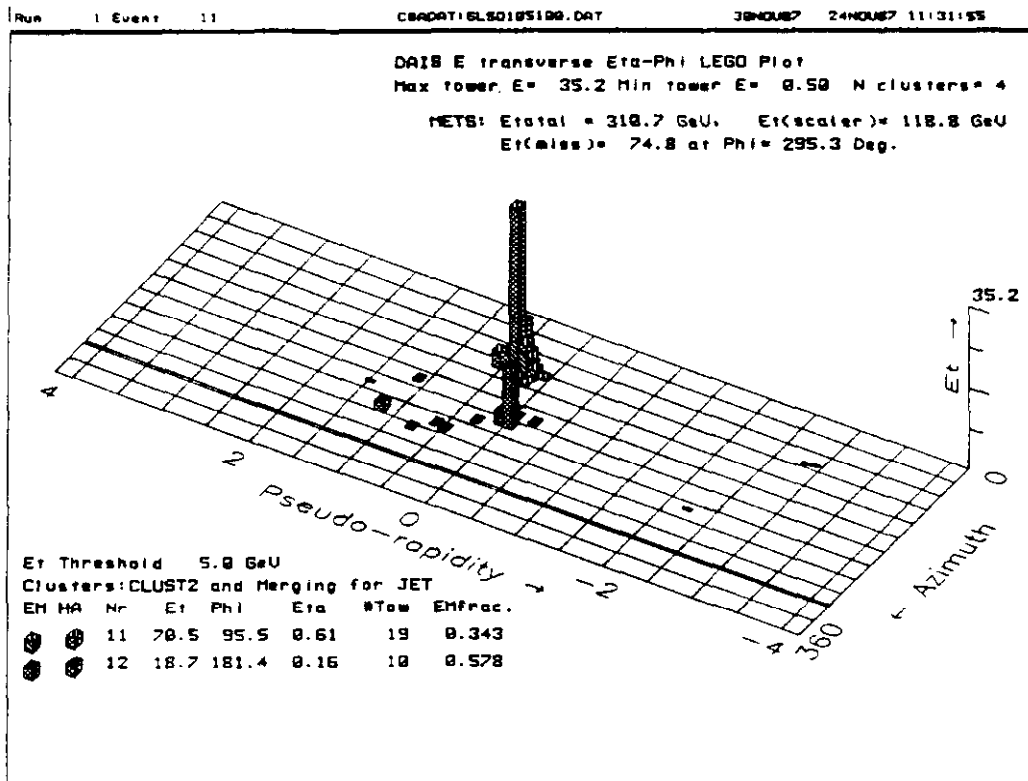


a



b

Fig. 24



a

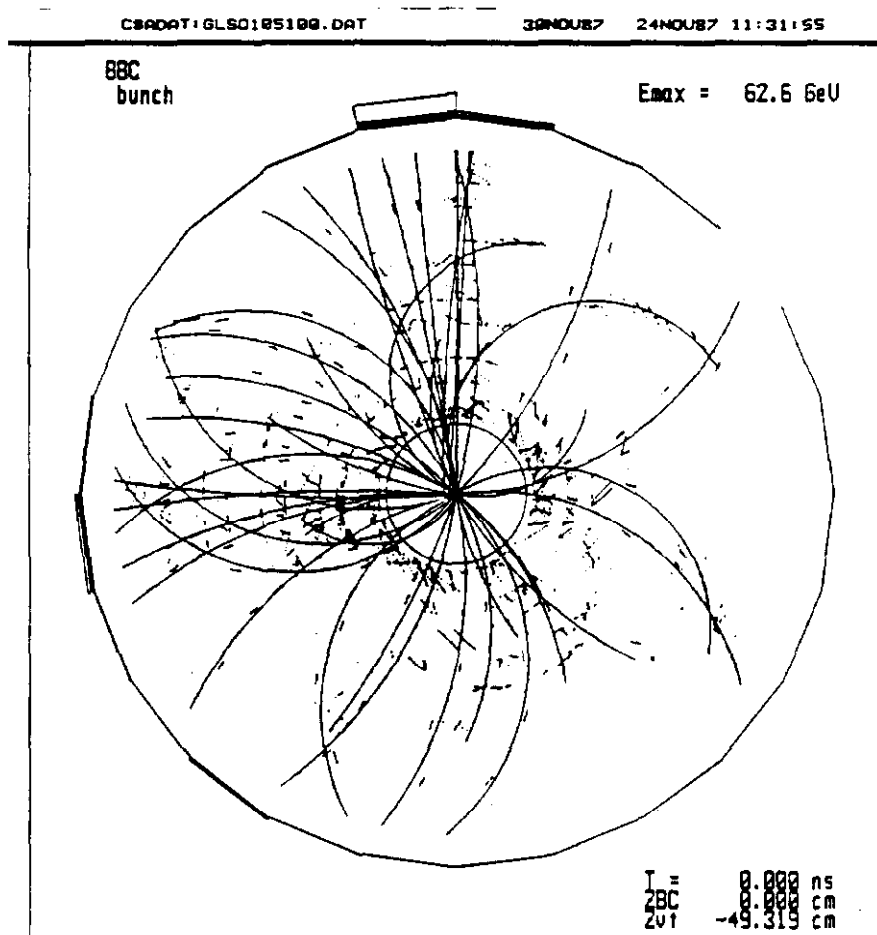


Fig. 25

b

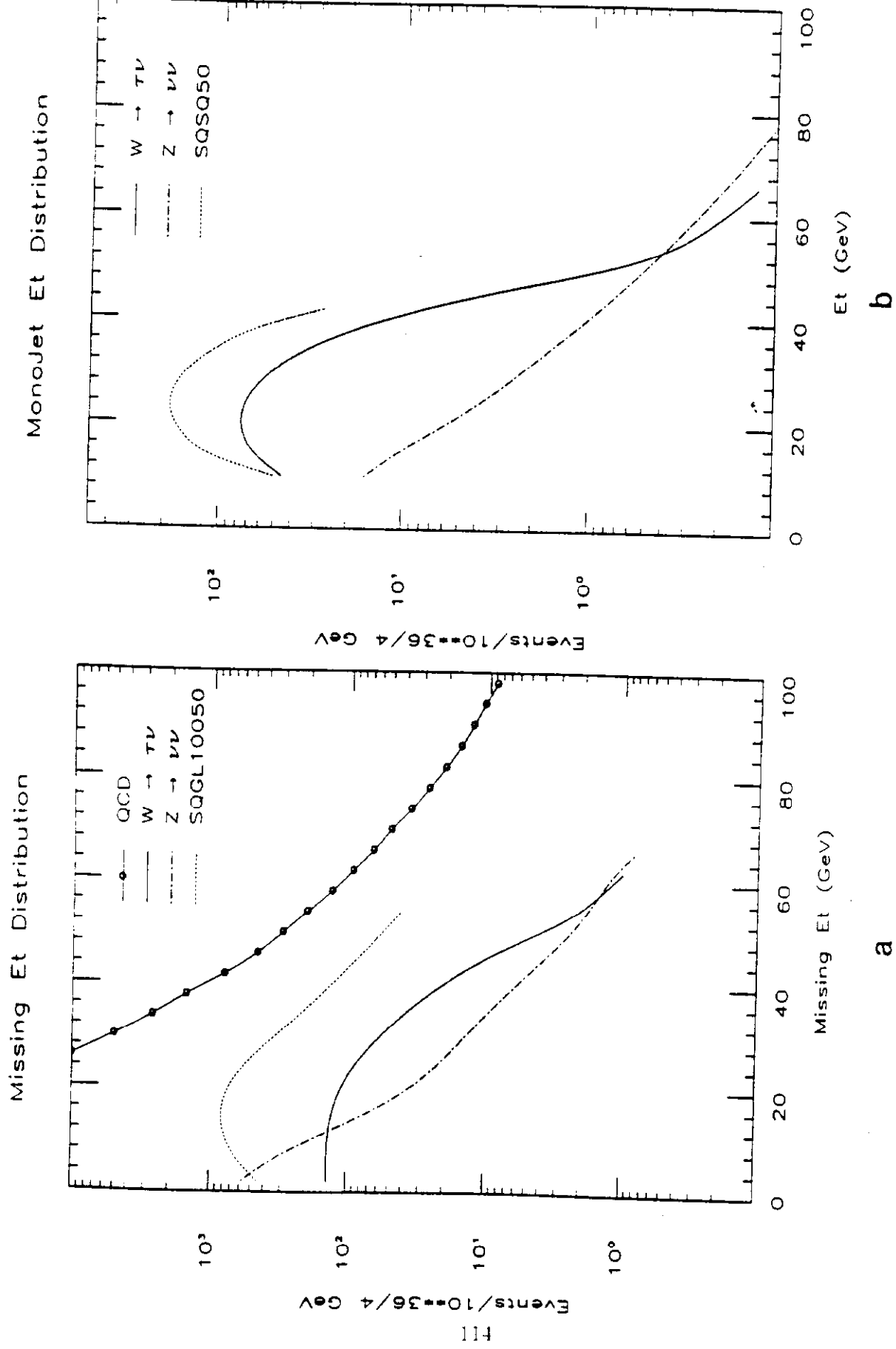


Fig. 26

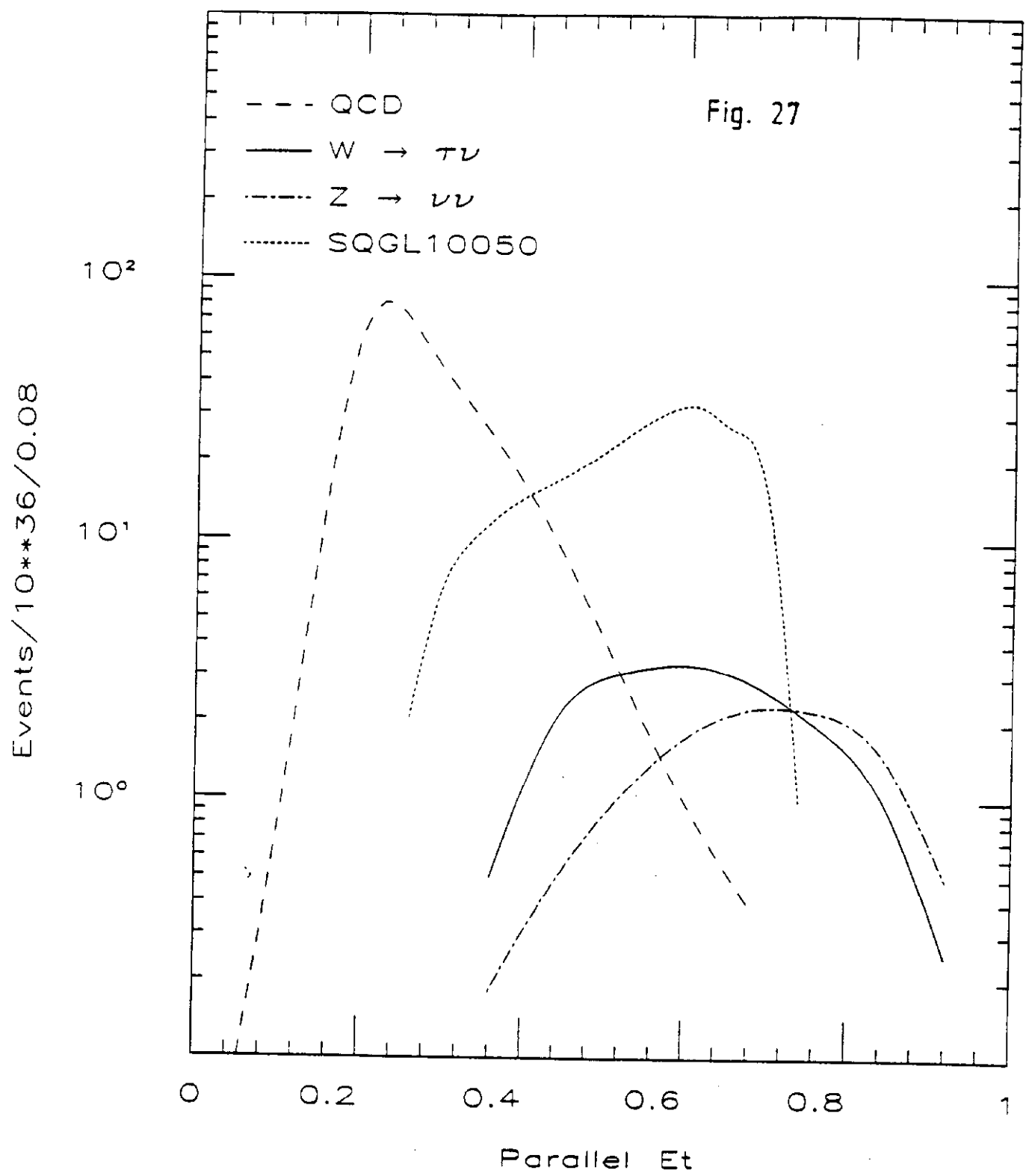


Figure 28

